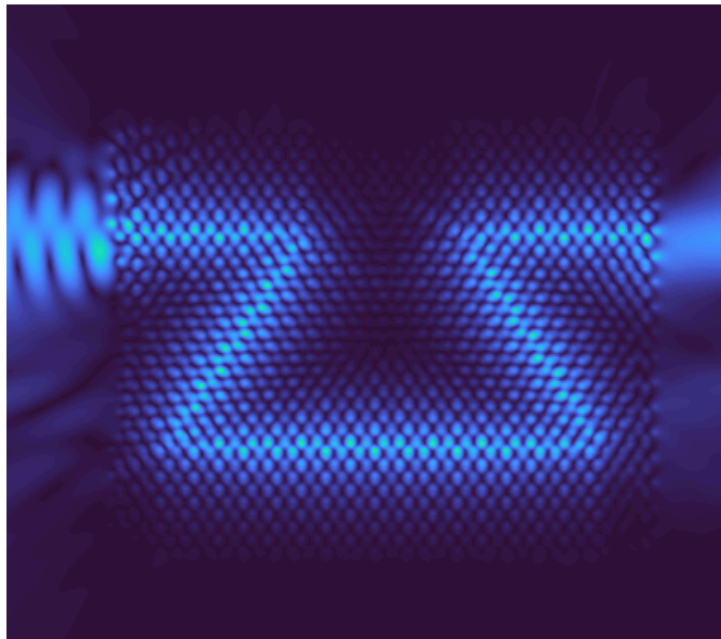


Valley-contrasting Physics in All-dielectric Photonic Crystals



Reiko Inoue Bendtsen
FYSIK 10
Department of Materials and Production
Aalborg University



AALBORG UNIVERSITY
STUDENT REPORT



AALBORG UNIVERSITY
STUDENT REPORT

Department of Materials and Production
Aalborg University
<http://www.aau.dk>

Title:

Valley-contrasting Physics in
All-dielectric Photonic Crystals

Theme:

Methods and Applications of
Physics

Project Period:

Spring Semester 2022

Project Group:

FYS10 2022

Author:

Reiko Inoue Bendtsen

Supervisors:

Thomas M. Søndergaard

Copies: 1

Page Numbers: 105 (84 in the
main text)

Date of Completion:

May 18, 2022

Abstract:

Inspired by recent applications of topology in photonics, which led to discovery of unconventional ways of manipulating light, this report first presents a comprehensive review of 2D photonic topological insulators (PTIs), with an emphasis on valley-PTIs. It then demonstrates the basic ideas and features, including valley Chern numbers and formation of kink states, through numerical calculations utilizing plane wave expansion method, Fast Fourier Transform, Green's Function Area Integral Method etc. Our main contribution is comparison of robustness of light propagation among various types of interfaces formed between two finite-sized topologically distinct photonic crystals (PhCs). We find that the kink states along a bearded-stack domain wall are the most robust among the configurations examined. We also observe the back-scattering free propagation in the valley-PTIs, even in the presence of sharp bends, which cannot occur in conventional PhC waveguides. We also investigate how a chiral light source propagates in a valley-PTI. We confirm that a bearded-stack domain wall allows unidirectional coupling between the valley chiral state and the chirality of the light source, and the behavior is dictated by the value of the dot product (coupling) between the field and chiral dipole moment.

Contents

1	Introduction	1
1.1	Topological Photonics	1
1.2	Valley-Photonic Topological Insulators and State of the Art	2
1.3	Main Focus of this Report	4
1.4	Overview of the Report	6
2	Photonic Topological Insulators	7
2.1	Brief Review of the Origin of Topological Insulators	7
2.1.1	Integer Quantum Hall Effect	8
2.1.2	Berry Phase, Berry Connection, and Berry Curvature	10
2.1.3	Chern Number and Topological Phases in 2D Photonic Crystals	12
2.1.4	Photonic Realizations of Fundamental Topological Models	13
2.2	Valley-Photonic Topological Insulators	16
2.2.1	Valleys in Photonics	16
2.2.2	An Example Study of Valley-Photonic Topological Insulators	18
2.2.3	Recent Development of Valley-Photonic Topological Insulators	21
2.3	Designing Valley-Photonic Topological Insulators: A Summary	23
3	Computational Methods	25
3.1	Modeling Band Structures of Honeycomb Photonic Crystals Using Plane-wave-expansion Method	25
3.1.1	Structure Factor and Fourier Coefficients for Honeycomb Lattice	26
3.2	Iterative Method Taking Advantage of the Fast Fourier Transform and PWE Theory	27
3.2.1	Iterative Method in a Nutshell	28
3.2.2	Main Steps	28
3.3	Fast Iterative FFT-based Approach for Solving the GFAIEM	30
3.3.1	GFAIEM for 2D Photonic Crystals	31
3.3.2	Green's Function Area Integral Equation	31
3.3.3	Fast Iterative FFT-based Approach	32
3.3.4	Chiral Magnetic Dipole	33
3.3.5	Calculation of Magnetic Field Based on Electric Field	34

3.3.6	Summary	35
4	Valley Photonic Topological Insulators	37
4.1	Breaking Inversion Symmetry of Honeycomb Lattice Photonic Crystals	37
4.2	Numerical Calculation of the Valley Chern Numbers	39
4.2.1	Valley Chern Numbers	39
4.2.2	Calculation of Berry Curvatures	41
4.2.3	Calculation of Electric Field Distribution	42
4.2.4	Reciprocal Space Grid	43
4.2.5	Calculated Topological Indices	43
4.3	Valley Photonic Topological Insulators Studied in This Project	45
4.3.1	Valley Photonic Crystals	45
4.3.2	Valley-dependent Kink States	46
4.3.3	Valley-Photonic Topological Insulators and Coupling	48
4.4	Summary	50
5	Waveguide Quality of Valley-PTIs	53
5.1	Formation of Z-shape Bend	53
5.1.1	Kink States Localized at a Domain Wall	53
5.1.2	Various Types of Boundaries	54
5.2	Comparison between Kink States and Waveguides	59
5.2.1	Propagation of Light in a Z-shape Bend Waveguide of a Photonic Crystal	59
5.2.2	Propagation of Light in Zigzag-edge Domain Walls	63
5.2.3	Propagation of Light in Bearded-stack Domain Walls	67
5.3	Unidirectional Coupling – Chiral Light-Matter Interaction	72
5.3.1	Method for Testing the Hypotheses	72
5.3.2	Directionality of 2D Honeycomb Lattice Silicon Rods: Preliminary Testing	72
5.3.3	Explaining Directionality by Coupling Between Chiral Magnetic Dipole and Magnetic Field	73
5.3.4	Zigzag-edge Domain Walls	79
5.4	Conclusion	82
6	Conclusion	83
A	Fast Fourier Transform	91
A.1	Fourier Transform	91
A.2	Discrete Fourier Transform and Fast Fourier transform	92
A.3	Convolution Theorem	93

Preface

This report is written by Reiko Inoue Bendtsen, a 10th-semester student enrolled in the Physics programme at Aalborg University (AAU). It is submitted as documentation for Master's thesis project work during spring 2022 under the supervision of Associate Professor Thomas Møller Søndergaard. The main theme of this report is photonic topological insulators (PTIs), in particular valley-PTIs. This project was carried out in the spirit of AAU's problem-based learning (PBL), where physics students receive research-based education and learn to work as researchers. The intended readers are thus societies of professionals and researchers, including students, in physics-related fields. This report is written assuming that the reader possesses basic knowledge of optics, solid state physics, and quantum mechanics in order to obtain a good grasp of the contents.

Reading guide

Throughout the report, citations are given in the form of three alphabetic characters and a two-digit number, for example [EIN17], where the first three letters represent the author(s) or the publisher and the two-digit number represents the year of publication. All the references are listed in the bibliography at the end of the report. Equations, figures, and tables are referenced by two numbers separated by a period, where the first number represents the chapter in which they appear and the second number represents their chronological order within the chapter. Vectors and matrices are written in bold face, while scalars are written in normal font.

Reiko Inoue Bendtsen
rbendt15@student.aau.dk

Nomenclature

The following lists describe the main symbols and abbreviations that will be later used within the main text.

List of Symbols

\mathbf{a}_i	Primitive vector of crystal lattice
\mathbf{b}_i	Primitive vector of reciprocal lattice
\mathbf{B}	Magnetic induction field vector
c	Speed of light
\mathbf{D}	Electric displacement field vector
\mathbf{E}, E	Electric field vector, amplitude
$E(\mathbf{H})$	Electromagnetic functional
\mathbf{H}, H	Magnetic field vector, amplitude
\mathbf{M}	Magnetization
k	Wave number
\mathbf{k}	Wave vector
k_0	Free-space wavenumber
$\hat{\mathbf{n}}$	Normal vector
μ_0	Magnetic permeability of vacuum
$\epsilon(\mathbf{r})$	Dielectric function/constant (relative dielectric permittivity)
ϵ_0	Dielectric permittivity of vacuum
λ	Wavelength
Λ	Lattice constant, length of primitive lattice vector of crystal lattice
a	Distance between rods in honeycomb lattice
w_0	Waist radius of a Gaussian beam
λ_0	Free-space wavelength
ω	Frequency
ρ	Charge density
\mathbf{J}	Current density
g	Green's function
δ	Dirac delta
\mathbf{r}	Spatial location
N	Number (e.g., number of divisions)
C_n	Chern number
\mathbf{d}_\pm	Magnetic dipole moment
\mathcal{H}	Hamiltonian operator
$\lambda_n(\mathbf{k})$	Eigenenergy
$\psi_n(\mathbf{k})$	Normalized eigen wavefunction
$\mathbf{A}(\mathbf{k})$	Berry connection
$\Omega(\mathbf{k})$	Berry curvature
ϕ	Berry phase

List of Abbreviations

Valley-PTIs	valley Photonic Topological Insulators
PhC	Photonic Crystal
VPhC	Valley Photonic Crystal
DoF	Degree of Freedom
QHE	Quantum Hall Effect
QSHE	Quantum Spin Hall effect
QVHE	Quantum Valley Hall effect
THz	Terahertz
EM	Electromagnetic
TI	Topological Insulator
TPEM	Topologically Protected Edge Mode
HC	HoneyComb
CES	Chiral Edge State
L(R)CD	Left(Right)-handed Circularly Polarized
MOS	Metal Oxide Semiconductor
Si	Silicon
SOI	Silicon-On-Insulator
GFAIEM	Green's Function Area Integral Equation Method
PPWG	Parallel Plate WaveGuide
OAM	Orbital Angular Momentum
PBG	Photonic Band Gap
PWE	Plane Wave Expansion
1 BZ	First Brillouin Zone
TE	Transverse Electric
TM	Transverse Magnetic
UDC	UniDirectional Coupling

CHAPTER 1

Introduction

For several decades now, ideas and concepts from solid-state physics aimed at steering the passage of electrons in an electron current have been emulated in photonics in order to better control and manipulate electromagnetic waves. An area of this emerging field of topological photonics, where engineers/researchers take advantage of valleys as a powerful degree of freedom (DoF) for the manipulation of electromagnetic waves, is called topological valley photonics. The photonic systems - so-called valley photonic topological insulators (valley-PTIs) - emulate the quantum valley Hall effect studied in graphene-like materials in solid-state physics, and are easy to construct from dielectric materials, but provide waveguiding that is more robust against small defects and backscattering than ever before.

1.1 Topological Photonics

Topological photonics is one of the most active research areas in photonics recently and has been growing rapidly since its inception as an optical analog of the Quantum Hall Effect (QHE) [KDP80] proposed in 2008. This field aims to explore the physics of topological phases of matter, originally discovered in solid-state electron systems, in a novel optical context in order to design and control the behavior of light, by exploiting geometrical and topological ideas. [OPA⁺19], [WGXL20]

Since the pioneering works of Yablonovitch and John in 1987 [Yab87], [Joh87], it has been recognized that periodic photonic structures (i.e., “photonic crystals”) have remarkable capabilities in terms of manipulating the flow of light. In the past three decades, many physics and device applications of photonic crystals (hereinafter referred to as PhCs) utilizing the limited photonic DoFs, such as frequency, polarization, and phase, have been proposed. In topological photonics, additional DoFs possessed by electrons, such as spin and valley, are also simulated, by constructing so-called

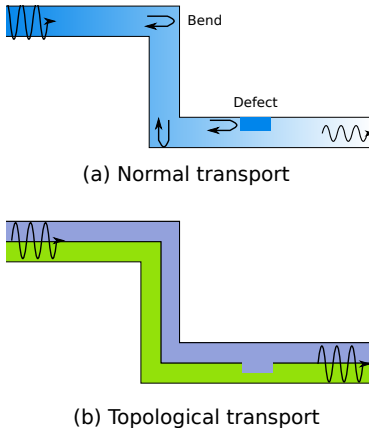


Figure 1.1: Normal (a) vs topologically protected (b) transport. The normal case has backscatter at sharp corners and defects, leading to low transmission. Topological transport, where the wave propagates at the interface, is backscattering free. [BDZ⁺20]

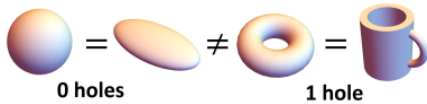


Figure 1.2: Topology concerns quantities that are preserved under continuous deformations of objects. The number of holes in a closed surface (genus) is an example of a topological invariant, since a hole cannot be added or removed without tearing or stitching the surfaces, which is not considered a continuous deformation: a torus can be stretched and pulled into a coffee cup shape, but not a sphere. [BDZ⁺20]

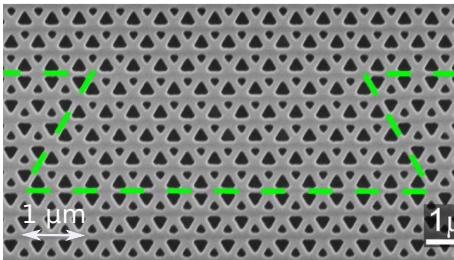


Figure 1.3: Scanning electron microscopy image of a sample composed of two parts with opposite ‘polarities’ separated by a trapezoidal interface [KS17]

photonic pseudospin and/or valley pseudospin. [XYZ21]

Often called semiconductors of light, PhCs are the optical analog to crystals with nearly free electrons. They were born by applying ideas of solid-state physics to photons. In the same way, the new field of photonic topological insulators (PTIs) finds its origins in the world of electronic systems; topological photonics attempts to emulate the concepts of electronic topological insulators (TIs) in electromagnetic (EM) systems [SB20].

TIs are perfect conductors on the edges. The current continues to flow without being scattered into the bulk or being backscattered by local defects, by disorder in the lattice, or by sharp edges. Due to the lack of backscattering, such topological edge currents are often viewed as unidirectional. This property is often called “topologically protected transport” or “topologically protected edge modes (TPEMs).” Fig. 1.1 illustrates this. At the same time, they are “insulators” that behave like regular electrical insulators within the bulk of the material. They are called “topological,” because they can be categorized by a so-called “topological invariant” that does not depend on the fine details of the system, such as minor defects and obstacles on the surface [BDZ⁺20], [SB20]. See Fig. 1.2 for a brief illustration of topology.

1.2 Valley-Photonic Topological Insulators and State of the Art

Recently, the valley binary DoF has been introduced and photonic Quantum Valley Hall Effect has been realized in 2D PhCs, metamaterials¹, and other periodic photonic structures due to the recent explosion in so-called valleytronics². Such systems exhibit topological photonic states with unusual features, and a few promising applications have been identified, ranging from on-chip communication to quantum cascade lasers. Fig. 1.3 shows an example of an actual PTI waveguide, with the path of a photon highlighted in green. The experiment showed that each turn in the path resulted in backscattering losses of only a few percent.

Although the valley DoF is still relatively less known in the photonic community, various designs that realize topologically protected robust propagation and refraction have already been proposed, and physics combining valley DoF and spin DoF (called spin-valley physics) has been studied, leading to identification of many other interesting phenomena, and potential applications. Valley-PTIs have been implemented at different frequencies, ranging from microwave over terahertz, to optical frequencies, and platforms, such as substrate-integrated platforms, dielectric scatterers, scatterers between two metallic plates etc. Photonic valley-Hall systems are also used to construct topological cavities and lasers, and the features of valley-PTIs, including linear dispersion, single-mode propagation, topological protection, high-density integration, and low-propagation losses, are actively exploited for robust on-chip communication. [XYZ21]

¹Any artificial materials engineered to have exotic properties [Gap10]

²An experimental area in semiconductors that exploits valley DoF in the electronic band structure to store and carry information (similar to spin in spintronics [XYZ21])

The reason why topological photonics has attracted so much attention is its potential to produce TP EMs that are robust against disorder and imperfection, achieving ballistic transport (traveling at high speeds within a medium without scattering off of obstacles). Hereinafter, we define *robustness of transport* to mean how a waveguide is immune to backscattering of any forms. A relevant question is then how robust is their topological transport compared to standard photonic non-topological transport. This question is especially relevant in topological valley photonics, because the robustness of topologically protected transport of valley-PTIs is said to be strictly less robust compared with that achieved by so-called Chern PTIs.

Chern PTIs guarantee non-reciprocal³ unidirectional (i.e., backscattering-free) transport along the interface between topologically trivial and non-trivial systems by breaking so-called time-reversal symmetry. Valley-PTIs, on the other hand, preserve time-reversal symmetry, meaning that reciprocity necessarily holds. Thus, every edge mode always comes with its time-reversal image. Moreover, such edge modes must be protected by crystal symmetries and valley conservation. This means that edge modes must be formed at an interface between a pair of topologically distinct but symmetric PhCs. [XYZ21], [OF19]. See Fig. 1.4 for examples of interfaces formed between two PhCs using symmetry operations.

Nonetheless, [ABB⁺21] experimentally found that TP EMs of valley PTIs (honeycomb (HC) lattice structure with triangular holes) are two orders of magnitude more robust than modes of conventional PhC waveguides, at least at the telecommunication wavelengths. In an interesting study comparing valley-PTIs and spin-PTIs, [OF19] quantitatively studied the robustness of subwavelength edge modes originating from metamaterial spin-Hall effect and metamaterial valley-Hall insulators based on valley preservation for all possible interface types, and demonstrated superior robustness of the valley-Hall edge states, provided one works with a zigzag-edge interface.

There are many studies on metal valley-PTIs that show how bends in waveguide paths will not lead to intervalley scattering. For example, [GYG⁺17] showed that a so-called bearded-stack interface formed between HC-lattice metal PhCs having opposite orientation is robust against 120° path bends, through simulation and experiment. [WH15] numerically investigated the propagation of TP EMs along paths with different bending angles using triangular-lattice metal-dielectric PhCs and similarly found negligible backscattering. For all-dielectric valley-PTIs, [CZCD17] showed that HC silicon-rod PTIs in air with zigzag-edge interface achieves very high transmission even with an interface having Z-shaped bends, proving backscattering-free transportation of the PTIs. However, there are not many studies on all-dielectric PTIs that compare various types of interface against waveguides of ordinary PhCs.

Another important feature of valley-PTIs is so-called unidirectional coupling (UDC)⁴. [RHZD21] studied HC dielectric PhC slabs whose unit cell contains two cylindrical air holes of different diameters in silicon back-



Figure 1.4: Various types of interfaces

³Reciprocity is a fundamental concept in light transport that can be stated as “if I can see you, you can see me.” In essence, this means that if a light ray can travel from point A to point B, then it can also follow this trajectory in the opposite direction, from B to A [Wie12].

⁴Unidirectional excitation of valley chiral bulk states by external sources with proper

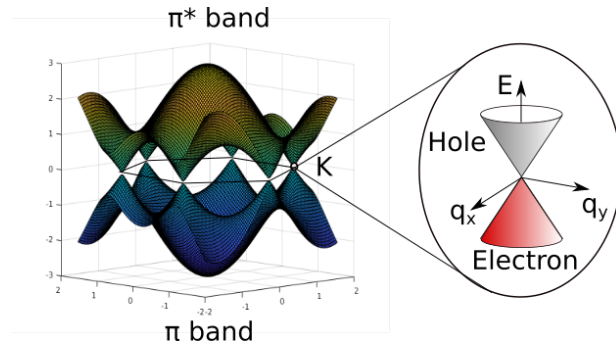


Figure 1.5: Graphene electronic bands. The linear dispersion relation close to the K point of the first 2D BZ is illustrated using the Dirac cone.

ground. It numerically compared directionality and unidirectional coupling of zigzag- and bearded-stack interfaces. [HLY⁺19] experimentally showed robustness and unidirectionality of TP EMs of silicon-on-insulator (SOI) valley PhC slabs having bearded-stack interface as in [RHZD21]. Both studies are important in a sense that they give the physics behind unidirectional excitation of valley chiral states by chiral sources, and necessity of glide-plane symmetry.⁵ However, we were not able to find any studies on unidirectional coupling on two dimensional (2D) silicon rod valley photonic crystals (VPhCs) that exploit valley pseudospin DoF.

1.3 Main Focus of this Report

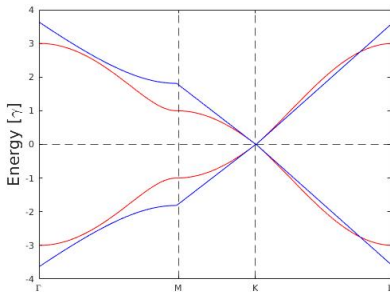


Figure 1.6: The full tight-binding band structure of graphene (red), compared to the so-called Dirac model (blue).

In this P10 project, we aim to study 2D PTIs by applying and expanding previous investigations of dielectric PhCs and their photonic band structures in P9. Furthermore, we have chosen to study valley-PTIs because they can easily be designed purely based on conventional dielectric PhCs and combined with traditional processing techniques to prepare nanophotonic devices; other types of PTIs, such as Chern PTIs and spin PTIs, cannot be constructed from dielectric materials alone [BDZ⁺20].

More precisely, in order to obtain a VPhC, one simply needs to start with a photonic lattice hosting “Dirac-like” degenerate points, which are photonic equivalents of the Dirac points for electrons in graphene. See Fig. 1.5 for an illustration of a Dirac point for electrons in graphene and a so-called Dirac cone showing the linear dispersion relationship in the vicinity of the point. Fig. 1.6 shows a plot of the dispersion relationship; notice the linearity and degeneracy at the K point. One then gaps out the Dirac points through breakage of inversion symmetry [XYZ21]. By preparing two topologically-distinct VPhCs (i.e., VPhCs having opposite orientations) and

chirality[CZCD17].

⁵Interested readers are recommended to read [BS21] and [YHO21], who theoretically and experimentally showed that an ordinary triangular-lattice PhC, which is considered to be an extreme case of HC-lattice PhC where one of the sublattices is eliminated (3-fold rotational symmetry is maintained, but the inversion symmetry is broken), can achieve high transmission and unidirectionality along a bearded-stack interface.

placing them next to each other, the topologically protected transport is realized at the interface [LSH⁺21].

We are particularly interested in two topics. The first is numerical comparison of the robustness of so-called kink states among various types of interfaces as waveguides, in comparison with the robustness of waveguides formed by linear defects in non-topological PhCs. The second is identification of positions in a valley-PTI where the efficiency of UDC is maximized for the case of 2D HC lattice VPhCs having cylindrical silicon rods in air. For this purpose, we use our own programs developed using computational methods we studied in P9, plus software implementing Green's Function Area Integral Equation Method (GFAIEM).

We will first attempt to understand the mechanism of valley-PTIs and confirm important properties of valley-PTIs through numerical calculation, using 2D HC valley-PTI made of two VPhCs whose unit cell contains cylindrical silicon rods with different radii. For the first goal, we systematically compare transmission among various types of interfaces, including armchair-edge, zigzag-edge, and bearded-stack (there are 2 types for each, depending on whether small or big rods meet each other at the domain wall), against transmission of a line-defect waveguide of triangular-lattice PhC. Our hypothesis for the research is:

H1: Kink-states formed between two topologically-distinct VPhCs are more robust than an ordinary PhC waveguide.

In order to compare the robustness, we let a Gaussian beam hit our valley-PTIs/PhCs having two types of domain walls, straight-line and Z-shape bends, and calculate the intensity at the entrance and exit of the waveguides to calculate transmission. Fig. 1.7 illustrates the schematic of the measurement. If there are no differences in transmission between the two types of domain walls, we conclude that the transmission is backscattering-free. Through this comparison, we will find out which type of domain walls will achieve the most stable topologically protected transportation.

Regarding the second goal, previous studies on VPhC slabs with air holes drilled in silicon substrate by [RHZD21] and [HLY⁺19] found that higher UDC efficiency is achieved along bearded-stack domain walls, rather than zigzag-edge domain walls⁶.

They also found that high UDC efficiency is achieved by placing a chiral dipole emitter at the center of one of the bearded air rods, because optical vortex fields around bearded rods in the upper domain will interact with the lower domain, and thus generate chiral-flow edge states as shown in Fig. 1.8. Such chirality ensures the rightward (leftward) excitation by using a right-circularly polarized (RCP)/left-circularly polarized (LCP) source [HLY⁺19], [RHZD21], [YHO21].

We hypothesize, for the case of 2D VPhCs having HC lattice of cylindrical silicon rods in air, that the higher UDC efficiency is achieved in a

⁶It is necessary to break the inversion symmetry of the interface in order to generate optical vortex fields in the edge states for high-efficiency UDC. A valley-PTI having a zigzag-edge domain wall has the inversion symmetry with respect to the y -axis. A bearded-stack domain wall, on the other hand, has glide-plane symmetry, i.e. the inversion symmetry is broken via a translation along the x axis with half lattice constant after a reflection with respect to the y -axis.

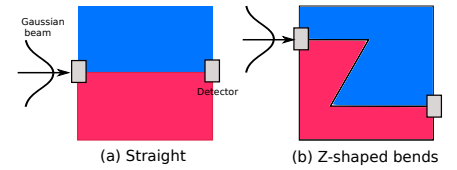


Figure 1.7: Schematic drawing of the measurement

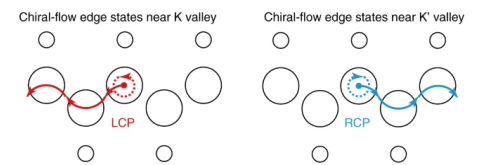


Figure 1.8: Illustration of UDC along the VPhC interface, based on the selective excitation of the phase vortex. The vortex fields around the bearded rods at the upper domain will interact with those of the lower domain, and thus a chiral-flow edge state occurs. [HLY⁺19]

bearded-stack domain wall, than in a zigzag-edge domain wall, as in the case of PhC slabs of air rods in silicon studied by [RHZD21], [HLY⁺19] and [YHO21]. We also hypothesize that UDC phenomena can be explained by coupling between harmonic modes and chiral emitter, i.e., high UDC efficiency is achieved when a chiral magnetic dipole is placed at a location where its inner product with the magnetic field at the location is the highest. We expect that the external magnetic dipole will excite guided modes formed in the PBG, and the directionality is determined by which valley mode, K' or K , is excited. For example, in case of a zigzag-edge domain wall composed of small rods, if a guided mode over the so-called K' valley is excited, the group velocity determined by the slope will be negative. On the other hand, if a guided mode over the so-called K valley is excited, the group velocity determined by the slope will be positive. See Section 2.2 for the discussion.

We form a bearded-stack interface along inverse- Ω and straight-line domain walls, in order to investigate how the efficiency of unidirectional propagation without backscattering depends on the position of a chiral light source. The transmission/intensity needed for calculation of UDC efficiency are found in the same way as for the first goal. Our hypotheses for this topic are:

- H2: Higher unidirectional coupling efficiency is achieved with a bearded-stack interface, than a zigzag-edged interface.
- H3: A chiral light source achieves a high efficiency in unidirectional coupling at a location where its inner product with the magnetic field is high.

1.4 Overview of the Report

The rest of the report is structured as follows. Chapter 2, after a brief review of the origin of PTIs, gives a rough classification of PTIs and discuss features of valley-PTIs through examples. Chapter 3 presents the three main computational methods used in this project in order to model photonic band structures, geometries, distribution of electric fields, and transmission. Chapter 4 provides the theoretical foundation for this project; it presents the valley-PTI to be studied in this project and explains the main concepts such as inversion symmetry breaking and computation of valley Chern number. Chapter 5 presents the results and findings regarding comparison of transmission among kink states of various interface types against a line-defect waveguide of PhC, as well as unidirectional propagation of a chiral light source in a valley-PTI. Chapter 6 summarizes the results, main contribution of the project to the accumulated knowledge in this field, and future outlook.

CHAPTER 2

Photonic Topological Insulators

Topological photonics is a rapidly growing field in photonics due to its novel possibilities of manipulating light, and a myriad of articles on both theoretical and experimental investigations as well as review articles are available for various topics. In this chapter, we aim to provide a rough overview of this field, attempt to cover the basic concepts of topological phases and main achievements in the field, as well as classify the general directions of photonic realization of topological insulators. For ease of presentation, we limit our attention to 2D systems.

2.1 Brief Review of the Origin of Topological Insulators

TIs found their beginning in the 1980s with the discovery of the QHE [KDP80]. In this effect, a two-dimensional electron gas subjected to a strong perpendicular and uniform magnetic field at very low temperature exhibits robust plateaus in the Hall conductance as a function of the magnetic field at values equal to integer multiples of the fundamental constant e^2/h . See Fig. 2.1 for an example of such measurement. The QHE shows that conductivity is fundamentally *discrete*, and the gas was found to exhibit TPEMs, effectively making it the first TI ever to be discovered [OPA⁺19], [BDZ⁺20].

Researchers then asked the question, whether the concept of TIs is unique to fermionic systems or if it might be found in bosonic systems as well. In 2005, Haldane and Raghu [HR08] made the crucial observation that topological band structures are, in fact, a ubiquitous property of waves inside a periodic medium, regardless of the classical or quantum nature of the waves, and theoretically proposed how to construct analogues of Quantum Hall edge states in “photonic crystals” made with nonreciprocal (Faraday-

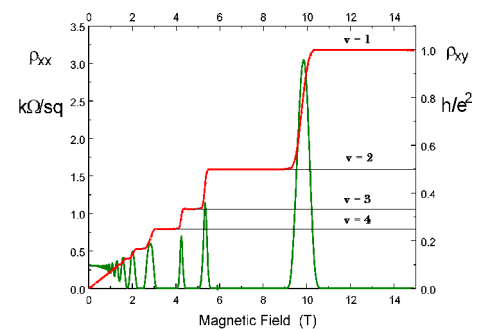


Figure 2.1: Typical measurement of the integer quantum Hall effect. The Hall resistivity exhibits plateaus quantized in exact multiples of h/e^2 . [CDG⁺11]

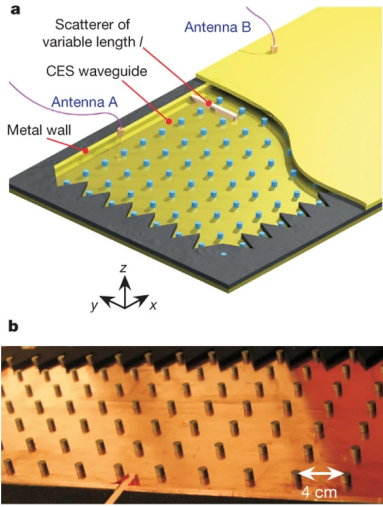


Figure 2.2: a: Schematic of the waveguide composed of an interface between a gyromagnetic photonic-crystal slab (blue rods) and a metal wall (yellow). b: Top view (photograph) of the actual waveguide with the top plate removed. [WCJS09].

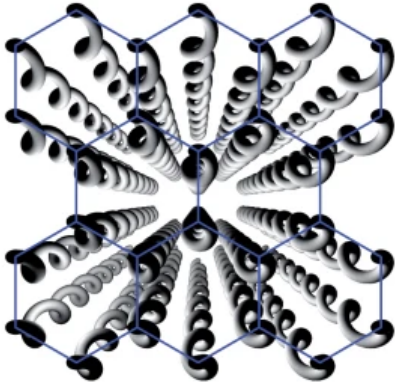


Figure 2.3: Geometry of honeycomb photonic Floquet topological insulator lattice. [RZP+13]

effect¹) media. In other words, it should be possible to construct classical wave systems with analogous properties to their quantum electronic counterparts. By replacing electrons with photons (along with a reinterpretation of some quantities), we may arrive at PTIs, which exhibit many of the same features as TIs. [OPA⁺19], [BDZ⁺20], [SB20].

Three years later, this idea was confirmed by Wang et al., who provided realistic material designs and experimental observations [WCJS09]; a brief explanation of this work is provided in Section 2.1.4. See Fig. 2.2 for the hardware overview. The idea of [WCJS09] was to avoid backscattering by breaking time-reversal symmetry² using gyro-optics materials³ where the application of a magnetic field breaks time-reversal symmetry. These studies spurred numerous subsequent theoretical and experimental investigations, see e.g., [SB20], [LJS14].

The next challenge was to find a way to bring the concepts of TIs into photonics (optical and near infrared frequencies), without relying on the aforementioned gyro-optic effects, which are weak in those frequency ranges. In 2013, the first PTIs were demonstrated, which displayed topological protection of transport (of light) against defects and disorder [RZP⁺13]. That system relied on periodic modulation, which is the essential feature of Floquet topological insulators⁴. The first photonic Floquet topological insulators relied on a HC lattice of coupled waveguides, where the modulation is generated by making the waveguides helical [SB20]. See Fig. 2.3 for the geometry. However, the implementation of such a 3D Floquet system in a genuine 2D time-dependent system is highly nontrivial. Nonetheless, despite the challenges in implementation, photonic analogues of Quantum Hall (QH) phase have the best performance among all photonic topological phases [XYZ21].

Afterwards, numerous other electromagnetic topological systems were proposed and demonstrated, including systems emulating quantum spin Hall effect (QSHE) and quantum valley Hall effect (QVHE). Further information may be found in [OPA⁺19], which is a comprehensive review on PTIs and provides the details of these systems, and [XYZ21] that details the physics behind various types of PTIs.

2.1.1 Integer Quantum Hall Effect

In this section, in order to clarify how TPEMs occur, we examine what happens in the QHE. As in the normal Hall effect, applying a magnetic field

¹The rotation of the plane of polarization of a light beam by a magnetic field

²Time reversal symmetry is the theoretical symmetry of physical laws under the transformation of time reversal, $\mathcal{T} : t \rightarrow -t$

³Gyrotropic media break optical reciprocity and give rise to magneto-optical phenomena such as the Faraday effect. In a gyrotropic medium, the polarization vector undergoes precession around a preferred direction. In the frequency domain, this corresponds to the presence of skew-symmetric off-diagonal components in the μ (permeability) tensor.

⁴Floquet Topological Insulators are topological phases resulting from strong light-matter interaction, or more generally, time-dependent perturbations. These topological phases can be achieved even in materials that natively lack topological states. Therefore, by using light one can achieve topological states similar to those in topological insulators [Tor20].

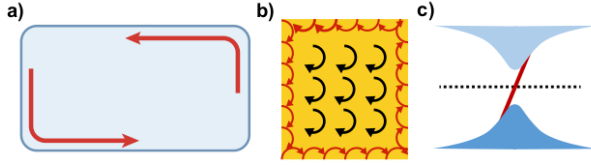


Figure 2.4: Topological insulator in a nutshell. (a) TI: a two-dimensional material that is insulating in the bulk but exhibit perfect conduction on the edge (red arrows). (b) Simplified sketch of the integer quantum Hall effect, which was the first TI. Black: closed cyclotron orbits of the electrons, red: closed orbits are not possible at the edges (Landau energy levels are shifted to higher energies thus forming so-called edge states). (c) Simplified dispersion relation for the QHE, with the red line marking the topological chiral edge states.[SB20]

causes the electrons to spin in cyclotron orbits, with their frequency being determined by the strength of the \mathbf{B} field (see Fig. 2.4 (b)). Under the aforementioned conditions, the quantization of the energy of these orbits (called Landau levels) becomes relevant, with the difference between the allowed energies becoming very large as the field strength increases. When the strength of the \mathbf{B} field varies enough to permit or remove an energy level, there will be a sudden jump in the transverse conductivity by an exact multiple of certain fundamental constants. [SB20]

The Lorentz force opens a bandgap in the dispersion curve, and the edge states are characterized by a single line crossing the gap diagonally. See Fig. 2.4 (c), where the red line marks the dispersion curve of the edge states corresponding to the red lines indicating conduction in (a) and unclosed orbits in (b). Notice that there is only one line; there is no line crossing the gap in the opposite direction, meaning that this is a so-called chiral property⁵. The slope of this line provides the group velocity of any edge excitation. The direction of the magnetic field sets the sign of the slope (which determines the direction of the edge current), and the strength of the magnetic field sets the size of the bandgap.

If disorder is introduced into this structure, the bands will be slightly modified, and the slope of the red line will be slightly altered. However, as long as the strength of the disorder (random variation in the potential) is smaller than a certain value, the edge states will not couple to the bulk states and scattering will not occur. The implication is that *any disorder weaker than (approximately) the bandgap will not cause scattering into the bulk or backscattering*. This is the origin of the topologically protected transport in the QHE, and its key ingredient is the size of the topological bandgap, which determines the degree of topological protection of transport. This is of technological importance due to the potential for reducing power consumption by eliminating sources of loss, as well as simplifying

⁵The edge modes display chiral properties, in the sense that they can propagate only in one direction along the sample boundary but not in the opposite direction [OPA⁺19]. We can say that the time reversal symmetry is broken in this case because the time reversed motion of an electron is not possible.

manufacturing by increasing defect tolerances. These discoveries led to the Nobel Prize in Physics being awarded to Thouless, Haldane, and Kosterlitz in 2016.

Landau level and cyclotron orbit

Here, we consider a Metal Oxide Semiconductor (MOS) device in order to provide some explanation on Fig. 2.4, based on [Lut15]. The application of a magnetic field causes the dimensionality of an electron gas to decrease; the 2D gas within MOS inversion layer (a conducting channel that connects the two n-type regions at the source and drain) is further quantized. If a strong magnetic field is applied normal to the surface, the electrons in the inversion layer are forced to move in cyclotron orbits ($m_{\parallel}^* \dot{\mathbf{v}} = -e[\mathbf{v} \times \mathbf{B}]$, where m_{\parallel}^* is the principal effective mass parallel to the surface of the MOS device (normal to \mathbf{B}), based on the Lorentz force $\mathbf{F} = -e(\mathbf{E} + [\mathbf{v} \times \mathbf{B}])$ with $\mathbf{E} = \mathbf{0}$) with the cyclotron frequency $\omega_c = e|B|/m_{\parallel}^*$. See Fig. 2.5 for an illustration of a cyclotron orbit.

Without a magnetic field, electrons can move freely in parallel to the surface, but such movement is no longer possible when $\mathbf{B} \neq \mathbf{0}$. For the cyclotron orbit, one obtains the so-called Landau levels as the energy eigenvalues within the magnetic field

$$E_n^L = \left(n + \frac{1}{2}\right) \hbar \omega_c, \quad n = 0, 1, 2, \dots,$$

where E_n^L is the n^{th} Landau energy level.

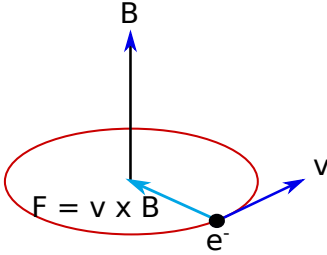


Figure 2.5: Classical description of cyclotron orbit of an electron with velocity v in a magnetic field B

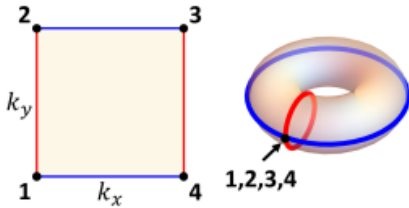


Figure 2.6: The 2D Brillouin zone can be considered as a torus by taking each periodic boundary (red and blue in the figure) and connecting them together [BDZ⁺20].

Importantly, it was found that this discrete behavior could be explained by a special phase called the geometric phase that each electron accumulates as it orbits in cyclotron motion in reciprocal (\mathbf{k}) space. It is shown that the added geometric phase responsible for the quantization is tied directly to the mathematical framework of topological invariants mentioned earlier (explained further in the next section). This is why bandgap materials can be classified by calculating their topological invariant, which is a property of the bulk material [SB20], [BDZ⁺20].

2.1.2 Berry Phase, Berry Connection, and Berry Curvature

The key idea behind topological effects in all areas is the geometric phase, a universal concept that emerges due to the gradual variation of a state in a closed cycle, in many types of parameter spaces. Many phenomena in physics can be attributed to the geometric phase, from the mechanical Foucault pendulums to the polarization in helical waveguides. See more detailed discussion in [BDZ⁺20]. In case of PhCs, for example, a geometric phase known as **Berry phase** can emerge in the momentum space. For any path that traverses an allowed band of a periodic system and does not intersect with any other band, the wavevector \mathbf{k} (Bloch momentum) must vary in closed loops due to the lattice periodicity. In a 2D crystal in

particular, \mathbf{k} traverses the surface of a torus geometry which bounds the entire Brillouin zone (BZ); see Fig. 2.6.

Consider a lattice described by a general eigenvalue problem in momentum space,

$$\mathcal{H}(\mathbf{k})\psi_n(\mathbf{k}) = \lambda_n(\mathbf{k})\psi_n(\mathbf{k}) \quad (2.1)$$

where $\lambda_n(\mathbf{k})$ is the eigenenergy and $\psi_n(\mathbf{k})$ is the normalized eigen wavefunction of $\mathcal{H}(\mathbf{k})$ (Hamiltonian operator) at each \mathbf{k} for the n^{th} band. Gradually changing \mathbf{k} along a given energy band will cause a phase accumulation associated with the slow evolution of $\psi_n(\mathbf{k})$. In most cases, when \mathbf{k} returns back to where it started, this accumulation will result in zero total phase, but special cases can arise where a non-zero geometric phase is added.

To calculate the total Berry phase, we need a means to add up the phase contributions from each small change to the wavefunction. The phase shift between two $\psi_n(\mathbf{k})$ states separated by a small difference $\Delta\mathbf{k}$ can be represented by their inner product, expanded in $\Delta\mathbf{k}$ as a low-order Taylor series as

$$\begin{aligned} \langle \psi_n(\mathbf{k}) | \psi_n(\mathbf{k} + \Delta\mathbf{k}) \rangle &\approx 1 + \Delta\mathbf{k} \langle \psi_n(\mathbf{k}) | \nabla_{\mathbf{k}} | \psi_n(\mathbf{k}) \rangle \\ &\approx \exp(-i\Delta\mathbf{k} \cdot \mathbf{A}_n(\mathbf{k})). \end{aligned} \quad (2.2)$$

In the second approximation, we used the definition of the exponential function $\exp(x) = \sum_{n=0}^{\infty} \frac{x^n}{n!}$ and set $\Delta\mathbf{k} \langle \psi_n(\mathbf{k}) | \nabla_{\mathbf{k}} | \psi_n(\mathbf{k}) \rangle = -i\Delta\mathbf{k} \cdot \mathbf{A}_n(\mathbf{k})$. Here, we can see that $\Delta\mathbf{k} \cdot \mathbf{A}_n(\mathbf{k})$ is the phase shift over $\Delta\mathbf{k}$, and $\mathbf{A}_n(\mathbf{k})$ is the rate of change of the phase shift. $\mathbf{A}_n(\mathbf{k})$ is called the **Berry connection**, or **Berry vector potential**, defined as

$$\mathbf{A}_n(\mathbf{k}) = i \langle \psi_n(\mathbf{k}) | \nabla_{\mathbf{k}} | \psi_n(\mathbf{k}) \rangle. \quad (2.3)$$

Consequently, the **Berry phase** for the n^{th} band is defined as the integral of $\mathbf{A}_n(\mathbf{k})$ over some closed path l in \mathbf{k} -space,

$$\phi_n = \oint_l d\mathbf{k} \cdot \mathbf{A}_n(\mathbf{k}). \quad (2.4)$$

The path l is simply a smooth curve of points within the Brillouin zone (BZ), such as the blue and red curves shown on the right half of Fig. 2.6. If we know what a given wavefunction looks like in the BZ, we could use the equation above to calculate the Berry phase for that path. However, the Berry connection $\mathbf{A}_n(\mathbf{k})$ is not uniquely defined; if a phase change $\zeta(\mathbf{k})$ is added to the eigen wavefunction $\psi_n(\mathbf{k})$, where $\zeta(\mathbf{k})$ is a periodic function with $\zeta(\mathbf{k}_{\text{end}}) = \zeta(\mathbf{k}_{\text{begin}}) + 2m\pi$, $m \in \mathbb{Z}$, the new wavefunction $e^{i\zeta(\mathbf{k})}\psi_n(\mathbf{k})$ is still an eigen wavefunction for $\mathcal{H}(\mathbf{k})$. The Berry connection $\mathbf{A}_n(\mathbf{k})$ is then replaced by $\mathbf{A}_n(\mathbf{k}) - \frac{\partial}{\partial\mathbf{k}}\zeta(\mathbf{k})$ due to (2.3), where it changes its formula with different choice of $\zeta(\mathbf{k})$. The Berry phase, on the other hand, is invariant modulo 2π , since

$$\oint_l d\mathbf{k} \cdot \mathbf{A}_n(\mathbf{k}) \rightarrow \oint_l d\mathbf{k} \cdot \mathbf{A}_n(\mathbf{k}) - \oint_l \frac{\partial}{\partial\mathbf{k}}\zeta(\mathbf{k})d\mathbf{k} = \oint_l d\mathbf{k} \cdot \mathbf{A}_n(\mathbf{k}) - 2m\pi.$$

Thus, it is helpful, especially for numerical purposes, to define a quantity that will be invariant to any arbitrary phase $\zeta(\mathbf{k})$ that we may add. The

Real-space (\mathbf{r})	Momentum Space (\mathbf{k})
Potential $\mathbf{A}_{mag}(\mathbf{r})$	Connection $\mathbf{A}(\mathbf{k})$
Field $\mathbf{B}(\mathbf{r}) = \nabla \times \mathbf{A}_{mag}(\mathbf{r})$	Curvature $\boldsymbol{\Omega}(\mathbf{k}) = \nabla \times \mathbf{A}(\mathbf{k})$
Flux $\Phi_{mag} = \oint_l d\mathbf{l} \cdot \mathbf{A}_{mag}(\mathbf{r})$	Phase $\phi = \oint_l d\mathbf{k} \cdot \mathbf{A}(\mathbf{k})$

Table 2.1: Analogy between real-space (EM) and momentum space (Berry) quantities [GSH17].

Berry curvature, or **Berry flux**, is a quantity that is invariant under such transformation, and can be constructed by taking the curl of the Berry connection,

$$\boldsymbol{\Omega}_n(\mathbf{k}) = \nabla_{\mathbf{k}} \times \mathbf{A}_n(\mathbf{k}). \quad (2.5)$$

Then, using Stokes' theorem ($\oint_l \mathbf{A} \cdot d\mathbf{l} = \iint_S (\nabla \times \mathbf{A}) \cdot d\mathbf{a}$), the Berry phase can be rewritten as the integral of the Berry curvature,

$$\phi_n = \iint_S d^2k \cdot \boldsymbol{\Omega}_n(\mathbf{k}) \quad (2.6)$$

where the integration is over the surface bounded by the path l [BDZ⁺20].

Interestingly, the geometric gauge-independent (modulo 2π) Berry phase, the gauge-dependent Berry vector potential/Berry connection, and the gauge-independent Berry curvature are analogous to the real-space magnetic flux, magnetic vector potential, and magnetic flux density, respectively. This correspondence is summarized in Table 2.1. [GSH17]

2.1.3 Chern Number and Topological Phases in 2D Photonic Crystals

The aforementioned topological invariant in case of electromagnetic systems is called the **Chern number**, after Chinese-American mathematician Shiing-Shen Chern [BDZ⁺20]. It is a quantized (that is, integer) flux of the Berry curvature through the BZ,

$$C_n = \frac{1}{2\pi} \int_{\text{BZ}} d^2k \boldsymbol{\Omega}_n(k_x, k_y), \quad (2.7)$$

where (k_x, k_y) are the axis directions of the 2D 1BZ and $d^2k = dk_x dk_y$. It characterizes the phase accumulation of the geometrical wave $\psi(\mathbf{k})$ as the Bloch wavenumber makes a full circle around the BZ [KS17]. Systems with the same topological invariant are said to be topologically equivalent; that is, they are in the same topological phase. For example, ordinary media like air, metal or Bragg reflectors all have zero Chern numbers, which makes them topologically trivial. When the Chern number is non-zero, the photonic system is said to be **topologically nontrivial**. [LJS14]

The aforementioned TPEMs emerge at the interface between a non-trivial phase and a trivial phase (different terminology is used in case of

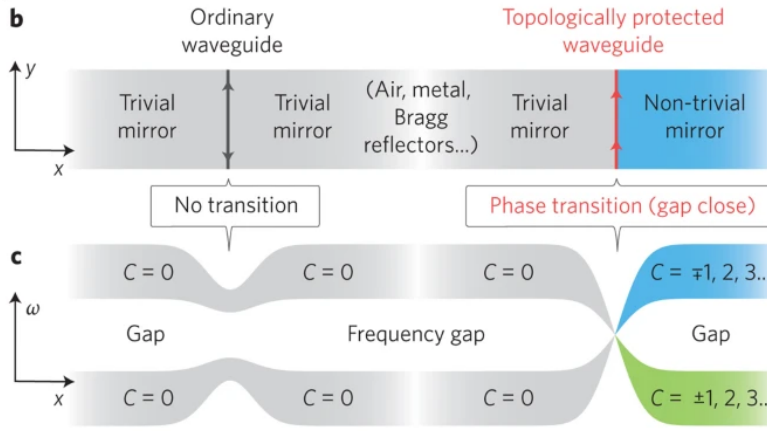


Figure 2.7: b: Two waveguides formed by mirrors of different (right) and same (left) topologies. c: Frequency bands of different topologies cannot transition into each other without closing the frequency gap. A topological phase transition takes place on the right, but not on the left [LJS14].

valley-PTIs, explained later) that are characterized by different Chern numbers [KS17]. What happens at the interface is known as a phase transition. When the two frequency bands both have zero Chern numbers, they can directly connect across the interface without closing the frequency gap. However, when the two systems have different Chern numbers, topology does not allow them to connect to each other directly. A topological phase transition must take place at the interface: this requires the frequency gap to be closed, neutralizing the Chern numbers, and the gap to be reopened. See Fig. 2.7 for a graphical explanation. This phase transition ensures gapless frequency states at the interface: there must exist edge states at all frequencies within the gap of the bulks, i.e., TPEMs. In general, the number of TPEMs equals the difference of the bulk topological invariants across the interface. This is known as the **bulk-edge correspondence**. [LJS14]

2.1.4 Photonic Realizations of Fundamental Topological Models

Fig. 2.8 illustrates the classification map of different approaches to engineering photonic topological states. The three classes of topological systems depicted are: (1) PTIs with broken time-reversal symmetry (Chern-PTIs); (2) time-reversal invariant PTIs that rely on internal symmetries of the electromagnetic field or on spatial symmetries of the structure (spin-PTIs and valley-PTIs); and (3) Floquet PTIs that are periodically modulated in time and/or space. These different categories of photonic topological states partially overlap due to underlying similarities between different topological phases. All these classes of PTIs have been successfully realized in experiments over the past decade [KS17]. In the following, we give overviews of some of the representative works for the first two classes (since we focus on 2D PTIs in this project, Floquet PTIs (3D) are omitted).

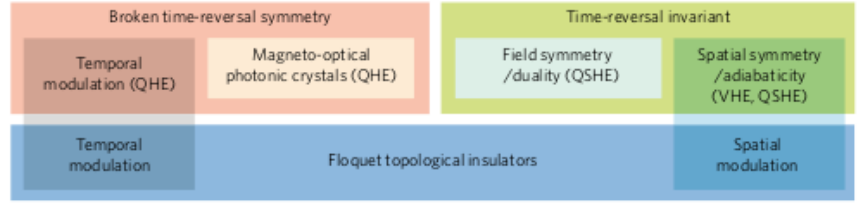


Figure 2.8: Classification scheme of topological orders in 2D photonic systems. The three major classes of photonic topological phases are based on (1) breaking the time-reversal symmetry, (2) conservation of synthetic discrete DoF based on symmetry or adiabaticity, and (3) spatial or temporal modulation. These three classes, correspondingly, emulate the QHE, QSHE and QVHE, and the Floquet effect in condensed-matter systems.[KS17]

Photonic Topological Insulators with Broken Time-reversal Symmetry: Gyromagnetic Photonic Crystals

As a representative of this class, we choose an experimental system that is analogue to the quantum (integer) Hall system (called the quantum Hall PTIs (QH-PTIs) or Chern-PTIs) by [WCJS09] mentioned earlier. Fig. 2.2 illustrates the experimental setup. The 2D square lattice PhC of ferrite rods is sandwiched between two parallel copper plates (yellow) for confinement in the z direction and surrounded with microwave-absorbing foam (grey regions). Two dipole antennas, A and B, serve as feeds and/or probes. A variable-length metal obstacle (orange) with a height equal to that of the waveguide (7.0 mm) is inserted between the antennas to study scattering. A magnetic field is applied along the z direction using an electromagnet (not shown).

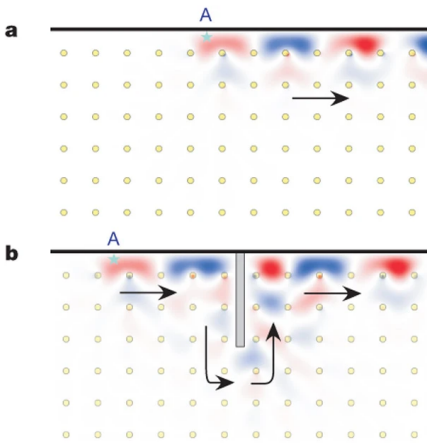


Figure 2.10: CESs and effects of a large scatterer. a: CES field distribution (E_z) at 4.5 GHz in the absence of the scatterer. The black arrow represents the direction of the power flow. b: When the metal obstacle is inserted, forward transmission remains unchanged because backscattering and side-scattering are entirely suppressed.[WCJS09]

When the ferrite rods are magnetized, they manifest gyrotropic permeability (which breaks time-reversal symmetry), and two gaps open as shown in Fig. 2.9 a and b, as the second, third and fourth bands of this photonic crystal acquire Chern numbers of 1, -2 and 1, respectively. The red dispersion line is the gapless chiral edge state (CES) existing inside the second bandgap, which has only positive group velocities at around 4.5 GHz. Numerical simulation results (Fig. 2.10 a) verified that an antenna inside the waveguide can only emit in the forward direction in the bulk frequency gap. There is no increase in the reflection amplitude even after the insertion of the metal scatterer (Fig. 2.10 b). Transmission measurements in Fig. 2.9 c show that the backwards reflection is more than five orders of magnitude smaller than the forwards transmission, indicating the existence of a TPem. [WCJS09]

However, the magneto-optical response is strong only in ferrites at microwave frequencies. This effect is fundamentally weak at all frequencies above terahertz (THz); hence the resultant topological bandgap would be very small, providing essentially no protection of transport. And even at microwave frequencies, the gyromagnetic approach is not practical because of the large size of the required magnets and absorption in ferrites. Therefore, alternative approaches to producing synthetic gauge fields that would

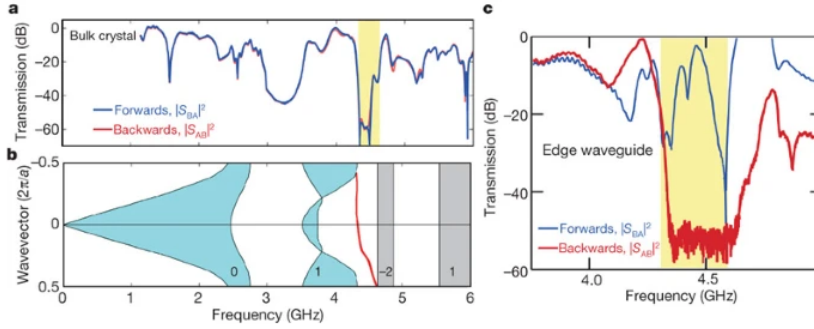


Figure 2.9: a: Forward and backward transmission spectra measured using only the bulk photonic crystal. The bulk transmission is **reciprocal**, with photonic band gaps at 3.3 and 4.5 GHz. b: Calculated projected PhC band structure. The red curve in the second BG between the fourth and fifth transverse magnetic (TM) bands is the CES existing at the interface between the metal cladding and the PhC, c: Measured transmission spectra upon inclusion of the metal cladding and antennas, indicating striking unidirectionality and existence of CES. [WCJS09]

result in finite Berry curvature without using a magnetic field are actively being pursued. [KS17]

Time-reversal Invariant Photonic Topological Phases

Many PTIs have been proposed and demonstrated as analogues of TIs, where the electron spin or valley degree of freedom (DoF) can be simulated by constructing photonic pseudospin or valley pseudospin. Table 2.11 lists some comparisons among QH phase, QSH phase, and QVH phase for intuitive understanding. In QSH systems, helical edge states formed by counter-propagating pseudospin states emerge at the boundary between trivial and non-trivial phases. For QVH systems, so-called valley kink states emerge at the domain wall separating a pair of topologically-distinct VPhCs that form the two domains; that is, the two PhCs have opposite on-site perturbation and are thus two distinct topologically non-trivial phases. For example, their inversion symmetry is broken in opposite ways such that they have opposite unit cell orientation and opposite valley Chern number signs. Both helical edge states and valley kink states counter-propagate, but for the latter, the propagation direction is locked to the valley DoF.

Chern PTIs (QH systems) have many advantages over QSH and QVH systems such as robustness of TPMEs, but the requirement for magneto-optical materials and external magnetic fields places limits on the practical applications, as discussed earlier. QSH and QVH systems do not require breaking time-reversal symmetry, but provides similar features of robustness to disorder or sharp turns, while still being reciprocal [BDZ⁺20]. In this section, an example QSH system is introduced. QVH systems, which is the main topic of this report, will be explained in detail in the next section.

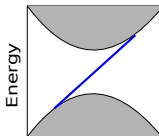
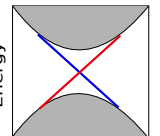
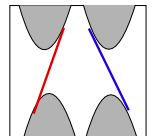
QH phase	QSH phase	Valley-Hall phase
Chern number \mathcal{T} breaking Chiral edge states	Z_2 index/spin chern number Spin-orbit coupling Herical edge states	Valley-Chern number \mathcal{T} breaking Valley kink states
		
Wavevector	Wavevector	Wavevector

Figure 2.11: Comparison between different 2D topological phases. \mathcal{T} : Time-reversal symmetry, \mathcal{I} : Inversion symmetry

For systems emulating QSHE, it has been proposed to utilize a non-periodic array of coupled silicon ring resonators whose diameters are much larger than the wavelength of light [HDLT11], metacrystal (superlattices of metamaterials) and bi-anisotropic materials ([KMT⁺12], [CJN⁺16]) in order to take advantage of a photonic pseudospin DoF while preserving time-reversal symmetry. The latter example is illustrated here; a strong spin-orbit coupling between the pseudospin states is generated by engineering an appropriate bianisotropy or magneto-electric coupling. While the bianisotropy of materials found in nature, such as optically active media containing chiral molecules, is typically small, a very large value can be obtained in metamaterial structures containing, for example, split-ring resonators. The key signature of this photonic QSHE quantum spin Hall effect is the appearance of robust polarization-dependent edge states (“spin”-polarized transport).

[CJN⁺16] experimentally demonstrated this effect for a uniaxial hexagonal metacrystal of nonresonant meta-atoms sandwiched between two metallic plates, where the effective bianisotropy arises from field inhomogeneities. See Fig. 2.12 for geometric arrangement of metallic rods at different positions inside the parallel plate waveguide.

2.2 Valley-Photonic Topological Insulators

Now that we have given a general classification of PTI systems, we clarify what valleys are in photonics and then review the structures and properties of valley-PTIs in detail through an example study.

2.2.1 Valleys in Photonics

A valley generically emerges at high-symmetry points of the BZ and refers to a local minimum in the conduction band or a local maximum in the valence band. An electron in a lattice is endowed with a valley DoF that specifies the valley that the electron occupies, in addition to charge and spin.

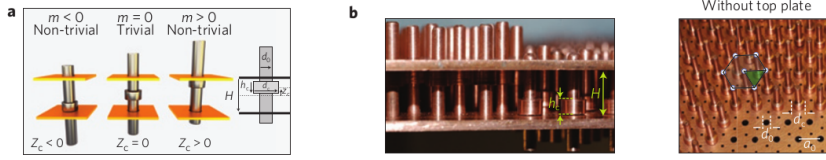


Figure 2.12: Reconfigurable metacrystal. a: Displacing a metallic collar relative to the two metal plates of a waveguide introduces an effective bianisotropy, coupling the electric and magnetic fields. Shifting a collar from the “down” to “up” position (Z_c) reverses the sign of the term m that indicates topological transition, leading to opening of a gap at the Dirac cone, once these rods are arranged into a hexagonal or triangular lattice. b: Photograph of the experiment, in which collars in a triangular array can be moved up and down to create arbitrary and reconfigurable topological domain walls (side view and top view of the metacrystal with the top copper plate and some rods removed to reveal the periodic arrangement of the rods and collars).

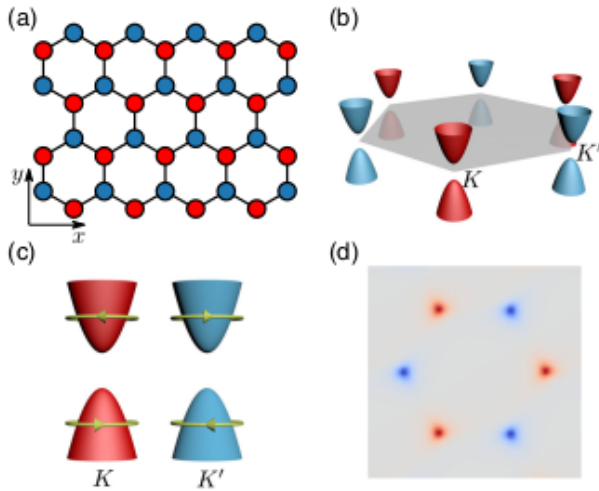


Figure 2.13: Valley-contrasting physics. (a) A honeycomb lattice with only nearest-neighbor coupling. Here, red and blue sites have different on-site energies. (b) Illustration of Dirac cones located at the corners of 1BZ. Here, the gray hexagon denotes the 1BZ zone, and the red (blue) color indicates the Dirac cones at K (K'). (c) The Bloch states at opposite valleys exhibit opposite self-rotating direction, as indicated by the yellow arrows. This leads to valley-locked orbital magnetic moments. (d) Berry curvature distribution. Here, the gray color corresponds to zero Berry curvature, and the red (blue) color corresponds to positive (negative) nonzero values. As shown, Berry curvature is concentrated at the valleys and takes opposite values at opposite valleys. [XYZ21]

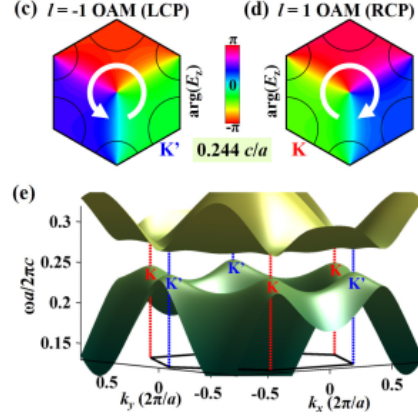


Figure 2.15: Valley-contrasting OAM in a VPhC. Valley-contrasting chiral OAM and the phase distributions of E_z at (c) the K' and (d) K point. (e) 3D bulk band structure, illustrating the complete gap and two inequivalent but time-reversal valleys. [CZCD17]

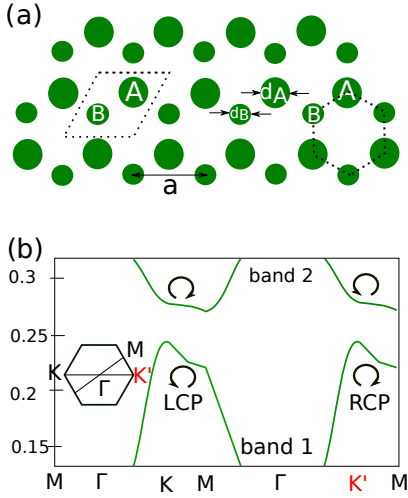


Figure 2.14: (a) Schematic of the valley-PhC with the unit cell of two silicon rods embedded in an air background, i.e., A and B rods in the dashed rhomboid or hexagon. The rod diameters are $d_A = 0.5a$ and $d_B = 0.38a$, where a is the lattice constant. (b) The two lowest bulk bands of TM modes, in which four valley states carrying intrinsic OAM are marked by either counterclockwise or clockwise arrows.[CZCD17]

The configuration shown in Fig. 2.13 (a) describes a graphene lattice with two sublattices (colored in red and blue) having different on-site energies (broken inversion symmetry). This model has the bulk energy dispersion near the two valleys (corners of the hexagonal BZ, labeled K and K' in Fig.2.13 (b)), where two massive Dirac cones are located. Although the two valleys look similar in terms of dispersion, they, in fact, behave very differently. By inspecting the Bloch states near the two valleys, one can find that the Bloch states are self-rotating in phase. Moreover, this self-rotation at different valleys has opposite directions, as shown in Fig. 2.13 (c). This behavior corresponds to valley-dependent orbital magnetic moments for electrons, and this spin-like magnetic momentum is thus named “valley pseudo-spin.” In classical wave systems, similar vortex Bloch states with valley-dependent orbital angular momentum (OAM) can be found. Moreover, the Berry curvature exhibits valley-contrasting physics as well, as shown in Fig. 2.13 (d).

2.2.2 An Example Study of Valley-Photonic Topological Insulators

Here, we introduce a study by [CZCD17], representing valley-PTIs that emulate the QVHE. As shown in Fig. 2.14 (a), their valley-PTI has a graphene-like lattice and a unit cell consisting of two silicon rods having different diameters, embedded in an air background. Because of the inversion asymmetry, the bulk states can split at the two inequivalent but time-reversal symmetric valleys, i.e., K and K' points (explained above), leading to a complete band gap throughout the entire BZ (Figs. 2.14 (b) and 2.15 (e)).

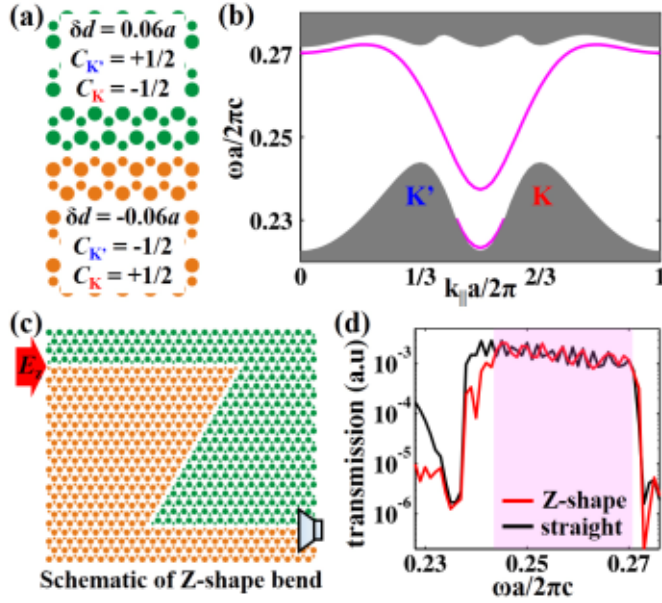


Figure 2.16: Broadband robust transmission and valley-dependent edge states. (a) Schematic of the edge constructed by valley PhCs (b) Valley-dependent edge states, including one with negative velocity (c) Schematic of the Z-shape bend. (d) Transmission spectra for the Z-shape bend (red) and the straight channel (black) and broadband robust transmission are found from $0.244c/a$ to $0.272c/a$. [CZCD17]

Valley-chirality locking

The OAM term is characterized by topological charge

$$l = \oint_L \nabla[\arg\{E_z\}]ds/2\pi,$$

where L is a closed contour surrounding the unit cell center. In this way, the E_z phases of the the K' valley state are anticlockwise decreasing with a circular OAM with $l = -1$ around the central point [Fig. 2.15 (c)]. In contrast, the E_z phases of the K valley state are reversed to be clockwise decreasing, and thus the E_z field has a circular OAM with $l = 1$ [Fig. 2.15 (d)]. The OAM with $l = -1$ and $l = 1$ can be denoted as left-handed circular polarized (LCP) and right-handed circularly polarized (RCP) OAM, respectively.

The valley dependence of OAM chirality can be used to achieve unidirectional excitation of valley chiral states by external sources with proper chirality. That is, the photonic valley is locked to the chirality of excited light, i.e., LCP light couples to the K' -valley mode, while RCP light couples to the K -valley mode. We will demonstrate this valley-chirality locking in Section 5.3.

Two pairs of valley states exist at the frequencies of $0.244c/a$ and $0.272c/a$ at the K and K' points. These separated photonic valley states show “chirality,” as they have intrinsic circular-polarized OAM. This can be verified by the phase distribution of E_z (i.e., $\arg\{E_z\}$) shown in Fig. 2.15 (c), (d), where we can see that the phase profile increases anticlockwise/clockwise by 2π around the center of a unit cell. Such optical vortex is related to valley pseudospin in an electronic system, and thus can be termed as a “photonic valley DoF”.

The Chern number of PTIs called valley Chern number is calculated differently as shown below, to achieve a nonzero integer. Fig. 2.16(a) shows the schematic of an edge constructed by two VPhCs; notice that the structure in orange color has so-called topological indices with signs opposite to those of the structure in green color. The difference of topological indices between the two VPhCs (called valley-Chern number) are ∓ 1 at the K/K' valley points. This leads to the valley-dependent edge states, i.e., one edge state with negative velocity at the K' valley and one with positive velocity at the K valley (Fig. 2.16(b)).

Valley-Chern number

The possible values of Berry curvature are constrained by symmetries. In the presence of the time-reversal symmetry, the distribution of Berry curvature must satisfy: $\Omega(\mathbf{k}) = -\Omega(-\mathbf{k})$. In addition, the inversion symmetry requires $\Omega(-\mathbf{k}) = \Omega(\mathbf{k})$. Thus, in the presence of time-reversal symmetry, the Chern number is always zero for all bands. In that sense, this valley system is topologically trivial, carrying no topological charge.

However, the absence of inversion symmetry means that the Berry curvature does not have to vanish everywhere in the BZ. In fact, the Berry curvature may take nonzero values around two valleys, taking opposite signs at opposite valleys. To establish a bulk-boundary correspondence, one can define a bulk quantity called a valley-Chern number $C_v = C_K - C_{K'} = 2C_K$, where C_K and $C_{K'}$ are called topological indices, each taking a positive or negative half-integer. This definition is similar to Chern number except that the integration of Berry curvature is done only around the valleys. [XYZ21]

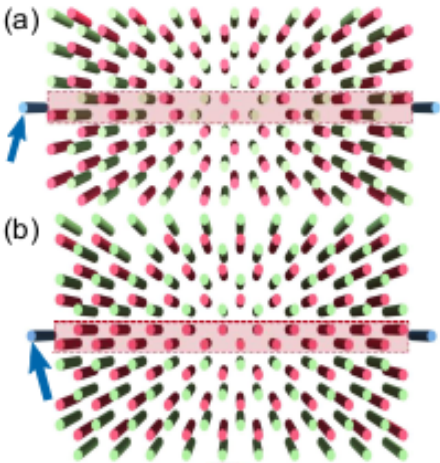


Figure 2.17: (a) Schematic diagram of inversion-symmetry-broken honeycomb lattices with armchair and (b) zigzag edge domain walls. Red and green waveguides indicate different refractive index, and blue indicates straw waveguides. Red shaded regions indicate domain walls. [NHCR17]

The edge dispersions in Fig. 2.16 (b) have curves similar to line-defect bands of topologically trivial PhCs, and the upper and lower bulk bands are not connected. This is a consequence of the Chern number of the valley-PTI being zero if calculated in the same way as for QH and QSH phases. However, they can still be employed for constructing a waveguide with broadband transport robustness against sharp corners, as the intervalley scattering is suppressed due to the vanishing field overlapping between two valley states. Fig. 2.16 (c) and (d) show that a broadband robust transport is achieved and that the transmittance of the Z-shape bend (red) is as high as that of a straight channel (black). [CZCD17].

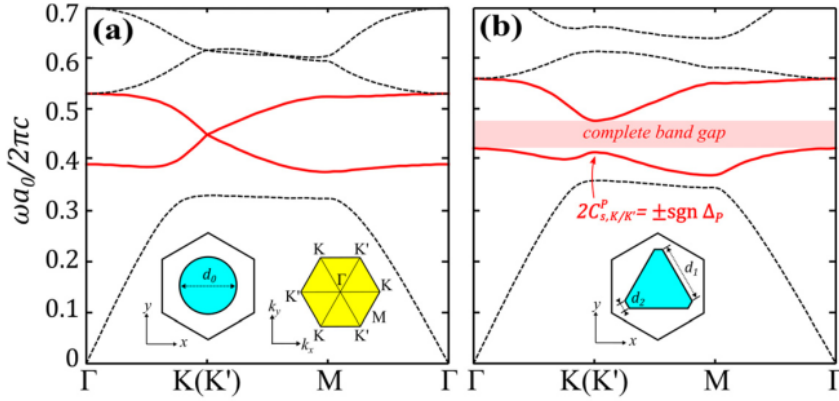


Figure 2.18: Photonic band structure and electromagnetic modes of (a) unperturbed and (b) perturbed photonic structures. Red lines: the relevant photonic bands forming a Dirac points at the K (K') point. [MS16]

2.2.3 Recent Development of Valley-Photonic Topological Insulators

In this section, we review recent development of valley-PTIs formed by dielectric materials alone. For a review of other types of valley-PTIs, see [LSH⁺21] and [XYZ21]. Various ways of breaking the inversion symmetry have been proposed. The first design of a valley-PTI was proposed in [MS16]. In their design, dielectric rods are arranged into a triangular lattice. When dielectric rods are in circular shape, the second and the third transverse electric (TE) bands form Dirac points at K and K' valleys. As the rods are deformed into triangular shape, as shown in Fig. 2.18, a bandgap opens, and a valley-Hall phase emerges as the rotational symmetry is reduced from 6 to 3-fold. Another popular valley-PTI design is based on the photonic HC lattice shown in Section 2.1.4 ([CZCD17]). In both designs, inversion symmetry is broken by tuning some geometrical parameters that are easy to control.

One can also tune material parameters, such as refractive index, to break inversion symmetry to obtain a VPhC. This approach was demonstrated by [NHCR17] using a laser-written waveguide lattice. As shown in Fig. 2.17, this system consists of coupled optical waveguides, forming a HC lattice. The refractive index of each waveguide can be controlled independently through the fabrication process. Thus, a refractive index detuning (deviation from the desired or original value) between the two sublattices can be introduced to create a valley-Hall lattice.

Valley-PTIs in the form of PhC slabs are increasingly being integrated on chips. Usually, realizing nanophotonic systems with low backscattering at sharp bends is a great design challenge. The promise of topologically protected photonic states supporting unhindered transport around defects and sharp corners without the need for optimization is thus especially interesting for on-chip applications [ABB⁺21]. [HLY⁺19] used the

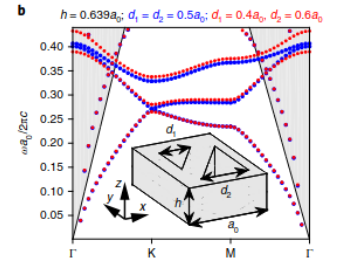


Figure 2.19: Band structures and the unit cell of the PhC slab [IWT⁺19]

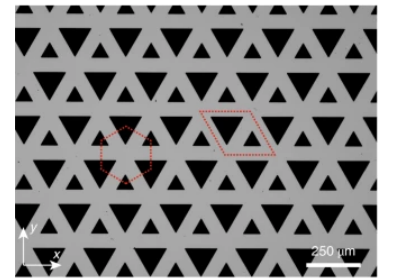


Figure 2.20: An optical image of the fabricated sample. The red dashed lines show Wigner-Seitz and unit cells. [YY⁺20]

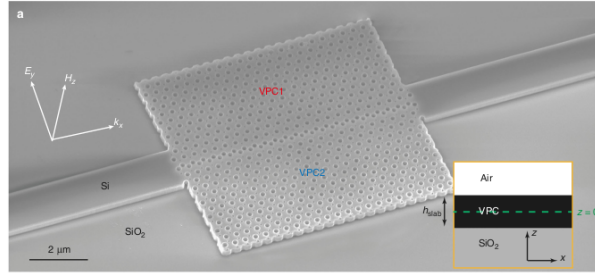


Figure 2.21: Scanning-electron-microscope image of the fabricated SOI valley photonic crystals [HLY⁺19]

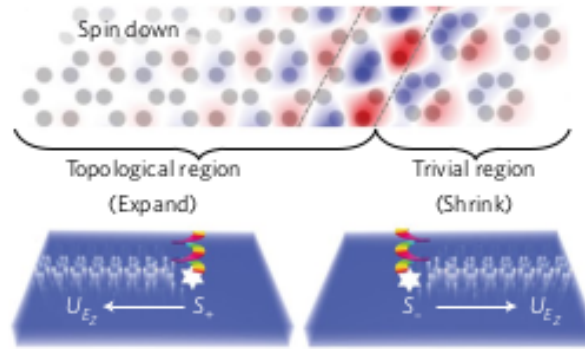


Figure 2.23: 2D geometry and field distribution of the edge state confined to the domain wall between trivial and non-trivial regions obtained by shrinkage (right) and expansion (left) of the dielectric hexamer constituting the unit cell of the crystal. S_+ and S_- are circularly left and circularly right polarized sources, respectively, and U_{E_z} is the Poynting vector. [WH15]

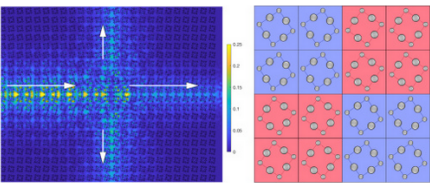


Figure 2.22: A three-way splitter designed on a square lattice using accidental degeneracies and geometry (right panel). The quadrants differ in only the rotation given to the inclusion arrangement within it (left panel). [MCG19]

same method of breaking the inversion symmetry as [CZCD17] to realize topological transport in a silicon-on-insulator (SOI) valley PhC slab (see Fig. 2.21). [IWT⁺19] also used PhC slabs and achieved TPEMs at NIR frequency range. The photonic crystal structure is built from unit cells shown in Fig. 2.19 and consists of a HC lattice with two inverted equilateral triangular air holes per unit cell. [YYY⁺20] experimentally demonstrated robust THz topological valley transport on an all-silicon chip using valley-PTIs having graphene-like lattice shown in Fig. 2.20.

[WH15] introduced a different approach, where the valley DoF was used as a pseudospin to emulate valley-PTIs in a photonic system. They used a particular symmetry reduction of the hexagonal lattice of dielectric rods—shrinking or expansion of a group of six nearest Si rods as illustrated in Fig. 2.23—the transformation that changes the shape of the unit cell and the BZ of the lattice.

These systems introduced here reveal the simplicity in constructing photonic valley-Hall systems, and most subsequent works follow similar design

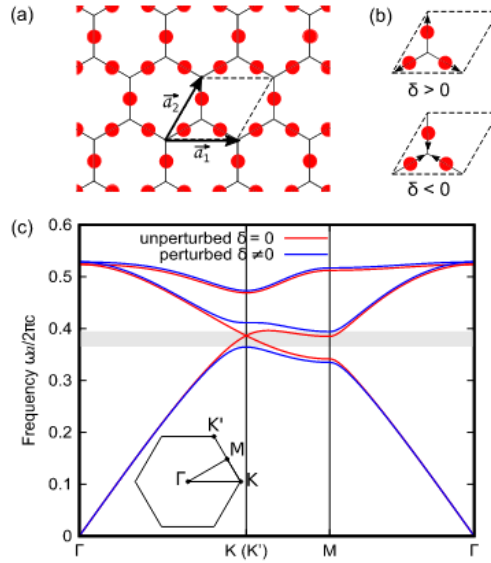


Figure 2.24: (a) Schematic of a kagome lattice. (b) Perturbations are considered by putting the rods further away (upper) or closer (bottom) to each other, represented by the arrows. (c) Band structure of the kagome lattice for the unperturbed (solid red line) and perturbed (solid blue line) cases. [WSHO20]

principles. However, valley-Hall lattices are not limited to these designs and can be realized in other settings, such as the kagome lattice [WSHO20] (see Fig. 2.24 for the lattice structure and band structure), the square lattice [MCG19] (see Fig. 2.22 for the lattice structure and achieved three-way splitter), and even amorphous systems. Due to this simplicity and flexibility in design, valley-PTIs have been widely studied, and various new phenomena and applications have been discovered. [XYZ21]

2.3 Designing Valley-Photonic Topological Insulators: A Summary

This chapter gave an overview of the development in topological photonics and clarified the characteristics/features of valley-PTIs in comparison with other types of PTIs. We summarize important features of valley-PTIs in this summary.

Valley-PTIs exploit an inherent DoF of hexagonal lattices, which can be used to mimic robust edge state propagation of Chern PTIs. For example, a graphene-like lattice, e.g., a HC lattice structure, possess the Dirac point at the K (K') point, and such a lattice can be constructed, for example, by a unit cell containing two rods of equal radius (A and B sites).

Unlike the Chern PTIs (and spin PTIs) where topological edge modes can be formed at the interface between a nontrivial lattice and a trivial

lattice, the valley-polarized topological kink states only exist at the domain wall separating two inversion-symmetry partner VPhCs. Therefore, when constructing a valley waveguide, there must always be a pair of complementary VPhCs. Such VPhCs are formed by breaking the inversion symmetry by differentiating the A and B rods in the unit cell in the opposite manner. This will lift the degeneracy and a controllable bandgap can be achieved (a guided mode in a bandgap guarantees propagation without scattering into the bulk), and the domain wall will have A sites adjacent to A sites, or B sites adjacent to B sites.

In accordance with the bulk-edge correspondence, the number of kink modes at each valley is determined by the valley Chern number, i.e., difference of topological indices C_v above and below the bandgap: $C_{v,1}^K - C_{v,2}^K = 1$ and $C_{v,1}^{K'} - C_{v,2}^{K'} = -1$, where each value corresponds to a single valley (explained in more details in Section 4.2). The differing signs here could be interpreted as the sign of the group velocity of the forward and backward propagating modes at the two valleys, respectively.

The valley Chern number being non-zero means that the two VPhCs form a PTI and the kink states are topologically protected. Since the kink states are coupled to K or K' valleys, these kink states are the most robust in the directions where the valleys are clearly defined (i.e. $\Gamma \rightarrow K$ or $\Gamma \rightarrow K'$ directions). [BDZ⁺20]

CHAPTER 3

Computational Methods

This chapter presents the three main MatLab programs developed for this project, in order to calculate photonic band structures and bandgaps, guided modes formed within the bandgaps, and electric field magnitude distribution in 2D VPhCs and valley-PTIs. Throughout the project, we deal with TM mode (*s*-polarization) only (TM modes have the electric field \mathbf{E} normal to the plane, i.e., $\mathbf{E} = \hat{\mathbf{z}}E(\mathbf{r}) = \hat{\mathbf{z}}E(x, y)$, and the magnetic field \mathbf{H} in the plane, $\mathbf{H}(\mathbf{r}) \cdot \hat{\mathbf{z}} = 0$). The discussion in this section is mainly based on [Søn19], [Søn21], and [Ben21].

3.1 Modeling Band Structures of Honeycomb Photonic Crystals Using Plane-wave-expansion Method

We use the plane-wave-expansion method (PWE method) to calculate band diagrams of 2D VPhCs, in particular HC lattice VPhCs whose unit cell contains cylindrical silicon rods having different radii (no defects are introduced). In this method, the electric/magnetic field expressed in terms of Bloch waves as well as the dielectric function are expanded in terms of their Fourier series components along the reciprocal lattice vectors. They are then inserted into the Helmholtz equation/master equation derived from Maxwell's equations to form an eigenvalue problem to be solved. This MatLab program is referred to as Program 1 throughout the report. Here, only new additions to the work done by the author in P9 is explained, since this method is well-known among the photonic crystal community.

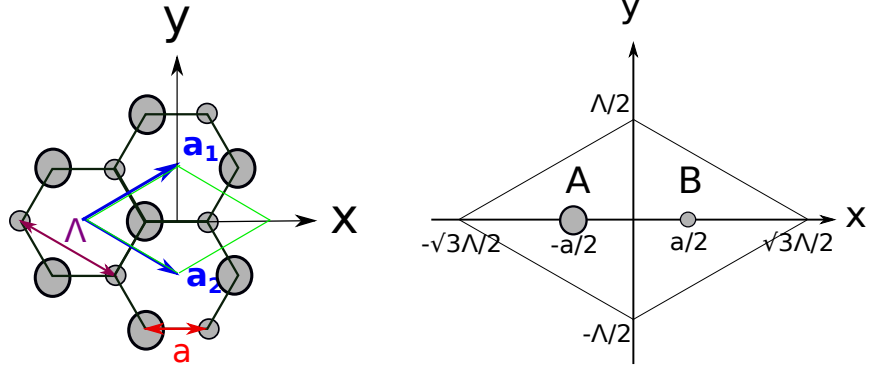


Figure 3.1: Left: primitive vectors \mathbf{a}_1 and \mathbf{a}_2 of the crystal lattice having the length Λ , with unit cell marked in green, Right: Unit cell having sublattices A and B. a is the distance between the centers of nearest neighbor rods.

3.1.1 Structure Factor and Fourier Coefficients for Honeycomb Lattice

In order to form a topologically-distinct VPhC pair, we break the inversion symmetry of a HC lattice PhC by changing the rod radius of one of the sublattices with respect to the other. This necessitates constructing a special structure factor.

Fig. 3.1 shows the geometry and unit cell of a 2D PhC with HC lattice of cylindrical dielectric rods, surrounded by air. The primitive vectors \mathbf{a}_1 and \mathbf{a}_2 of the crystal lattice have the length Λ . The rods at the two sublattices A and B, separated by length a , in one unit cell have different radii in order to break the inversion symmetry. Here, the rods have the dielectric constant ε_a , the dielectric function of air is ε_b , and the rod radius of sublattice A/B are r_A/r_B .

The primitive vectors of the crystal lattice are

$$\mathbf{a}_1 = \frac{\Lambda}{2}(\sqrt{3}\hat{\mathbf{x}} + \hat{\mathbf{y}}) \quad \text{and} \quad \mathbf{a}_2 = \frac{\Lambda}{2}(\sqrt{3}\hat{\mathbf{x}} - \hat{\mathbf{y}})$$

and the primitive vectors of the reciprocal lattice (not shown in the figure) are

$$\mathbf{b}_1 = \frac{2\pi}{\sqrt{3}\Lambda}(\hat{\mathbf{x}} + \sqrt{3}\hat{\mathbf{y}}) \quad \text{and} \quad \mathbf{b}_2 = \frac{2\pi}{\sqrt{3}\Lambda}(\hat{\mathbf{x}} - \sqrt{3}\hat{\mathbf{y}}).$$

The photonic band structure can be investigated by modifying the MatLab programs for a HC lattice having cylindrical rods with identical radius we developed in P9 using the PWE method. When rods in two different sublattices have different radii, the structure factor is calculated as the sum

over the two rods in the unit cell [GYG⁺17]:

$$\begin{aligned} S(\mathbf{G}_{m,n}) &= \frac{1}{A_{\text{cell}}} \left(\int d^2r S_A(\mathbf{r}) e^{-i(\mathbf{G}_{m,n} \cdot (\mathbf{r} + \mathbf{u}_A))} + \int d^2r S_B(\mathbf{r}) e^{-i(\mathbf{G}_{m,n} \cdot (\mathbf{r} + \mathbf{u}_B))} \right) \\ &= \frac{1}{A_{\text{cell}}} \left[e^{-i\mathbf{G}_{m,n} \cdot \mathbf{u}_A} \int d^2r S_A(\mathbf{r}) e^{-i(\mathbf{G}_{m,n} \cdot \mathbf{r})} \right. \\ &\quad \left. + e^{-i\mathbf{G}_{m,n} \cdot \mathbf{u}_B} \int d^2r S_B(\mathbf{r}) e^{-i(\mathbf{G}_{m,n} \cdot \mathbf{r})} \right] \end{aligned} \quad (3.1)$$

$$\begin{aligned} &= \frac{1}{A_{\text{cell}}} \left[e^{-i\mathbf{G}_{m,n} \cdot \mathbf{u}_A} \left(\frac{2\pi r_A}{G_{m,n}} J_1(G_{m,n} r_A) \right) \right. \\ &\quad \left. + e^{-i\mathbf{G}_{m,n} \cdot \mathbf{u}_B} \left(\frac{2\pi r_B}{G_{m,n}} J_1(G_{m,n} r_B) \right) \right] \end{aligned} \quad (3.2)$$

where $\mathbf{G}_{m,n} = m\mathbf{b}_1 + n\mathbf{b}_2$, $\mathbf{u}_A = -\frac{a}{2}\hat{\mathbf{x}}$ and $\mathbf{u}_B = \frac{a}{2}\hat{\mathbf{x}}$ are the relative positions of the rods, and $J_1(\cdot)$ is the Bessel function of first kind. Furthermore, $S_A(\mathbf{r})$ and $S_B(\mathbf{r})$ are indicator functions defined as

$$S_A(\mathbf{r}) = \begin{cases} 1 & \text{for } |\mathbf{r} - \mathbf{u}_A| \leq r_A \\ 0 & \text{for } |\mathbf{r} - \mathbf{u}_A| > r_A \end{cases}$$

and

$$S_B(\mathbf{r}) = \begin{cases} 1 & \text{for } |\mathbf{r} - \mathbf{u}_B| \leq r_B \\ 0 & \text{for } |\mathbf{r} - \mathbf{u}_B| > r_B. \end{cases}$$

See [Sak05] for the step from (3.1) to (3.2) (evaluating the integral in polar coordinate will give the Bessel function). The filling factor becomes $f_i = 2 \cdot \frac{2r_i^2\pi}{\sqrt{3}\Lambda^2}$, where $i \in \{A, B\}$. Thus, for $\mathbf{G}_{m,n} \neq 0$, the Fourier coefficients in case of TE polarization are given by

$$\tilde{\eta}_{m,n} = \left(\frac{1}{\varepsilon_a} - \frac{1}{\varepsilon_b} \right) \left[f_A e^{-i\mathbf{G}_{m,n} \cdot \mathbf{u}_A} \frac{J_1(G_{m,n} r_A)}{G_{m,n} r_A} + f_B e^{-i\mathbf{G}_{m,n} \cdot \mathbf{u}_B} \frac{J_1(G_{m,n} r_B)}{G_{m,n} r_B} \right], \quad (3.3)$$

where $G_{m,n} = |\mathbf{G}_{m,n}|$. For $\mathbf{G}_{n,m} = 0$, we take the average of the sublattices:

$$\tilde{\eta}_{0,0} = \frac{1}{2} \left[\left(\frac{f_A}{\varepsilon_a} + \frac{1-f_A}{\varepsilon_b} \right) + \left(\frac{f_B}{\varepsilon_a} + \frac{1-f_B}{\varepsilon_b} \right) \right]. \quad (3.4)$$

For TM polarization, we simply change $\frac{1}{\varepsilon_j}$ to ε_j , where $j \in \{a, b\}$. For the detailed discussion of the PWE method, see [Søn19], [Sak05], and [Ben21].

3.2 Iterative Method Taking Advantage of the Fast Fourier Transform and PWE Theory

This method takes advantage of Fast Fourier Transform (FFT) and variational theory, and is a fast and efficient method for solving the electromagnetic wave equation for large numerical problems of light propagation

[Søn21]. We use this method in order to model band diagrams and defect modes formed within the PBGs and electric field distribution of valley-PTIs with various types of domain walls. It is used to calculate eigenfunctions used in Chern number calculation as well. The software using this method is referred to as Program 2 throughout the report. See Appendix A.2 for some explanation of FFT.

3.2.1 Iterative Method in a Nutshell

In this method, we first express the electric field and dielectric constant of the periodic structure as Fourier series, just as in the PWE method. Based on this we obtain an expression of the magnetic field, so that we can take advantage of the variational theory in quantum mechanics to find the eigenfunction corresponding to the least energy in a self-consistent manner. Here, it is exploited that the wave equation of the magnetic field (not the Helmholtz equation for the electric field), the so-called master equation,

$$\nabla \times \left(\frac{1}{\varepsilon(\mathbf{r})} \nabla \times \mathbf{H}(\mathbf{r}) \right) = \left(\frac{\omega}{c} \right)^2 \mathbf{H}(\mathbf{r}) \quad (3.5)$$

is Hermitian. After finding the smallest eigenfrequency by starting with an arbitrary guess, higher eigenfrequencies can be found by looking for eigenfunctions orthonormal to the first eigenfunction.

This method is particularly useful when analyzing defect modes (including domain walls) using supercells, where it is assumed that the wave functions localized at adjacent defects hardly overlap with each other when the supercell is sufficiently large. This means that a large supercell, and hence a large number of plane waves, is required, making the PWE method inappropriate for defect mode calculation. With the iterative method, the computation time is significantly shorter thanks to the FFT algorithm, and it is also possible to plot the distribution of the electric field magnitude at specific wavevectors and bands, which is useful to visualize localization of light due to defects formed in a PhC.

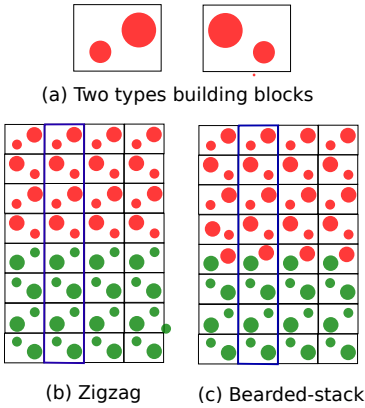


Figure 3.2: (a) Two types of building blocks, (b) zigzag-edge domain wall formed by the two types of building blocks. The supercells are marked with blue lines. Red and green colors distinguish different VPhCs.

3.2.2 Main Steps

Below, we briefly summarize the main aspects of this method.

Setting up Geometries of Various Domain Walls

In P9, we used this method in order to analyze waveguides formed by line-defects in 2D square-lattice PhCs, in which case we obtained one defect band (guided mode) in the PBG. In case of a valley-PTI, we create various types of domain walls formed between two topologically distinct HC-lattice VPhCs whose unit cell contain two cylindrical rods of different radii, such as zigzag-edge, bearded-stack, and armchair-edge as introduced in the Introduction. This can be achieved, for example, by forming two types of building blocks, each containing two rods of different radii, but having different orientation as shown in Fig. 3.2 (a), and combining them to construct supercells that can be repeated in the x - and y -directions several times to represent a 2D

PTI. Fig. 3.2 (b) and (c) show examples of zigzag-edge and bearded-stack domain walls, where the supercell is formed by stacking up the two types of building blocks, making sure to interchange the radii in two different domains. In case of bearded-stack domain wall, it is necessary to create a special unit cell at the interface, but otherwise, the two types of building blocks will do.

In order to discretize 2D rods having circular cross-section with square-shaped elements, we assign a geometric average dielectric constant to each cell using a method similar to Section 3.1.1.

Bloch Wave Vector

We want to plot the eigenvalues as a function of position around the boundary of the irreducible BZ, and we have a rectangular superlattice whose Λ_y is much longer than Λ_x , with 1D translational symmetry. It is thus only necessary to consider k_x/G_x , where k_x is the x component of wavevector and G_x is the reciprocal lattice vector, as the BZ collapses along the y -direction and basically becomes a line along the x -direction [Søn21]. It is important to select the number of plane waves in the x - and y -directions in proportion to the shape of the supercell (i.e., the ratio of Λ_x and Λ_y) to achieve a good resolution.

Iterative Procedure for Finding Eigenvalues and Eigenvectors

In case of a rectangular lattice and s -polarization, the electric and magnetic fields can be written as

$$\mathbf{E}_{\mathbf{k},n}(\mathbf{r}) = \hat{\mathbf{z}}U_{\mathbf{k},n}(x,y)e^{i\mathbf{k}\cdot\mathbf{r}} = \hat{\mathbf{z}} \sum_{m_x,m_y} E_{m_x,m_y,\mathbf{k},n} e^{m_x G_x x + m_y G_y y} e^{i\mathbf{k}\cdot\mathbf{r}} \quad (3.6)$$

$$\mathbf{H}_{\mathbf{k},n}(\mathbf{r}) = \sum_{m_x,m_y} H_{m_x,m_y,\mathbf{k},n} \hat{\mathbf{z}} \times \frac{\mathbf{k} + \hat{\mathbf{x}}m_x G_x + \hat{\mathbf{y}}m_y G_y}{|\mathbf{k} + \hat{\mathbf{x}}m_x G_x + \hat{\mathbf{y}}m_y G_y|} e^{m_x G_x x + m_y G_y y} e^{i\mathbf{k}\cdot\mathbf{r}}, \quad (3.7)$$

where U is a Bloch function, $\mathbf{k} = \hat{\mathbf{x}}k_x + \hat{\mathbf{y}}k_y$, $G_x = 2\pi/\lambda_x$, $G_y = 2\pi/\lambda_y$, and n is the band index used to distinguish between different solutions for the same \mathbf{k} . Using the master equation (3.5), the eigenvalue problem is written as:

$$\hat{\Theta}\mathbf{H}_{\mathbf{k},n}(\mathbf{r}) = \nabla \times \left(\frac{1}{\varepsilon(\mathbf{r})} \nabla \times \mathbf{H}_{\mathbf{k},n}(\mathbf{r}) \right) = \left(\frac{\omega_{\mathbf{k},n}}{c} \right)^2 \mathbf{H}_{\mathbf{k},n}(\mathbf{r}), \quad (3.8)$$

where $\hat{\Theta}$ is Hermitian. We start from setting up an arbitrary trial vector \mathbf{C}' in terms of its array of Fourier coefficients being normalized to unit length. We then use the variational theorem to find the first eigenfunction through a self-consistent iterative procedure, repeatedly recalculating \mathbf{H} and $\hat{\Theta}\mathbf{H}$ until the following condition is satisfied:

$$1 - \frac{\langle \mathbf{H}(\mathbf{r}) | \hat{\Theta}\mathbf{H}(\mathbf{r}) \rangle}{\sqrt{\langle \hat{\Theta}\mathbf{H}(\mathbf{r}) | \hat{\Theta}\mathbf{H}(\mathbf{r}) \rangle} \sqrt{\langle \mathbf{H}(\mathbf{r}) | \mathbf{H}(\mathbf{r}) \rangle}} \leq \delta. \quad (3.9)$$

The calculation of $\hat{\Theta}\mathbf{H}$ can be performed effectively using the MatLab command for the FFT algorithm `fft2`. Care must be taken so that, after calculating the first curl in the reciprocal space (\mathbf{k}), the result is inverse Fourier transformed such that the calculation of $1/\varepsilon(\mathbf{r})$ is performed in real space \mathbf{r} . The result is again Fourier transformed back into reciprocal space to calculate the last curl.

Once the first eigenfunction is found, use the Gram-Schmidt orthogonalization procedure to find the next eigenvector in a subspace orthogonal to the first one:

$$\mathbf{C}'' = \mathbf{C}' - \sum_j \langle \mathbf{H}_j | \mathbf{C}' \rangle \mathbf{H}_j.$$

The search for the next eigenfunction is further restricted by determination of the residual vector to the trial vector, which determines a suitable direction in which to change the trial vectors \mathbf{C}' , and calculation of “kinetic energy” of the residual vector in order to construct a preconditioning operator that reduces the weight of high wave number components in the residual vector [MAB⁺93]. Once the next eigenvector is found, the next trial vector is found as the optimal linear combination of the present and updated vectors.

Data Processing

Once we find the eigenvectors, the electric field magnitude is calculated using the FFT algorithm again using the relation $\mathbf{E}(\mathbf{r}) = \frac{1}{\varepsilon(\mathbf{r})} \nabla \times \mathbf{H}(\mathbf{r})$. We can plot the eigenvalues (in fact, the dimensionless frequency $\omega_{\mathbf{k},n}\Lambda/(2\pi c)$) against the position along the edge of the irreducible BZ, i.e., k_x/G_x . The distribution of the corresponding electric field over the unit cell can be found using Farady’s law and Fourier transform, and then plotted as well. The electric field distribution thus calculated is used for valley Chern number calculation as well.

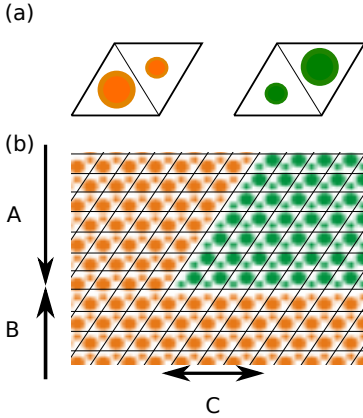


Figure 3.3: Forming a sharp bend. Step 1: In area B, repeat orange unit cells. Step 2: In area A, increment the number of orange cells (decrement the number of green cells) until the desired length C is reached.

3.3 Fast Iterative FFT-based Approach for Solving the GFAIEM

We used the software that combines the Green’s function area integral equation method (GFAIEM) and the fast iterative FFT-based approach ([Søn19], [LLG⁺15]) in order to simulate how the light propagates through a valley-PTI composed of two VPhCs with opposite unit cell orientation. We refer to this software as Program 3. Just like Program 2, Program 3 is suited for analyzing large structures due to the use of the FFT algorithm. See Appendix A.2 for a note on how FFT is taken advantage of in Program 3. Various types of edge domain walls can be formed using a method similar to the one explained in Section 3.2.2, but this time two HC unit cells with opposite orientations shown in Fig. 3.3 (a) are used as building blocks. For example, a sharp corner can be formed with zigzag edge by piling up the two unit cells as shown in Fig. 3.3 (b).

3.3.1 GFAIEM for 2D Photonic Crystals

Throughout this section, we consider situations where a 2D PhC or a PTI (scatterer) having silicon rods in air or air holes drilled in silicon substrate is irradiated by a s -polarized Gaussian beam. A typical situation is illustrated in Fig. 3.4. We want to apply the GFAIEM in order to calculate the electric field at any position in the scatterer or its surrounding, in order to plot the distribution of electric field magnitude. In the GFAIEM, we consider that the silicon is polarized due to an incident field, and the total field at a local position is the sum of the incident field and the radiation from all polarized parts of the scatterer itself [Søn19].

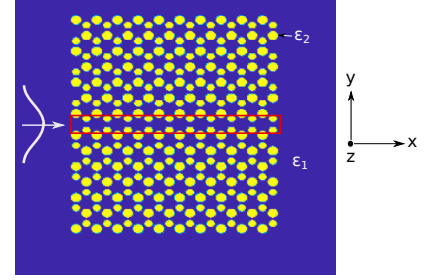


Figure 3.4: Schematic of a PTI having HC array of silicon rods in the air background, being illuminated by a Gaussian beam.

3.3.2 Green's Function Area Integral Equation

We start from Maxwell's equations,

$$\nabla \times \mathbf{E}(\mathbf{r}, t) = -\frac{\partial \mathbf{B}(\mathbf{r}, t)}{\partial t}, \quad (3.10)$$

$$\nabla \times \mathbf{H}(\mathbf{r}, t) = \mathbf{J}(\mathbf{r}, t) + \frac{\partial \mathbf{D}(\mathbf{r}, t)}{\partial t}, \quad (3.11)$$

$$\nabla \cdot \mathbf{D}(\mathbf{r}, t) = \rho(\mathbf{r}, t), \quad (3.12)$$

$$\nabla \cdot \mathbf{B}(\mathbf{r}, t) = 0, \quad (3.13)$$

where \mathbf{D} is the electric displacement field, \mathbf{B} is the magnetic induction field, ρ is the density of free charges, and \mathbf{J} is the density of free currents. Assuming

$$\mathbf{B}(\mathbf{r}) = \mu_0 \mathbf{H}(\mathbf{r}), \quad (3.14)$$

$$\mathbf{D}(\mathbf{r}) = \varepsilon_0 \varepsilon(\mathbf{r}) \mathbf{E}(\mathbf{r}), \quad (3.15)$$

$$\mathbf{H}(\mathbf{r}, t) = \mathbf{H}(\mathbf{r}) e^{i\omega t}, \quad (3.16)$$

where μ_0 is the vacuum permeability, ε_0 is the vacuum permittivity, and $\varepsilon(\mathbf{r})$ is the dielectric function, Maxwell's equations become

$$\nabla \times \mathbf{E}(\mathbf{r}) = i\omega \mu_0 \mathbf{H}(\mathbf{r}), \quad (3.17)$$

$$\nabla \times \mathbf{H}(\mathbf{r}) = \mathbf{J}(\mathbf{r}) - i\omega \varepsilon_0 \varepsilon(\mathbf{r}) \mathbf{E}(\mathbf{r}), \quad (3.18)$$

$$\nabla \cdot \varepsilon_0 \varepsilon(\mathbf{r}) \mathbf{E}(\mathbf{r}) = \rho(\mathbf{r}), \quad (3.19)$$

$$\nabla \cdot \mathbf{H}(\mathbf{r}) = 0. \quad (3.20)$$

From (3.17), we have $\mathbf{H}(\mathbf{r}) = \frac{1}{i\omega \mu_0} \nabla \times \mathbf{E}(\mathbf{r})$. Inserting this into (3.18) and multiplying both sides with $i\omega \mu_0$, we obtain

$$-\nabla \times \nabla \times \mathbf{E}(\mathbf{r}) + k_0^2 \varepsilon(\mathbf{r}) \mathbf{E}(\mathbf{r}) = -i\omega \mu_0 \mathbf{J}(\mathbf{r}). \quad (3.21)$$

Since we are dealing with s polarization, $E(\mathbf{r}) = \hat{\mathbf{z}} E(\mathbf{r})$ and $J(\mathbf{r}) = \hat{\mathbf{z}} J(\mathbf{r})$, and (3.21) reduces to the scalar wave equation

$$(\nabla^2 + k_0^2 \varepsilon(\mathbf{r})) E(\mathbf{r}) = -i\omega \mu_0 J(\mathbf{r}). \quad (3.22)$$

This equation can be solved by using a solution $g(\mathbf{r}, \mathbf{r}')$ (Green's function) to the following equation

$$(\nabla^2 + k_0^2 \varepsilon(\mathbf{r})) g(\mathbf{r}, \mathbf{r}') = -\delta(\mathbf{r}, \mathbf{r}'). \quad (3.23)$$

In terms of the Green's function, a solution to (3.22) is given by the following area integral

$$E(\mathbf{r}) = i\omega\mu_0 \int g(\mathbf{r}, \mathbf{r}') J(\mathbf{r}') d^2 r', \quad (3.24)$$

where the Green's function can be written as

$$g(\mathbf{r}, \mathbf{r}') = \frac{i}{4} H_0^{(1)}(k_0 |\mathbf{r} - \mathbf{r}'|), \quad (3.25)$$

where $H_0^{(1)}$ is the Hankel function of first kind (0th order). If the Green's function satisfying the radiating boundary condition is known for a more general reference geometry, we have

$$(\nabla^2 + k_0^2 \varepsilon_{\text{ref}}(\mathbf{r})) g(\mathbf{r}, \mathbf{r}') = -\delta(\mathbf{r}, \mathbf{r}'), \quad (3.26)$$

and a field solution for the reference geometry satisfies the equation

$$(\nabla^2 + k_0^2 \varepsilon_{\text{ref}}(\mathbf{r})) E_0(\mathbf{r}) = -i\omega\mu_0 J(\mathbf{r}). \quad (3.27)$$

The equation (3.22) is rewritten as

$$(\nabla^2 + k_0^2 \varepsilon_{\text{ref}}(\mathbf{r})) E(\mathbf{r}) = -k_0^2 (\varepsilon(\mathbf{r}) - \varepsilon_{\text{ref}}(\mathbf{r})) E(\mathbf{r}) - i\omega\mu_0 J(\mathbf{r}). \quad (3.28)$$

By subtracting (3.27) and using (3.22), we find

$$(\nabla^2 + k_0^2 \varepsilon_{\text{ref}}(\mathbf{r})) (E(\mathbf{r}) - E_0(\mathbf{r})) = -k_0^2 (\varepsilon(\mathbf{r}) - \varepsilon_{\text{ref}}(\mathbf{r})) E(\mathbf{r}) \quad (3.29)$$

$$= -i\omega\mu_0 J(\mathbf{r}). \quad (3.30)$$

Applying (3.24) to $E(\mathbf{r}) - E_0(\mathbf{r})$, we obtain the GFAIEM for s polarization:

$$\begin{aligned} E(\mathbf{r}) - E_0(\mathbf{r}) &= i\omega\mu_0 \int g(\mathbf{r}, \mathbf{r}') J(\mathbf{r}') d^2 r' \\ \Rightarrow E(\mathbf{r}) &= E_0(\mathbf{r}) + \int g(\mathbf{r}, \mathbf{r}') k_0^2 (\varepsilon(\mathbf{r}) - \varepsilon_{\text{ref}}(\mathbf{r})) E(\mathbf{r}') d^2 r'. \end{aligned} \quad (3.31)$$

We can obtain the electric field at any location by solving this equation. [Søn19]

3.3.3 Fast Iterative FFT-based Approach

The PhCs and PTIs we consider in this project are quite large in geometry: a structure may for example contain 32×32 unit cells, the entire simulation window may be divided into 840×840 elements, and each element may in turn be discretized into 100 sub-elements. In order to reduce the calculation time, we take advantage of the iterative Fast Fourier Transform (FFT) method.

This method takes advantage of the fact that, due to the form of the Green's function, (3.24) can be seen to be in the form of a two-dimensional convolution integral:

$$E(x, y) = \int f(x - x', y - y') h(x', y') dx' dy'.$$

This type of integral can be calculated fast by using the FFT algorithm, due to the convolution theorem. See Appendix A.3. The integral equation can then be solved using iterative methods rather than finding eigenvalues: the memory requirement is much lighter.

In case of s -polarization, with discretization of a rectangular structure into $N = N_x N_y$ square-shaped elements, we convert (3.31) to a discrete convolution:

$$E_{i_x, i_y} - \sum_{j_x, j_y} g_{i_x - j_x, i_y - j_y} k_0^2 (\varepsilon_{j_x, j_y} - \varepsilon_{\text{ref}}) E_{j_x, j_y} = E_{0, i_x, i_y}, \quad (3.32)$$

where each discrete position $\mathbf{r} = (x, y)$ is represented by $0 \leq i_x \leq N_x$ and $0 \leq i_y \leq N_y$ (indices with j is used for \mathbf{r}'). The values of the total field, reference field, dielectric constant, and Green's function are then organized into matrices to form an eigenvalue problem¹:

$$\mathbf{E}_0 = \mathbf{E} - \text{ifft2}(\text{fft2}(\mathbf{g}) .* \text{fft2}(\mathbf{k}_0^2 * (\varepsilon - \varepsilon_{\text{ref}})) .* \mathbf{E}).$$

After the convolution is calculated in the reciprocal space, the result is inverse Fourier transformed into the real space to find the total electric field. See [Søn19] for a more detailed discussion.

3.3.4 Chiral Magnetic Dipole

When we analyze unidirectional coupling in Section 5.3 (unidirectional excitation of valley chiral states by external sources carrying OAM with proper bulk chirality [CJN⁺16]), we need the magnetization source density for a chiral magnetic dipole that can be placed at any position desired. This section explains how to implement such a density into Program 3.

The reference field \mathbf{E}_0 can be obtained from the following magnetization source density for a chiral magnetic dipole located at position \mathbf{r}_0 :

$$\mathbf{M}(\mathbf{r}) = \frac{M}{\sqrt{2}} (\hat{\mathbf{x}} \pm i\hat{\mathbf{y}}) \delta(\mathbf{r} - \mathbf{r}_0), \quad (3.33)$$

where M is the magnitude of the magnetic dipole moment and $\mathbf{d}_{\pm} = \frac{1}{\sqrt{2}} (\hat{\mathbf{x}} \pm i\hat{\mathbf{y}})$ is the chiral dipole moment. Over the time, the dipoles rotate counter-clockwise and clockwise, respectively, because:

$$\Re \left(\frac{M}{\sqrt{2}} (\hat{\mathbf{x}} \pm i\hat{\mathbf{y}}) e^{-i\omega t} \right) = \frac{M}{\sqrt{2}} (\hat{\mathbf{x}} \cos(\omega t) \pm \hat{\mathbf{y}} \sin(\omega t)). \quad (3.34)$$

We start from Maxwell's equations in matter where there is no free charge or free current:

$$\nabla \times \mathbf{E}(\mathbf{r}) = i\omega \mathbf{B}(\mathbf{r}) = i\omega \mu_0 (\mathbf{H}(\mathbf{r}) + \mathbf{M}(\mathbf{r})) \quad (3.35)$$

$$\nabla \times \mathbf{H}(\mathbf{r}) = -i\omega \varepsilon_0 \varepsilon(\mathbf{r}) \mathbf{E}(\mathbf{r}) \quad (3.36)$$

where \mathbf{M} is the magnetization, and $\mathbf{H}(\mathbf{r}) \equiv \frac{1}{\mu_0} \mathbf{B}(\mathbf{r}) - \mathbf{M}(\mathbf{r})$ is used for the first equation. Hereinafter, \mathbf{r} is omitted.

¹Shown in Matlab notation to emphasize the use of element-wise operations

Due to the product rule $\nabla \times (\nabla \times \mathbf{E}) = \nabla(\nabla \cdot \mathbf{E}) - \nabla^2 \mathbf{E}$ and $\nabla \cdot \mathbf{E} = 0$, (3.35) and (3.36) can be combined to yield:

$$\nabla \times (\nabla \times \mathbf{E}) = -\nabla^2 \mathbf{E} \quad (3.37)$$

$$= i\omega\mu_0(-i\omega\varepsilon_0\mathbf{E}) + i\omega\mu_0\nabla \times \mathbf{M} \quad (3.38)$$

$$\Rightarrow (\nabla^2 + k_0^2\varepsilon)\mathbf{E} = i\omega\mu_0\nabla \times \mathbf{M}. \quad (3.39)$$

Since we deal with *s*-polarization (TM), we want the *z*-component, and the relevant part of the wave equation for the reference field is thus given by:

$$(\nabla^2 + k_0^2\varepsilon)E_{0,z} = i\omega\mu_0(\hat{\mathbf{z}} \cdot \nabla \times \mathbf{M}). \quad (3.40)$$

In terms of the Green's function, a solution to (3.40) can be obtained as the following area integral

$$\begin{aligned} E_{0,z}(\mathbf{r}) &= i\omega\mu_0\hat{\mathbf{z}} \int g(\mathbf{r} - \mathbf{r}') \cdot \nabla' \times \mathbf{M}(\mathbf{r}') d^2r' \\ &= i\omega\mu_0\hat{\mathbf{z}} \int (\nabla' \times g(\mathbf{r} - \mathbf{r}')\mathbf{M}(\mathbf{r}') - \nabla'g(\mathbf{r} - \mathbf{r}') \times \mathbf{M}(\mathbf{r}')) d^2r' \\ &= i\omega\mu_0\hat{\mathbf{z}} \cdot \int \nabla g(\mathbf{r} - \mathbf{r}') \times \mathbf{M}(\mathbf{r}') d^2r', \end{aligned} \quad (3.41)$$

where, in the second equality, the product rule $\nabla \times (f\mathbf{A}) = f(\nabla \times \mathbf{A}) - \mathbf{A} \times (\nabla f)$ and the relation $\nabla'g(\mathbf{r} - \mathbf{r}') = -\nabla g(\mathbf{r} - \mathbf{r}')$ are used, and the first term in the second line vanishes since \mathbf{M} is a point emitter.

Inserting (3.25) in (3.41), we obtain the equation to be used for programming:

$$E_0(\mathbf{r}) = i\omega\mu_0 \frac{M}{2} \frac{-i}{4} H_1^{(1)}(k_0|\mathbf{r} - \mathbf{r}_0|) k_0 \left(\pm i \frac{x - x_0}{|\mathbf{r} - \mathbf{r}_0|} - \frac{y - y_0}{|\mathbf{r} - \mathbf{r}_0|} \right). \quad (3.42)$$

3.3.5 Calculation of Magnetic Field Based on Electric Field

In Section 5.3, we attempt to show that high directionality of a chiral magnetic dipole is achieved if it is placed on a location where the dot product between the magnetic field at the location and the chiral magnetic dipole is large. For this purpose, we obtain *x* and *y* components of the magnetic field based on the electric field $\mathbf{E}(\mathbf{r}) = \hat{\mathbf{z}}E(x, y)$ calculated by Program 3. Here we assume that the Green's function used is (opposite sign convention to H_0^1)

$$g^d(\mathbf{r}, \mathbf{r}') = -\frac{i}{4} H_0^2(k_0|\mathbf{r} - \mathbf{r}'|),$$

in which case $\mathbf{H}(\mathbf{r}, t) = \mathbf{H}(\mathbf{r})e^{i\omega t}$. If the Hankel function of the first kind is used ($g^d(\mathbf{r}, \mathbf{r}') = \frac{i}{4} H_0^1(k_0|\mathbf{r} - \mathbf{r}'|)$), the sign is reversed. We obtain $\mathbf{H}(\mathbf{r})$, using Faraday's law (3.17) as

$$\begin{aligned} \mathbf{H}(\mathbf{r}) &= \frac{i}{\omega\mu_0} \nabla \times \hat{\mathbf{z}}E(x, y) \\ &= \frac{i}{\omega\mu_0} \left(\hat{\mathbf{x}} \frac{\partial E(x, y)}{\partial y} - \hat{\mathbf{y}} \frac{\partial E(x, y)}{\partial x} \right). \end{aligned} \quad (3.43)$$

Thus, using the GFAIEM for s polarization (3.31), we get

$$H_x(\mathbf{r}) = \frac{i}{\omega\mu_0} \left[\frac{\partial E_0(x, y)}{\partial y} + \int \frac{\partial g(\mathbf{r}, \mathbf{r}')}{\partial y} k_0^2(\varepsilon(\mathbf{r}') - \varepsilon_{\text{ref}}) E(\mathbf{r}') d^2 r' \right] \quad (3.44)$$

$$H_y(\mathbf{r}) = \frac{-i}{\omega\mu_0} \left[\frac{\partial E_0(x, y)}{\partial x} + \int \frac{\partial g(\mathbf{r}, \mathbf{r}')}{\partial x} k_0^2(\varepsilon(\mathbf{r}') - \varepsilon_{\text{ref}}) E(\mathbf{r}') d^2 r' \right], \quad (3.45)$$

where the derivatives of the Green's function are found to be

$$\frac{\partial g(\mathbf{r}, \mathbf{r}')}{\partial x} = \frac{i}{4} H_1^2(k_0 |\mathbf{r} - \mathbf{r}'|) k_0 \frac{x - x'}{|\mathbf{r} - \mathbf{r}'|} \quad (3.46)$$

$$\frac{\partial g(\mathbf{r}, \mathbf{r}')}{\partial y} = \frac{i}{4} H_1^2(k_0 |\mathbf{r} - \mathbf{r}'|) k_0 \frac{y - y'}{|\mathbf{r} - \mathbf{r}'|}. \quad (3.47)$$

Here the self-interaction term (when $\mathbf{r} = \mathbf{r}'$) vanishes, as it will be a symmetric integral over an odd function. The integral equation in discrete form is expressed as

$$H_{x,i} = H_{x,0,i} + \frac{i}{\omega\mu_0} \sum_j \frac{\partial g(\mathbf{r}, \mathbf{r}')}{\partial y} k_0^2(\varepsilon_i - 1) E_i \quad (3.48)$$

$$H_{y,i} = H_{y,0,i} - \frac{i}{\omega\mu_0} \sum_j \frac{\partial g(\mathbf{r}, \mathbf{r}')}{\partial x} k_0^2(\varepsilon_i - 1) E_i. \quad (3.49)$$

The dot product between the magnetic field and the dipole \mathbf{d}_\pm is then obtained as:

$$(\hat{\mathbf{x}}H_x + \hat{\mathbf{y}}H_y) \cdot (\hat{\mathbf{x}} \pm i\hat{\mathbf{y}}) = H_x \pm iH_y. \quad (3.50)$$

3.3.6 Summary

This chapter explained the three computational methods we used in order to develop basic programs needed to model 2D VPhCs and valley-PTIs. We modified the programs to analyze various geometries, calculate transmission, directionality/efficiency of UDC etc. as needed. They served their purposes satisfactory, except that the computational time of Program 3 is rather long in spite of the use of FFT, especially for larger structures. It will be necessary to find/develop a better algorithm for more efficient analysis in the future.

CHAPTER 4

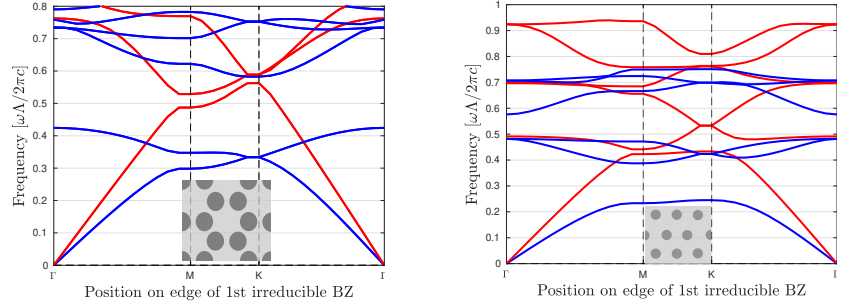
Valley Photonic Topological Insulators

Chapter 2 gave a brief review of the development of topological photonics and an overview of the main features of valley-PTIs. The previous chapter then gave a short review of the calculation tools at our disposal. This chapter first shows how the degeneracy of a topologically trivial HC lattice PhC is lifted by breaking its inversion symmetry. It then explains how to calculate the valley Chern numbers numerically, through an example calculation. Finally, it introduces the valley-PTI to be studied in this project and shows the photonic band structures and electric field magnitude distribution that illustrate that the valley-PTI actually achieves topologically protected kink states.

4.1 Breaking Inversion Symmetry of Honeycomb Lattice Photonic Crystals

In this section, we demonstrate that breaking the inversion symmetry of a HC lattice with dielectric cylindrical rods lifts the degeneracy at the valley points and a PBG is formed, using Program 1 explained in Section 3.1. We will from now refer to PhCs with broken inversion symmetry as VPhCs.

Here we use a HC lattice VPhC whose unit cell contains two cylindrical sublattice rods A and B having the same dielectric constant $\varepsilon = 13$ but different radii. Fig. 4.1 shows the photonic band structures for both TE and TM modes up to 6 bands, obtained using Program 1. In Fig. 4.1 (a), the rod radius of sublattice B, r_B , is set equal to that of sublattice A ($r_A = r_B = 0.23a$), where $a = \Lambda/\sqrt{3}$ is the distance between the two sublattices and Λ is the lattice constant. Here, the first and second bands of the TM mode cross at the K point (no bandgap), and this photonic band structure is exactly the same as the one obtained using the MatLab code developed in our previous P9 report [Ben21] for a HC lattice of cylindrical



(a) When $r_A = r_B = 0.23a$, the structure is the same as the HC lattice of cylindrical rods having the same radius $r = 0.23a$.

(b) When $r_A = 0.23a$ and $r_B = 0$, the structure is the same as the triangular lattice of cylindrical rods having the same radius $r = 0.23a$.

Figure 4.1: Photonic band structures obtained using Program 1. The radius of sublattice rod B (r_B) is equal to that of A or 0. Blue curves: TM mode, Red curves: TE mode

rods having the same radius¹.

Fig. 4.1 (b) shows the case where $r_B = 0$, which is equivalent to a triangular lattice of cylindrical rods, where the distance between two rods is equal to Λ . Here, the rod radius of sublattice A is set to $r_A = 0.23a$.² It is seen that there is a large bandgap opening between the first and second bands. Due to our results matching with previous studies, it is assumed from here on that Program 1 gives the correct band structures.

Fig. 4.2 illustrates the development of the bandgap between the first and second TM bands when the radius of sublattice B is decreased relative to that of sublattice A. As the diameter of the sublattice B rods is decreased (the degree of inversion asymmetry becomes higher), the PBG becomes wider.

This result shows that the inversion symmetry of the original HC lattice with cylindrical rods is broken by differentiating the two sublattices, for instance by changing the radius as in our example, which leads to lifting of the degeneracy at the valley points and a PBG is formed. Furthermore, the PBG becomes wider as the degree of differentiation is made greater. Note that if we have air holes instead of dielectric rods, a PBG is formed in the TE mode, instead of the TM mode.

¹Note that the result obtained in [Ben21] was furthermore found to match with [DG14] to a high degree.

²In fact, this photonic band structure is the same as the one obtained by the MatLab program we developed in [Ben21] for a triangular array of cylindrical rods.

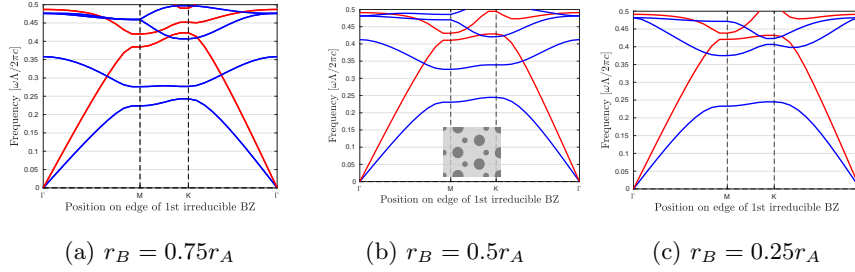


Figure 4.2: Photonic band structures obtained using Program 1. The radius of sublattice rod B (r_B) is changed from $r_B = 0.75r_A$ (a) over $r_B = 0.5r_A$ (b) to $r_B = 0.25r_A$ (c), where $r_A = 0.23a$. Blue curves: TM mode, Red curves: TE mode

4.2 Numerical Calculation of the Valley Chern Numbers

In principle, the Chern number gives a straightforward means of checking whether a given system has TPEMs. Therefore, this section explains how to calculate Berry curvature and valley Chern number for VPhCs having HC lattice structures, where the unit cell consists of two dielectric cylindrical rods with different radii, called sublattices, embedded in an air background. Here, we assume for simplicity that the sublattice A rod radius r_A is larger than the sublattice B rod radius r_B , and that r_B is determined as a ratio of r_A .

Two topologically distinct VPhCs can be formed, depending on which position in the unit cell sublattice A takes, i.e., right or left in the rhombus. We refer to the former VPhC A and the latter VPhC B. Note that the VPhC is a topologically trivial HC PhC when $r_B = r_A$ and is a topologically trivial triangular lattice PhC when $r_B = 0r_A$; see [YYY⁺20] and [CZCD17] for an investigation of such structures. Furthermore, the discussion on the Chern number calculation method in this section is primarily based on [BDZ⁺20] and [dPDG⁺20].

4.2.1 Valley Chern Numbers

As explained in Section 2.2.2, in case of valley-PTIs (unlike Chern PTIs and Spin PTIs), only half of the 1BZ corresponding to each of the valley points in each VPhC shall be integrated to obtain the topological index C_K (or $C_{K'}$) in order to calculate the so-called valley Chern number $C_v = C_K - C_{K'}$ (the definitions here are according to [CZCD17], [YHO21], and [ZXC⁺20]).

First, consider VPhC B and the lowest bulk band in Fig. 4.2. In this case, the peak at the K point results in a Berry phase accumulation of π , while there is a Berry phase accumulation of $-\pi$ at K' (not shown in the figure)³. Integrating over half of the 1BZ, we get the topological indices of

³The valley Chern number is limited to ± 1 when just one pair of Dirac points is

$C_{v,1}^K = +\frac{1}{2}$ for K and $C_{v,1}^{K'} = -\frac{1}{2}$ for K' due to (2.7), i.e.,

$$C_{v,n} = \frac{1}{2\pi} \int_{\text{BZ}} d^2k \Omega_n(k_x, k_y), \quad (4.1)$$

where $C_{v,n}^i, n \in \{1, 2\}, i \in \{K, K'\}$ means topological index (for valley Chern number C_v) of band n for valley point i . The topological indices are either positive or negative half-integers regardless of the radii. In case of VPhC A, the signs of the topological indices are flipped: we will get the topological indices $C_{v,2}^K = -\frac{1}{2}$ and $C_{v,2}^{K'} = +\frac{1}{2}$.

Next, consider the second bulk band of VPhC B. The signs of the topological indices for the valley points are flipped compared to the first bulk band: $C_{v,2}^K = -\frac{1}{2}$ and $C_{v,2}^{K'} = +\frac{1}{2}$. Again, the signs are flipped for the VPhC with different orientation. Thus for VPhC A, the indices are $C_{v,1}^K = +\frac{1}{2}$ and $C_{v,1}^{K'} = -\frac{1}{2}$.

Since each of the inversion asymmetric VPhCs thus achieves a nonzero half-integer topological invariant, we get integer valley Chern numbers. That is, for VPhC B, $C_{v,1} = C_{v,1}^K - C_{v,1}^{K'} = \frac{1}{2} - (-\frac{1}{2}) = 1$ and, similarly for VPhC A, $C_{v,1} = -\frac{1}{2} - \frac{1}{2} = -1$. This is also the reason why valley-polarized topological kink states exist within the bandgap at a domain wall between two VPhCs with opposite unit cell orientation.

Now consider the difference of topological indices above and below the bandgap. For VPhC B, at the K valley point, $C_v^K = C_{v,2}^K - C_{v,1}^K = -\frac{1}{2} - (\frac{1}{2}) = -1$. Similarly, at the K' valley point, $C_v^{K'} = C_{v,2}^{K'} - C_{v,1}^{K'} = \frac{1}{2} + \frac{1}{2} = 1$. According to the bulk-edge correspondence, the number of kink states at each valley is thus 1. The differing signs here indicate the signs of the group velocity of the forward and backward propagating modes at the two valleys [BDZ⁺20], [CZCD17].

In our case, however, since the VPhCs open a large TM gap, as shown in Fig. 4.2, the Berry curvature for both valleys will overlap with each other. As a consequence, the valley Chern number is not a well-defined integer, but rather $0 < |C_{v,n}^K| < 1, 0 < |C_{v,n}^{K'}| < 1$. As the radius contrast between two sublattices becomes larger, the topological indices become smaller. For example, using a similar VPhC structure, [YHO21] shows that the plot of topological indices as a function of r_B forms a parabola-like curve, whose values range from 0 to ± 0.5 , but the Chern number of the standard definition, i.e., $C_v = C_K + C_{K'}$, is zero. Note that the edge dispersion will not cross from the lower band to the upper band in a gap-free manner. Regardless of this side effect, the difference in the sign of valley Chern number should ensure the protection of the topological valley phase, as long as the bulk state at the K valley is orthogonal to the K' valley. [HLY⁺19]

gapped. In case of larger valley Chern numbers, one may find multiple pairs of Dirac points along a mirror-symmetric reciprocal axis, and then lift the degenerate points by lowering the point-group symmetry [CZCD17].

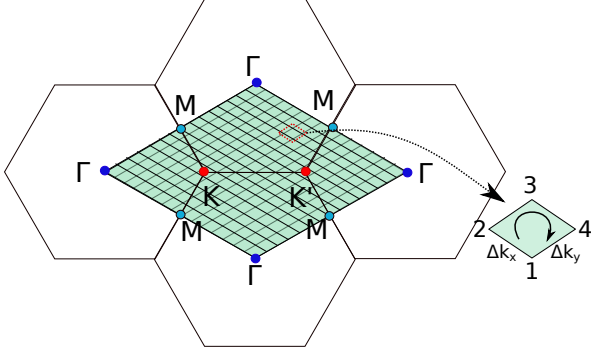


Figure 4.3: Discretization of the 1BZ in increments of Δk_x and Δk_y for the case of the HC lattice, called plaquettes. The position of the corresponding high symmetry points are indicated with colored points. The inset shows a zoom-in of the plaquette over which the Berry curvature is evaluated. [dPDG⁺20]

4.2.2 Calculation of Berry Curvatures

In this section, we show how we can calculate topological indices numerically. We limit our discussion to TM mode for simplicity. That is,

$$\mathbf{E}_{\mathbf{k}}(\mathbf{r}) = \hat{\mathbf{z}}E_{\mathbf{k}}(\mathbf{r}).$$

The solutions for the electric field are scalar functions for the 2D case, which makes calculation simpler. We can define the associated Bloch functions as

$$E_{\mathbf{k}}(\mathbf{r}) = v_{\mathbf{k}}(\mathbf{r})e^{i\mathbf{k}\cdot\mathbf{r}},$$

where $v_{\mathbf{k}}(\mathbf{r})$ is the periodic part of the electric field solutions.

In calculations of the topological indices and valley Chern number for HC lattice structures, we first need to discretize the continuous 2D 1BZ into a grid, as shown in Fig. 4.3. For the n^{th} band, the Chern number is given by

$$C_n = \frac{1}{2\pi} \sum_{k_x, k_y} \Omega_n(k_x, k_y) \Delta k_x \Delta k_y. \quad (4.2)$$

where Δk_x and Δk_y are side lengths of each plaquette (equal to $|\mathbf{b}_i|/N$, where $i = 1, 2$, $N \times N$ is the number of divisions of the unit cell, and \mathbf{b}_i are the basis vectors of 1BZ). We number the four vertices of each plaquette 1, 2, 3, and 4 in a clockwise direction, as shown in Fig. 4.3. For isolated bands (i.e., the 1st and 2nd bands are separated by a bandgap, and there are no degeneracies, as in case of inversion asymmetric VPhCs), the integral of the Berry curvature over the plaquette can then be written as follows (the reasoning for this can be found in [BDZ⁺20], [dPDG⁺20], and [FHS05]):

$$\Omega_n(k_x, k_y) \Delta k_x \Delta k_y = \Im[-\ln(\langle v_{\mathbf{k},n,1} | v_{\mathbf{k},n,2} \rangle \langle v_{\mathbf{k},n,2} | v_{\mathbf{k},n,3} \rangle \langle v_{\mathbf{k},n,3} | v_{\mathbf{k},n,4} \rangle \langle v_{\mathbf{k},n,4} | v_{\mathbf{k},n,1} \rangle)], \quad (4.3)$$

where

$$\langle v_{\mathbf{k},n,p} | v_{\mathbf{k},n,q} \rangle = \sum_{w,m} v_{\mathbf{k},n,p}(w,m)^* \varepsilon(w,m) v_{\mathbf{k},n,q}(w,m) \Delta s \quad (4.4)$$

where $p, q \in \{1, 2, 3, 4\}$ denotes the four vertices, (w, m) indicates the $(w, m)^{th}$ discretized cell in the real space, and Δs is the area of the discretized lattice in the real space. Thus $v_{\mathbf{k},n,p}(w, m)$ is the periodic part of the electric field in real space corresponding to each corner of each plaquette. Eq. (4.3) shows that the integral of the Berry curvature over each plaquette in the BZ can be obtained by taking the inner products of the eigen electric fields at adjacent vertices in a clockwise order. Note that the electric field solutions are normalized, i.e., $\langle v_{\mathbf{k}}(\mathbf{r}) | v_{\mathbf{k}}(\mathbf{r}) \rangle \equiv 1$. Moreover, any arbitrary phase coming from this procedure cancels out because each state appears twice, once as a $\langle \text{bra} |$ and once as a $| \text{ket} \rangle$.

Substituting (4.3) into the summation in (4.2), we get a discrete approximation to the Chern number. It can be shown that this approximation converges to the (continuous variable) Chern number in the limit $\Delta k_x(y) \rightarrow 0$ [FHS05]. Fortunately, it also converges rapidly; often, as coarse a grid as 24×24 cells is enough for accurate determination of the Chern number. The integration is carried out over the two equilateral triangles obtained by cutting the unit cell shown in Fig. 4.3 vertically into two along a line segment $\Gamma - \Gamma$, yielding separate valley Chern numbers for the K and K' points, respectively.

In the case considered, there is one band each above and below the bandgap (the first and second bands), and for each band, we want to calculate the topological index for each of the two valley points. For numerical calculation using MatLab, we will need the following input data:

- Real space grid $\{x_w, y_m\}$ and reciprocal space grid $\{k_{x_w}, k_{y_m}\}$
- Distribution of electric field (eigenfunction) in the real space, corresponding to each point of the reciprocal space grid $\mathbf{E}(\mathbf{r}) = E(x_w, y_m)$
- Dielectric constant value at each point of the real space grid $\varepsilon(\mathbf{r})$.

The output shall be a matrix containing all values of the Berry curvature and topological indices for both the valley points. The following sections explain how to obtain the input data above.

4.2.3 Calculation of Electric Field Distribution

We numerically calculate the distribution of electric field within a unit cell using Program 2. Fig. 4.4 shows the geometries of unit cells of HC lattices that serve as dielectric constant maps, as well as photonic band structures for TM mode when the two rods in the unit cell have the same radius of $r_A = r_B = 0.23a$ ((a) and (b)) as well as when $r_A = 0.23a$ and $r_B = 0.5r_A$ ((c) and (d)), respectively. The resulting photonic band structures match with those in Fig. 4.1 and 4.2 obtained using Program 1 to a high degree for other r_B radii as well.

Program 2 first calculates the in-plane magnetic field. Using the calculated magnetic field, it then calculates the electric field. The calculated

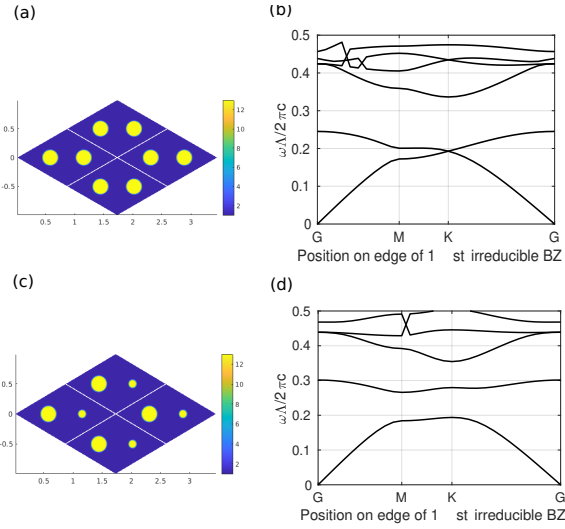


Figure 4.4: Dielectric constant map and photonic band structures of a HC lattice, obtained using Program 2: (a) and (b) for $r_A = r_B = 0.23a$, (c) and (d): for $r_A = 0.23a$ and $r_B = 0.5r_A$. Four unit cells are put together to show the HC lattice structure. The structures are the same as the those obtained using Program 1.

electric field does not include the phase factor $e^{i\mathbf{k}\cdot\mathbf{r}}$ at each reciprocal grid point. This means that the code yields the periodic part $v_{\mathbf{k}}(\mathbf{r})$, which we can use for the calculation of Berry curvature as is.

4.2.4 Reciprocal Space Grid

We formed the reciprocal space grid by dividing each reciprocal lattice vector length into $N = 2^5$ equal intervals. Fig. 4.5 shows the grid numbering scheme used. The grid points whose coordinates (k_x, k_y) run along \mathbf{b}_1 (upper left edge) start from $(0, 0)$ and end at $(0, \frac{2\pi}{\Lambda})$ are numbered 1 to $N - 1$. The grid point N starts from the second row at $(\frac{2\pi}{N\Lambda}, 0)$ and so on.

The topological index for the K valley point is calculated using the upper half of the rhombus, while that for the K' valley point is calculated using the lower half of the rhombus. Those two areas are divided by the line $k_x = k_y$. Each equilateral triangle is divided into rhombus areas and triangular areas, for which we calculate the Berry curvature using (4.3). The grid point numbering scheme is furthermore used to determine the values of p, q for each plaquette.

4.2.5 Calculated Topological Indices

Fig. 4.6 presents the result of calculating topological indices $C_{v,1}^K$ and $C_{v,1}^{K'}$ for the first band of the TM mode, for VPhC A ($r_A > r_B$). The grid size is 24×24 . Our plot is almost the same as the corresponding plot in [YHO21]. It should be noted, however, that in the study by [YHO21], hollow rods in

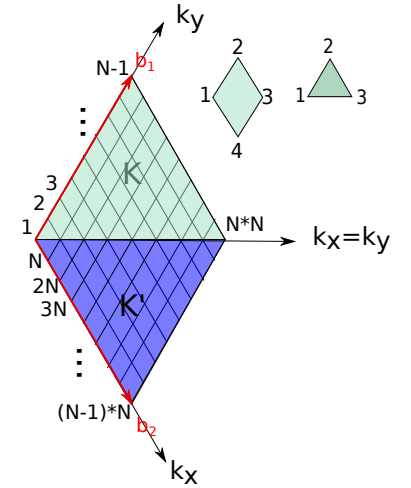


Figure 4.5: Grid points numbering scheme for reciprocal space grid. Insets show the order of taking inner products for the case of rhombus and triangular plaquettes.

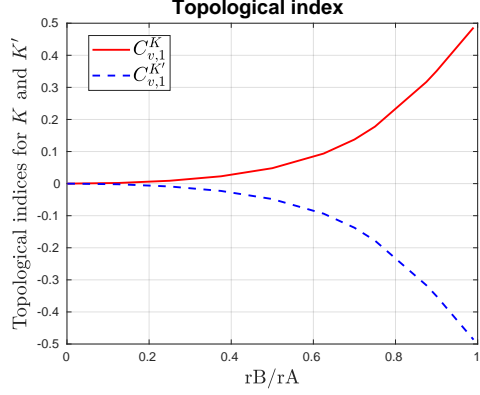


Figure 4.6: Topological indices $C_{v,1}^K$ and $C_{v,1}^{K'}$ for the first band of the TM mode. The rod radius of sublattice A r_A is fixed while the rod radius of sublattice B is changed as a function of $r_A = 0.23\Lambda$.

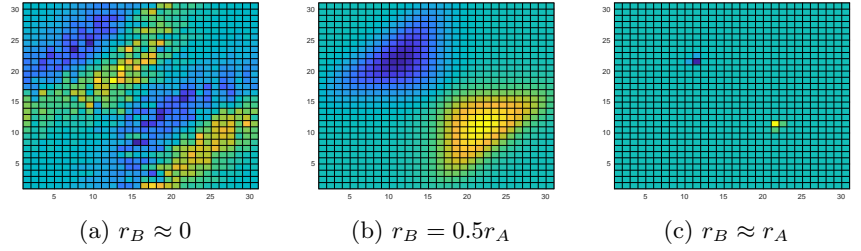


Figure 4.7: Distribution of berry curvature, $r_A = 0.23\Lambda$

silicon background and TE band were used, which may be the reason for any differences. The topological indices for the K and K' have the same values with opposite signs, as should be, and as the sublattice radius r_B is decreased from $r_B = r_A$ to $r_B \approx 0$, $C_{v,1}^K$ decreases from 1 to 0 while $C_{v,1}^{K'}$ increases from -1 to 0. The signs of the topological indices are flipped for the second band (values not shown). These results indicate that our code for calculating valley Chern numbers is correct. Note that we only calculate the topological indices until $r_B = 0.99r_A$, because the case $r_B = r_A$ represents a degeneracy (no bandgap) and requires a different calculation method.

Fig. 4.7 shows some example distributions of Berry curvature for VPhC A. Here, the rhombus-shaped HC reciprocal space shown in Fig. 4.5 is represented as a rectangle. It is seen that the peak/sink of Berry curvature is sharply localized around K/K' valley for $r_A \approx r_B$ (HC lattice structure), but spread out around the valley as the geometry approaches a triangular lattice.

Next, we fixed the radius of sublattice B rod to be $r_B = 0.23\Lambda$ and changed the radius of sublattice A (VPhC B). As expected, we obtained the same topological index values, but with opposite signs compared to the case of VPhC A, where the rod radius of sublattice A is fixed and the rod radius

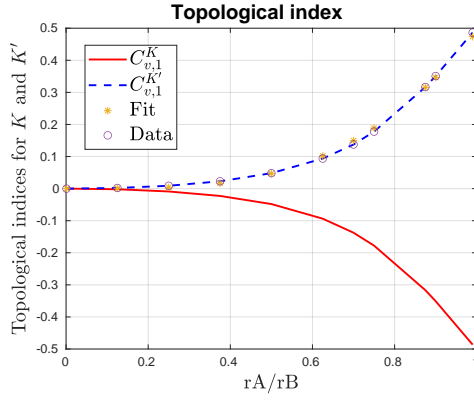


Figure 4.8: Topological indices $C_{v,1}^K$ and $C_{v,1}^{K'}$ for the first band of the TM mode. The rod radius of sublattice B r_B is fixed while the rod radius of sublattice A is changed as a function of $r_B = 0.23\Lambda$.

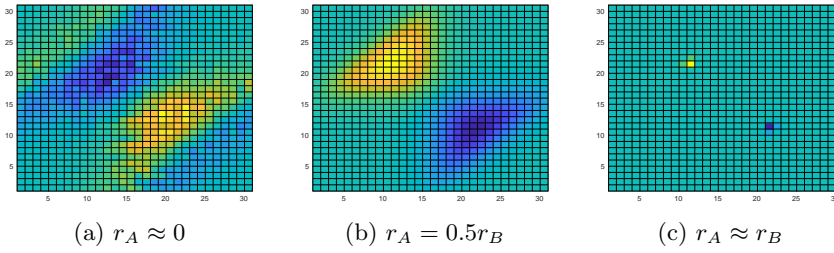


Figure 4.10: Distribution of berry curvature, $r_B = 0.23\Lambda$

of sublattice B is changed. This means that the topological indices for band 2 for VPhC A are identical to the topological indices for band 1 for VPhC B. Figs. 4.8 and 4.10 show the results. Our program produced exactly the same values for the same radius combinations, with different signs depending on the band and rod orientation, as expected. Fig. 4.8 also shows a 3rd order polynomial fit to the result of $C_{v,1}^{K'}$, exhibiting very good agreement with the function $f(r_A/r_B) = 0.6426(r_A/r_B)^3 - 0.1724(r_A/r_B)^2 + 0.01951(r_A/r_B)$.

Fig. 4.10 shows the gradually increasing concentration of Berry curvature around the K and K' valley points as r_A approaches r_B , whose distribution is opposite to Fig. 4.7.

4.3 Valley Photonic Topological Insulators Studied in This Project

4.3.1 Valley Photonic Crystals

In the rest of the project, we investigate an all-dielectric VPhC studied in [CZCD17]. We form two VPhCs called VPhC A and VPhC B, both of which have a HC lattice structure whose unit cell consists of two silicon rods

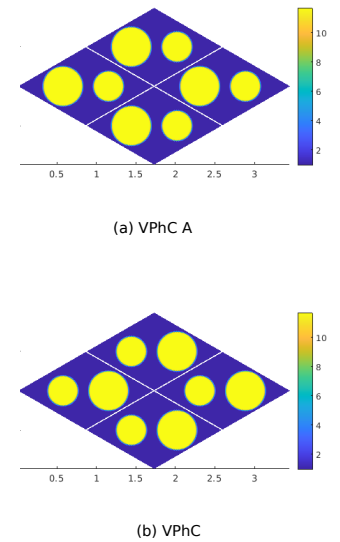


Figure 4.9: ϵ map of four unit cells of the HC VPhCs used in [CZCD17] generated using Program 2 showing a HC structure for VPhCs A and B. Bigger rods have $r = 0.25\Lambda$, smaller rods have $r = 0.19\Lambda$.

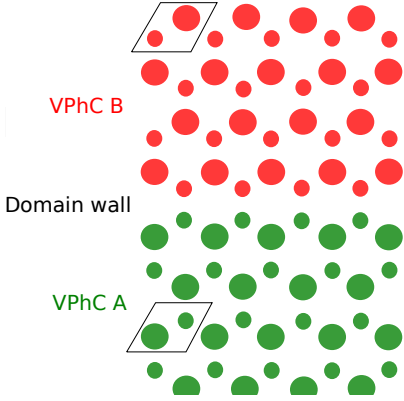


Figure 4.11: Schematic drawing of a valley-P TI with a domain wall having zigzag-edge boundary [CZCD17]

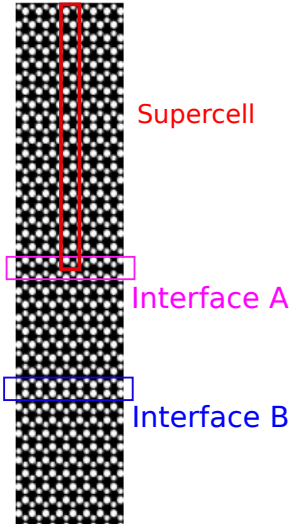


Figure 4.13: (a) Geometry of the PTI where the supercell (10 unit cells of VPhC B are placed on top of 10 unit cells of VPhC A) indicated with red line is repeated 8 times in the x -direction and 2 times in the y -direction. Two types of boundaries, interfaces A and B, are formed: small rods meet at the boundary for interface A, while big rods meet at the boundary for interface B.

embedded in an air background as shown in Fig. 4.9, which are generated using Program 2. The bigger rod has a radius of $r_A = 0.25\Lambda$ while the smaller rod has a radius of $r_B = 0.19\Lambda$. The dielectric constant of each silicon rod is $\varepsilon = 11.7$. The inversion symmetry is broken in opposite ways in the two VPhCs; before the inversion symmetry breaking, the rod radius is $r = 0.22\Lambda$, and with the detuning of $\delta r = \frac{r_A - r_B}{2} = 0.3\Lambda$, the right rod in a unit cell is bigger than the left rod for VPhC A while the left rod is bigger than the right rod for VPhC B. Thus, the K and K' valley points of the two VPhCs will have topological indices of opposite sign.

Due to the inversion asymmetry, there is a bandgap at frequencies between $0.244\Lambda/\lambda$ and $0.272\Lambda/\lambda$ at the $K(K')$ points, between the two lowest bulk bands of TM mode for both VPhCs. We confirmed the existence of the bandgap as well as the frequency range using Program 1, as shown in Fig. 4.12. The same result is obtained with Program 2 as well.

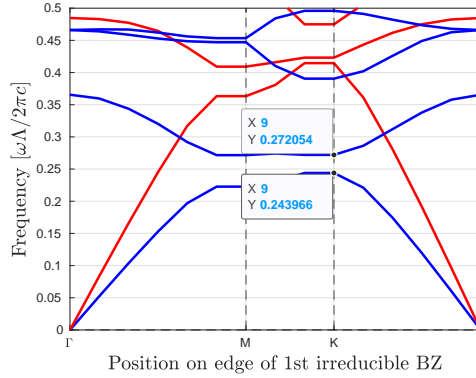


Figure 4.12: The photonic band structure of the VPhC shown in Fig. 4.9. Notice that the bandgap width between the first and second bands obtained matches with the result reported by [CZCD17].

In this valley-P TI, various types of domain walls can be formed, such as zigzag-edge, armchair-edge, and bearded-stack, and each of them can have two types: either small or big rods meet each other at the boundary (See Fig. 1.4). We first study the zigzag-edge boundary where small rods meet each other at the domain wall, shown in Fig. 4.11.

4.3.2 Valley-dependent Kink States

We use Program 2 in order to examine the photonic band structure of the valley-P TI and the distribution of electric field magnitude. We create a long rectangular supercell sized $\Lambda_x = \sqrt{3}a$ and $\Lambda_y = \frac{3a}{2} \cdot 20$ (1D discrete translational symmetry in the x -direction) where the upper half is VPhC B and lower half is VPhC A. By repeating this supercell 8 times in the x -direction and 2 times in the y -direction, two types of zigzag boundaries, interfaces A and B, are formed as shown in Fig. 4.13: small rods meet at the boundary for interface A, while big rods meet at the boundary for interface B.

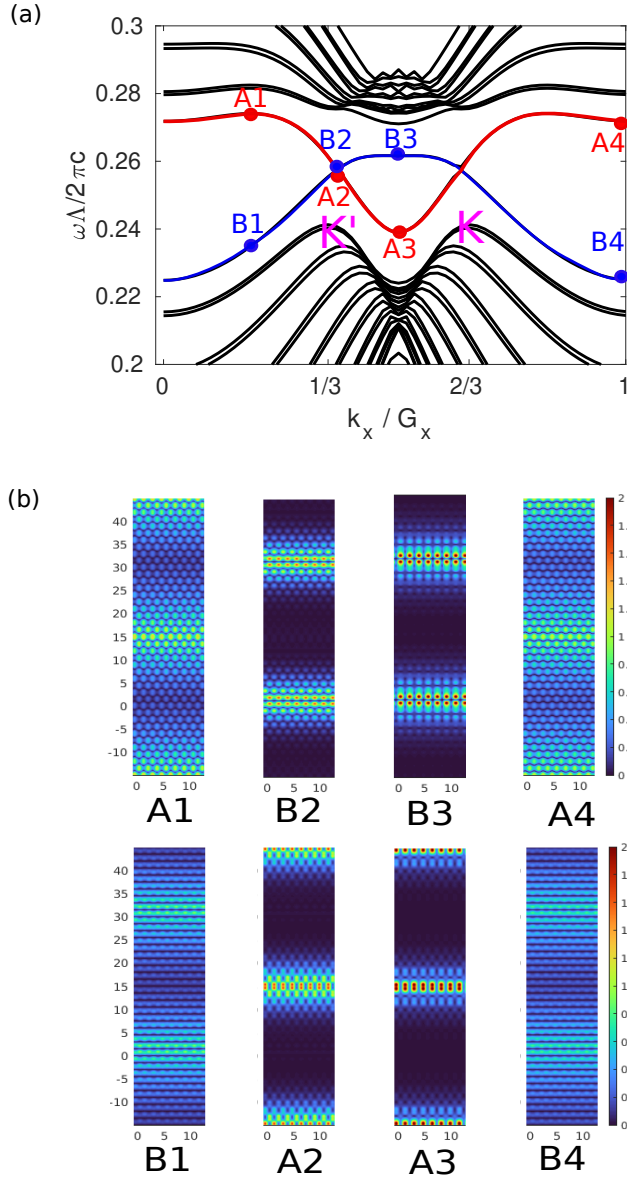


Figure 4.14: (a) Band diagram for the geometry in Fig. 4.13, showing the two types of valley-dependent kink states. The kink states of interface A (red curve) consist of one with negative velocity at the K' valley and the other with positive velocity at the K valley, whereas the kink states of interface B (blue curve) consist of one with positive velocity at the K' valley and the other with negative velocity at the K valley. (b) The distribution of electric field magnitude for the two bands located in the bandgap, for the points marked in (a).

Fig. 4.14 (a) shows the photonic band diagram thus obtained. In the bulk bandgap between normalized frequencies $0.244 \Lambda/\lambda$ and $0.272 \Lambda/\lambda$, we see robust edge states at interfaces A and B. The kink states for interface B have the opposite group velocities $\frac{d\omega}{dk_x}$ at the K and K' valleys, which agrees well with [CZCD17]. In this case, the topological index differences at the K and K' valleys are -1 and $+1$. The kink states for interface A have the opposite group velocities due to the opposite signs of topological indices.

Fig. 4.14 (b) shows the distributions of electric field magnitudes corresponding to the points marked in Fig. 4.14. It is seen that the waveguiding effect and light confinement are the strongest between the K and K' valley points; the effect is weaker otherwise. The broadness of the waveguiding effect in terms of frequency depends on the type of interface: interface A has robust transport in a broader band. It is also noted that the group velocity is nearly zero at points A3 and B3; the wave oscillates up and down without propagating in neither direction. On the other hand, at the valley points (A2 and B2) the magnitude of group velocity is the greatest.

4.3.3 Valley-Photonic Topological Insulators and Coupling

Valley-PTIs are different from other types of PTIs in the sense that the TPEMs are formed at the domain wall between two domains (in case of Chern and Spin PTIs, TPEMs are formed at interfaces between topologically trivial and non-trivial systems). For this reason, it is not possible to form directional coupling between two identical domain walls. Interface A is formed when VPhC B is placed above VPhC A while interface B is formed when VPhC A is placed above VPhC B; there is no way to form two interfaces A next to the other, for any types of boundaries. This implies that coupling normally occurring between the same type of waveguides placed close to each other may not occur in case of valley PTIs⁴. We demonstrate this by comparing with conventional PhC waveguides.

Fig. 4.15 illustrates that when two identical waveguides (line defects of triangular-lattice PhC) are formed in parallel at a close distance as shown in (a), the photonic band structure has two defect modes shown in (b) (19th and 20th bands shown in red and blue colors), and waves in the two waveguides are coupled to form odd and even waves as illustrated in (c) and (d), which show imaginary and real parts of electric field. The figures are generated using Program 2.

When two different types of interfaces are placed at a close distance, coupling phenomena like the one shown in Fig. 4.15 is not observed. Fig. 4.16 shows the schematic drawing for testing coupling between interfaces A and B. Fig. 4.17 shows the photonic band diagram (Fig. 4.17 (c)) and the distribution of electric field magnitude at the mid point between the two

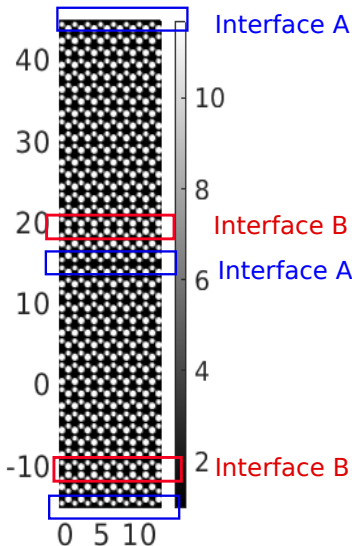


Figure 4.16: Geometry of the valley-PTI having two domain walls close to each other

⁴An example photonic circuitry element utilizing this principle is a directional coupler. This consists of two waveguides that come close to each other so that the fields can couple in a section of certain length. In the coupling section, the two aligned single-mode waveguides form a dual-mode guide that supports an even and an odd propagating guided mode (with different wavevectors) with respect to a certain symmetry of the system. [Gap10]

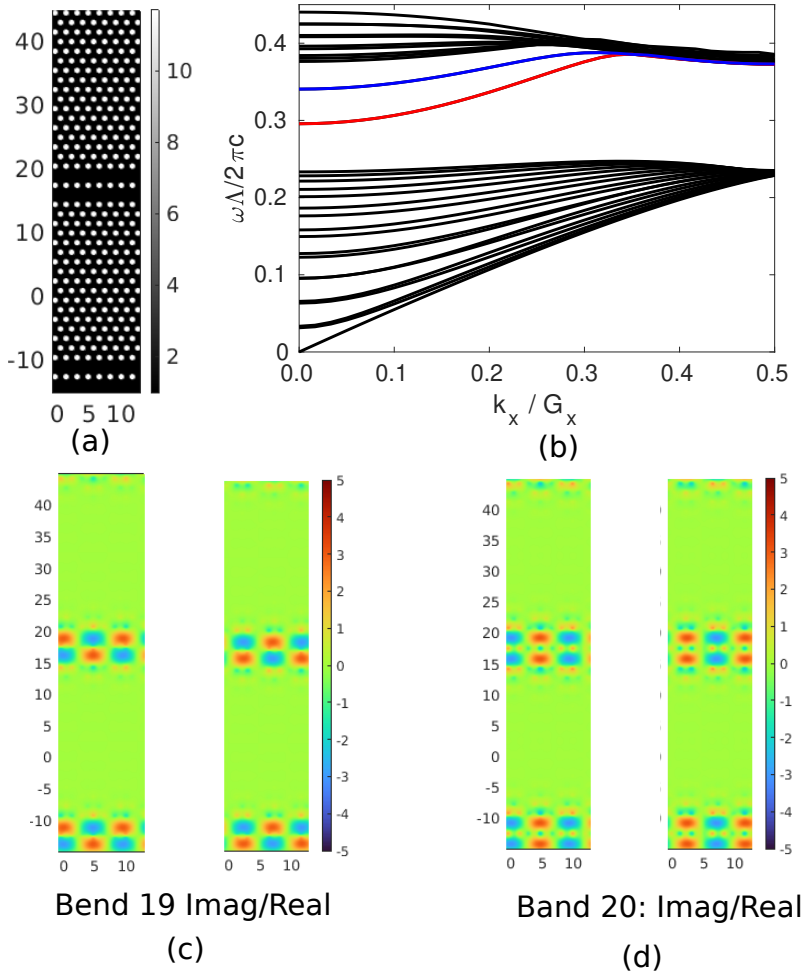


Figure 4.15: Directional coupling of two waveguides of triangular-lattice PhC. (a) Geometry of the PhC containing two parallel waveguides in close distance. (b) photonic band structure, (c),(d) distribution of imaginary (left) and real (right) parts of electric field of the 19th and 20th bands (marked with red and blue colors in (a)), respectively

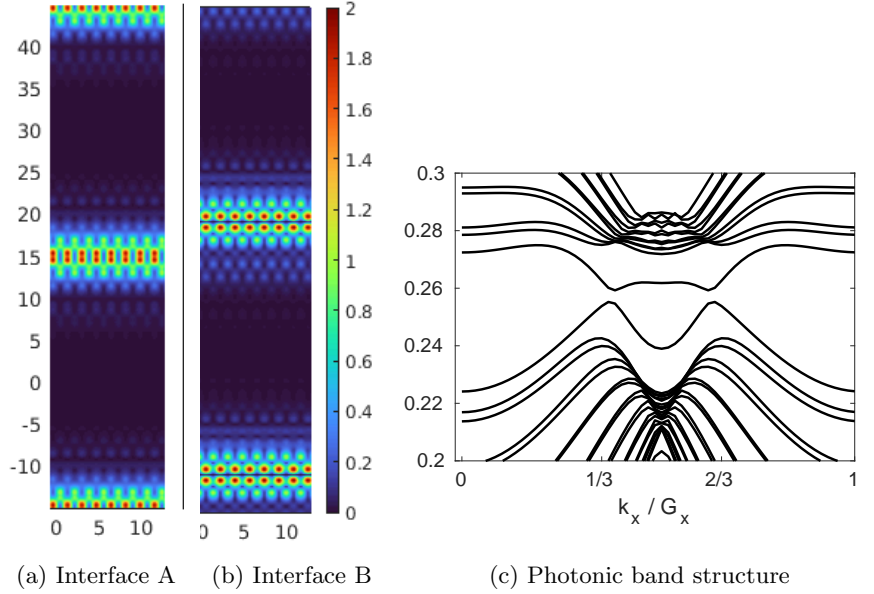


Figure 4.17: Photonic band structure and distribution of electric field magnitude at close to the middle point between K and K' , when interfaces A and B of the valley-PTI are placed close to each other

valley points (Figs. 4.17 (a) and 4.17 (b)). We tried to place the two interfaces as close as possible as shown in Fig. 4.18 (a), which depicts interfaces B and A being placed next to each other. As illustrated in Fig. 4.18 (b), the two kink states still do not couple. The distribution of electric field magnitude is more spread compared to the case above, but clearly different. From these results, we conclude that even though the two domain walls are close, the two types of kink states are excited separately; no coupling is observed.

4.4 Summary

In this chapter, we demonstrated the main features of valley-PTIs discussed in Section 2.2 through numerical calculation using Programs 1 and 2. Firstly, we calculated photonic band structures of a HC lattice PhC to show that it has a degeneracy at the K point, and that the degeneracy is lifted when one of the sublattice rods is made smaller. Secondly, we developed a program for calculating the valley Chern number, and used a HC lattice VPhC whose unit cell contains two cylindrical rods having different radii to illustrate that the Berry curvatures are actually concentrated around the two valley points. The two valley points of a VPhC are said to have topological indices of half integers having opposite signs, but in case of the example geometry we used, the K and K' points have the same non-integer indices with opposite signs due to overlapping of Berry curvature as a consequence of the large PBG. Lastly, we formed inversion-symmetry partner VPhCs

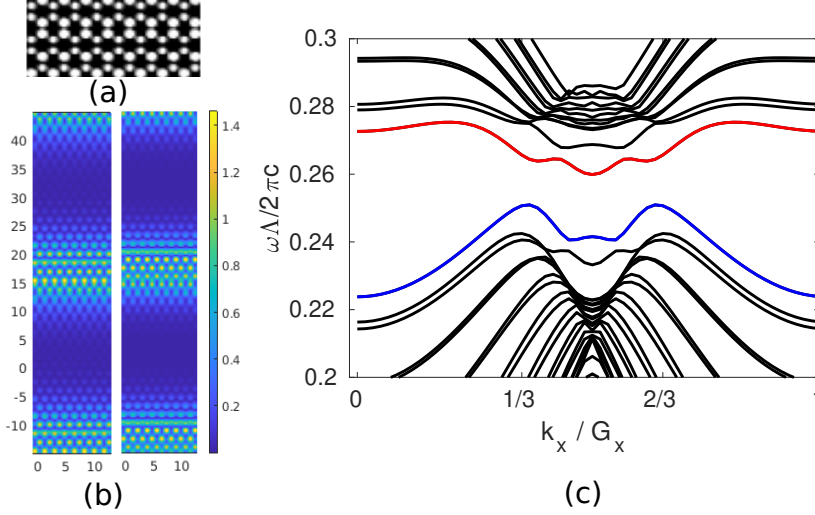


Figure 4.18: (b) Distribution of electric field magnitude of PTI containing two different domain walls next to each other as illustrated in (a) at $k_x / G_x = 22/30$, for 19th (left) and 20th (right) bands (c) Photonic band structure corresponding to geometry (a), bands 19 and 20 are more separated than in Fig. 4.17.

and created two types of zigzag-edge domain walls. We demonstrated that one guided mode for each domain-wall type is formed within the PBG and that the two modes have opposite group velocities at the valley points. We also showed that the thus formed kink states localized at the domain wall do form robust waveguides by illustrating localization of light through the distribution of electric field magnitude.

CHAPTER 5

Waveguide Quality of Valley-PTIs

This chapter first presents results related to the comparison of robustness of light propagation among various types of domain walls formed in the HC lattice valley-PTI and waveguides formed by line defects in the triangular PhC. It then presents results of investigating unidirectionality of domain walls as waveguides: optimum placement of dipole emitters for achieving the highest directionality and the effect of geometry of the PTI. Note that throughout the chapter, the same color scale is used for all color plots of electric field magnitudes, except when the magnitudes are exceptionally strong.

5.1 Formation of Z-shape Bend

In this section, we confirm that valley-polarized topological kink states exist within the bandgap, at the domain wall between the two VPhCs of opposite orientation, by showing the light confinement using Program 3 explained in Section 3.3.

5.1.1 Kink States Localized at a Domain Wall

We form a zigzag-edge domain wall along a Z-shape bend as shown in Fig. 5.1 in such a way that small rods of VPhC A meet small rods of VPhC B at the domain wall. Note that valley-protected broadband robust transport is not achieved along armchair-edge domain walls [OPA⁺19], [CZCD17], which is demonstrated later. Note also that Fig. 5.1 serves as dielectric constant map as well; silicon rods having $\varepsilon = 11.7$ are represented as white circles on a background of air having $\varepsilon = 1$. We define the simulation window to include some surrounding air background as well, so that we can show not only the distribution of electric field magnitude within the valley-PTI, but

also how the light is reflected, scattered, and transmitted in the surrounding area.

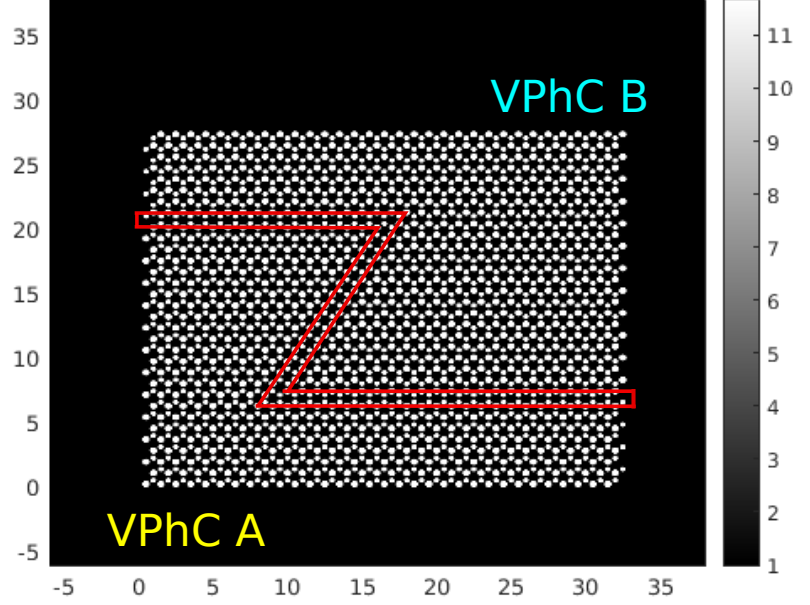


Figure 5.1: Z-shape bend formed using VPhCs A and B. VPhC B occupies the top 1/4 and middle right side, while VPhC A occupies the bottom 1/4 and middle left side of the PTI consisting of 32×32 unit cells. Along the Z-shape bend, small rods of both VPhCs meet, forming the zigzag-edge boundary. The unit of the axes is the lattice constant Λ .

Fig. 5.2 is a plot of electric field magnitude distribution in the valley-PTI at the normalized frequency $0.25\omega\Lambda/2\pi c$ (within the aforementioned bandgap), and demonstrates the existence of kink states; the Gaussian beam incident to the valley-PTI is confined along the domain wall between the two VPhCs; the magnitude of the electric field remains nearly constant throughout the bend and there is little scattering into the bulk. Fig. 5.3 shows the same analysis with the normalized frequency $0.2\omega\Lambda/2\pi c$, which is outside the bandgap. It is seen clearly that the bulk modes allow photon propagation through the bulk, and that the domain wall has no influence on the light propagation.

5.1.2 Various Types of Boundaries

In this section, we compare kink states of various types of domain walls, against interface A of zigzag-edge domain wall shown in Fig. 5.4. It is the same valley-PTI as in Fig. 5.1, but the size is smaller, consisting of 16×16 unit cells (Fig. 5.4 (a) shows only the relevant part enlarged). A Z-shape bend can be recognized as a narrow waveguide formed between small rods.

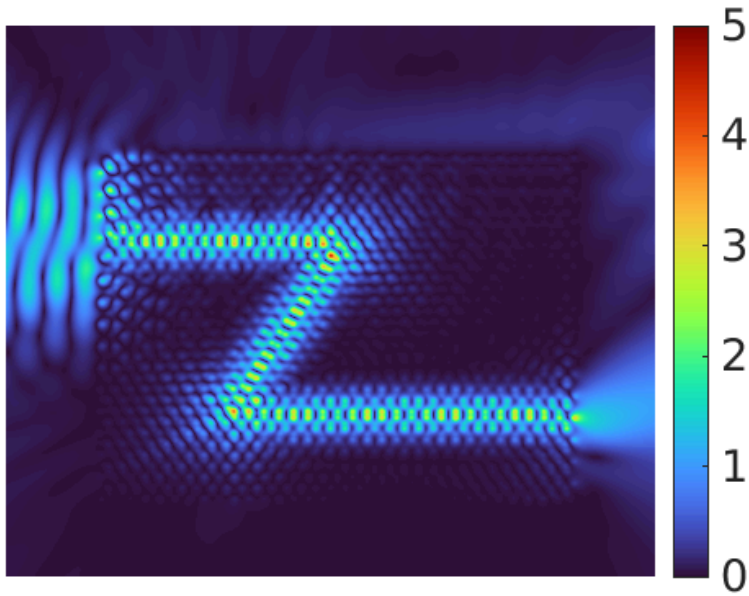


Figure 5.2: Distribution of electric field magnitude for a Gaussian beam (paraxial approximation) incident on a valley-PTI at normalized frequency $0.25 \omega \Lambda / 2\pi c$

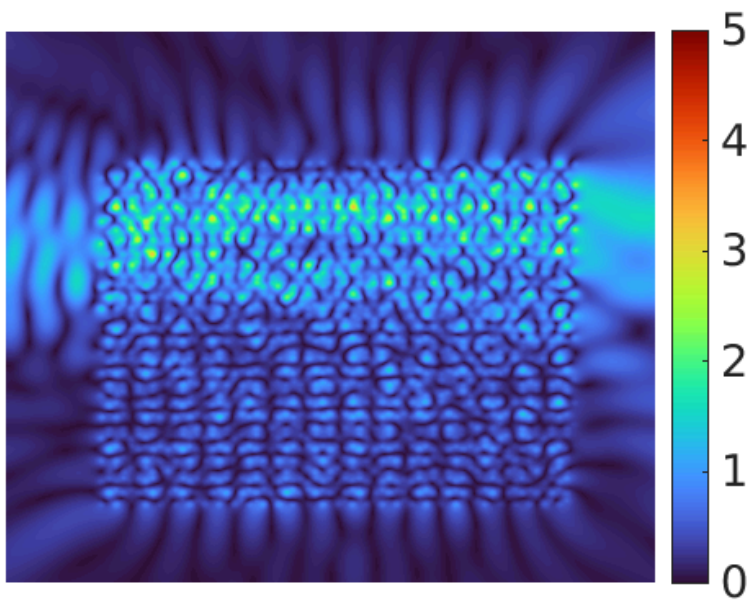


Figure 5.3: Distribution of electric field magnitude for a Gaussian wave incident on a valley-PTI at normalized frequency $0.2 \omega \Lambda / 2\pi c$

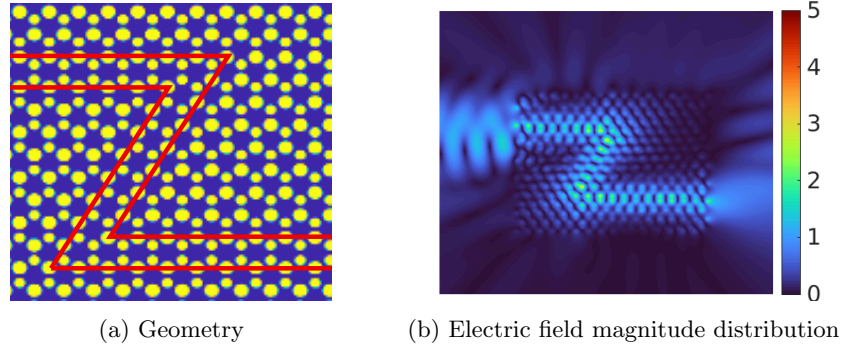


Figure 5.4: A Z-shape bend formed in a valley-PTI consisting of 16×16 unit cells, where small rods of VPhC A meet small rods of VPhC B to form a zigzag-edge domain wall. (a) Geometry, (b) Distribution of electric field magnitude

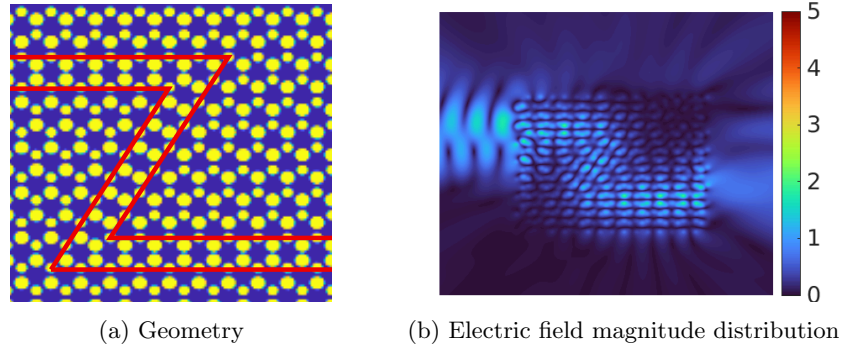


Figure 5.5: A Z-shape bend with interface B, where big rods of VPhC A meet big rods of VPhC B.

Exchanging VPhC Positions

Fig. 5.5 (a) shows a Z-shape bend where the positions of VPhCs A and B are exchanged (interface B). Along the Z-bend, big rods of both VPhCs meet, forming the zigzag-edge domain wall. We can recognize the Z-shape kink state, but the waveguiding is not as robust as in Fig. 5.4, judging from the lower light concentration at the domain wall. We thus conclude that interface A is more robust than interface B.

Narrower or Wider Boundaries

We investigate how the kink state robustness changes if the distance between the two small rods at the domain wall is made wider or narrower. Fig. 5.6 (a) shows the geometry of the boundary where the distance between the two VPhCs is made slightly narrower (0.15λ) and (b) illustrates the distribution of electric field magnitude. Fig. 5.7 shows the same plots with slightly wider (0.15λ) distance between the two VPhCs. Fig. 5.8 shows the result of making the distance between the two VPhCs even wider (0.45λ).

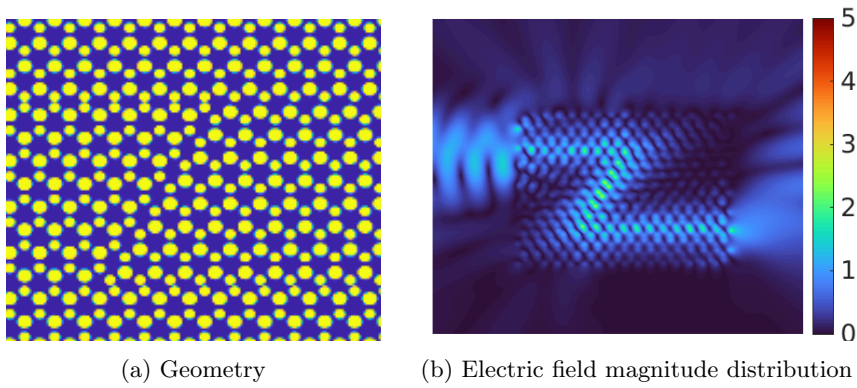


Figure 5.6: The same Z-shape bend as Fig. 5.4, except that the distance between the small rods belonging to VPhC A and VPhC B is made smaller.

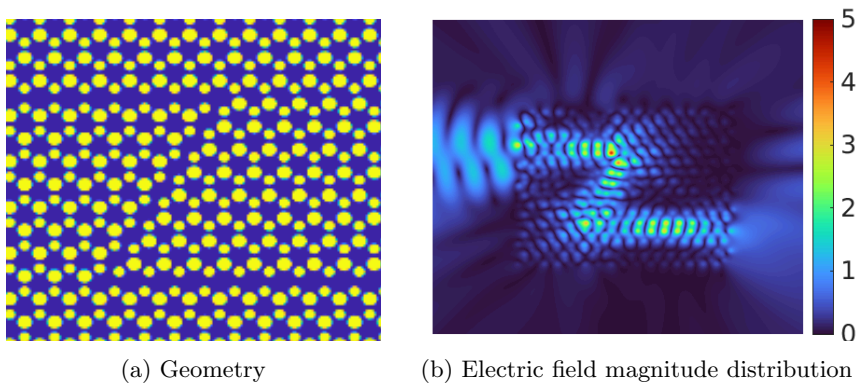


Figure 5.7: The same Z-shape bend as Fig. 5.4, except that the distance between the small rods belonging to VPhC A and VPhC B is made wider.

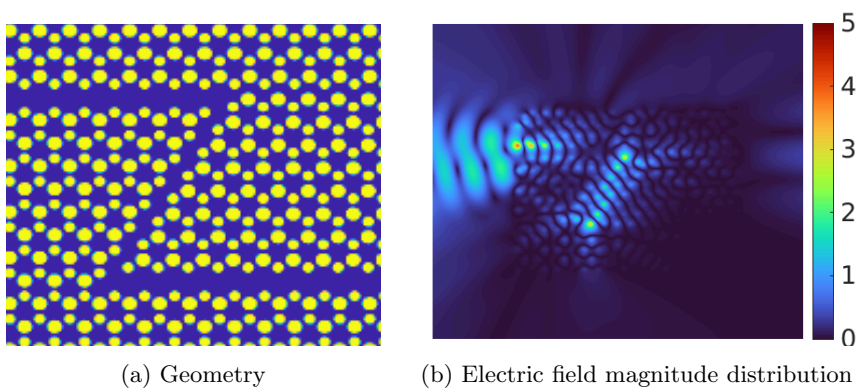


Figure 5.8: The same Z-shape bend as Fig. 5.4, except that the distance between the small rods belonging to VPhC A and VPhC B is made even wider.

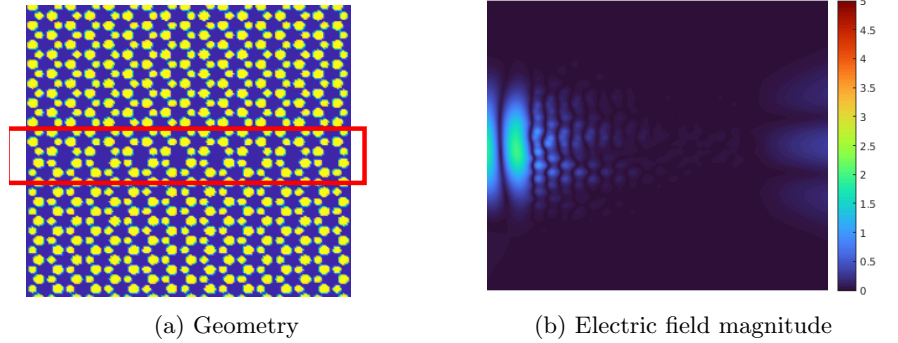


Figure 5.9: Armchair-edge boundary formed between VPhCs A and B (16×16 unit cells), where two valleys (small and large rods) mix.

Comparing the magnitude of electric field and scattering into the bulk among the three cases, we may conclude that the effect of narrowing the domain wall is small at best, and that the kink state is lost if the width of the domain wall is too large. The reason for this is that if the distance between the two VPhCs becomes too large in the zigzag-edge domain wall, the Berry curvatures associated with both valleys overlap. The valley Chern numbers are not well defined anymore, and a gap opens in the edge state bands [OPA⁺19].

Armchair-edge Domain Walls

There are two typical types of interfaces between two VPhCs having opposite orientations: zigzag- and armchair-edge domain walls. Since the K and K' valleys of the two lattices have opposite valley Chern numbers, the gap needs to close locally at the points at the interface between the two lattices in order for the light to propagate along the interface. This situation is restricted to very specific conditions.

For zigzag-edge domain walls, the propagation of a wave packet in an interface state with a given valley polarization is protected against any perturbation that does not mix the two valleys, for instance, bends of the interface of 120° , which preserve the zigzag character of the interface. For armchair-edge domain walls, on the other hand, the breaking of translational symmetry in the direction perpendicular to the interface mixes the K and K' valleys of each lattice, and the valley Chern number is not well defined. [OPA⁺19]

Here, we numerically demonstrate that no kink states are formed at the armchair-edge domain wall between VPhCs A and B. Fig. 5.9 (a) shows the geometry of an armchair-edge domain wall between the two VPhCs, where the two valleys mix at the interface. The distribution of electric field magnitude in Fig. 5.9 (b) illustrates that there is no penetration of light at a normalized frequency of $0.25 \omega \Lambda / 2\pi c$, which is well within the bandgap.

5.2 Comparison between Kink States and Waveguides

In this section, we first show the result of testing the first hypothesis. For this purpose, we compare robustness of the kink states formed at interface A between two VPhCs A and B having opposite geometrical orientation introduced in Section 5.1, against a waveguide formed by line defects in a triangular lattice PhC having the same dielectric material as the valley-PTI. This is done by comparing the transmission of light between the Z-shape bend and straight-line domain walls/waveguides; if the difference in their transmission is small, it can be concluded that the effect of sharp bends of the Z-shape domain wall is negligible, meaning that the light propagation is immune to backscattering.

We then show the result of testing the second hypothesis. We compare robustness of kink states among different types of valley-PTI domain walls. We already showed in Section 5.1.2 that the armchair-edge domain wall does not provide waveguiding, and interface A of a zigzag-edge domain wall is better than interface B. We thus only compare transmission of zigzag-edge interface A and bearded-stack domain wall.

5.2.1 Propagation of Light in a Z-shape Bend Waveguide of a Photonic Crystal

We first examine the robustness of a waveguide formed by line defects in a PhC. Here we use a PhC consisting of a triangular array of 16×16 Si ($\epsilon = 11.7$) rods of radius $r = 0.25\Lambda$, surrounded by air ($\epsilon = 1$). This triangular PhC is obtained simply by removing one of the sublattices of a unit cell of the HC VPhCs studied in this project (here, we chose to remove the rods with a smaller radius). A Z-shape bend waveguide is formed by removing rods along a Z-shape path shown in Fig. 5.10. The Si rods are represented with white color against the air background (black color). In order to calculate the transmission, we place “intensity detectors” at the 4 locations marked A to D.

The incident Gaussian beam may propagate in the air along the waveguide while being reflected by Si rods in a complicated manner, if the beam’s frequency lies within the bandgap of the surrounding crystal. Fig. 5.11 is the photonic band structure of the PhC obtained using Program 1, showing that the TM bandgap between the first and second bands lies between normalized frequencies $0.25\omega\Lambda/2\pi c$ and $0.37\omega\Lambda/2\pi c$ (the gap-midgap ratio is 0.39). We thus expect that light will propagate along the waveguide in this frequency interval.

Photonic Band Structure and Electric Field Magnitude Distribution

Here, we use Program 2 in order to obtain the band diagram for the triangular lattice PhC with a waveguide that is formed by removing a line of Si rods horizontally (the translational symmetry is preserved in the x direction). Fig. 5.12 illustrates the geometry of the waveguide, where the

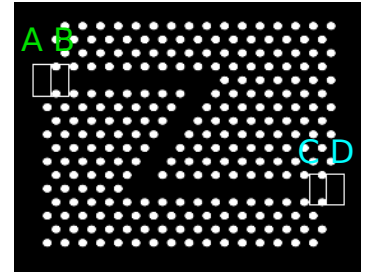


Figure 5.10: Geometry of a Z-shape waveguide formed by removing Si rods from the PhC formed by 16×16 rods. The position of intensity detectors (A, B, C, and D) are indicated as rectangles at the entrance/exit areas.

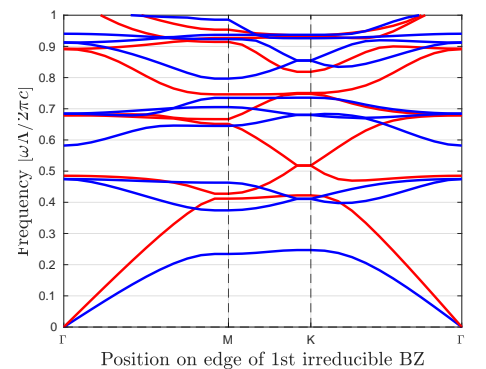


Figure 5.11: The photonic band structure of the 2D PhC, having triangular array of Si ($\epsilon = 11.7$) columns with $r = 0.25\Lambda$ in the air

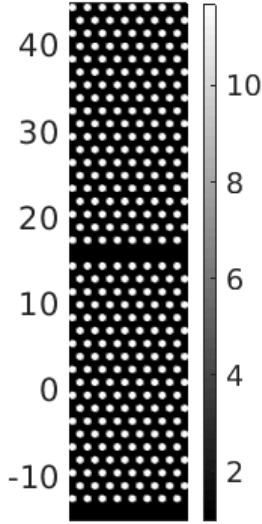


Figure 5.12: Schematic diagram (dielectric constant map) of the triangular lattice PhC with a line defect

unit cell is a rectangle sized $\sqrt{3}a \times 3a/2$, where $a = \Lambda/\sqrt{3}$, and the supercell sized $\sqrt{3}a \times 30a/2$, where 10 unit cells are arranged vertically, is repeated 2 times in the vertical direction and 8 times in the horizontal direction.

With this structure, Program 2 produces the photonic band structure shown in Fig. 5.13 (a), where the linear-defect mode appearing in the PBG is marked with red color and bulk modes in black color. We see that the light propagates in the waveguide at the group velocity $\frac{d\omega}{dk_x} > 0$ from a normalized frequency of around $0.32\omega\Lambda/2\pi c$. Fig. 5.13 (b) shows the distribution of electric field magnitude at $k_x/G_x = 0.0$ (0.32), 0.1 (0.33), 0.2 (0.35), 0.3 (0.38), 0.4 (0.38), 0.5 (0.37) (the numbers in parentheses are normalized frequencies). The light confinement is the strongest up to around $k_x/G_x = 0.2$ located at around the middle frequency of the PBG. The waveguiding effect disappears around $k_x/G_x = 0.3$, above which the defect-mode joins the upper bulk mode.

Results of Calculating Intensities

We modified Program 3 in order to calculate not only electric field at any position within the window, but also the intensities detected by the 4 detectors.

Qualitative Analysis

First, we qualitatively study what is happening in the waveguide. According to our analysis shown in Fig. 5.13, the linear-defect band (guided modes) starts from a normalized frequency of $0.32\omega\Lambda/2\pi c$. Fig. 5.14 supports this; at $0.30\omega\Lambda/2\pi c$, the light does not penetrate the PhC at all as expected, and at $0.32\omega\Lambda/2\pi c$, the light does propagate in the waveguide. In Fig. 5.14 (b), we see that the light is strongly reflected at the first bend (we consider this phenomenon later), and the electric field magnitudes in the remaining two straight segments are very weak. Standing waves (with different wavelengths) are formed in all the three straight segments, and the waveguide is a poor resonator.

Fig. 5.15 illustrates that the light is confined within the Z-shape waveguide at normalized frequencies within the bandgap (0.34 and $0.37\omega\Lambda/2\pi c$), but the light spreads through the entire PhC at a frequency higher than the bandgap interval ($0.38\omega\Lambda/2\pi c$). Similar patterns as Fig. 5.15 (b) are observed at $0.34\omega\Lambda/2\pi c$ and $0.37\omega\Lambda/2\pi c$; the differences are that the standing waves formed throughout the waveguide have different wavelengths and amplitudes. We see that this structure confines light, but does not function as a waveguide nor provide a broadband transport: the guided mode occupies only 50% of the bandgap interval.

Quantitative Analysis

In order to examine how much incident light will propagate and come out from the waveguide, we calculate the intensity measured by the 3 detectors B, C, and D. The intensity measured by detector A is excluded from the calculation because it ‘detects’ both the incident light and the light reflected by the PhC, and thus does not represent the intensity of the incident beam. The intensity is defined here as the sum of square electric field magnitude at all grid points within the rectangles (detectors) placed at the entrance and exit of the waveguide divided by the area. For example, with the incident

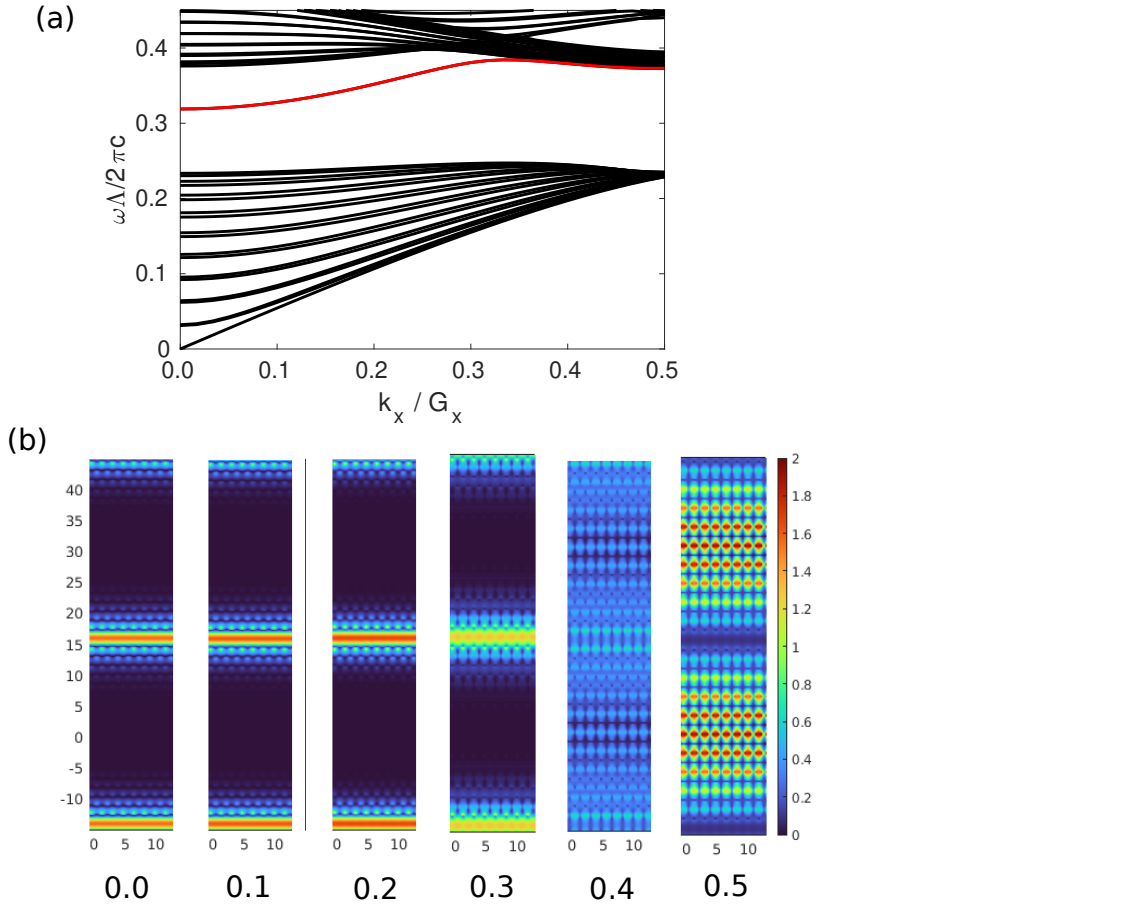


Figure 5.13: (a) Photonic band structure for the geometry shown in Fig. 5.12, (b) Distribution of electric field magnitude at $k_x/G_x = 0, 0.1, 0.2, 0.3, 0.4, 0.5$

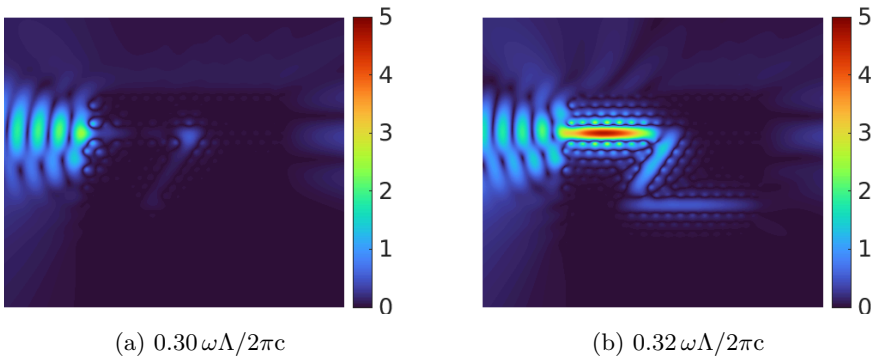


Figure 5.14: Distribution of electric field magnitude of the PhC with a Z-shape waveguide (16 × 16 rods) for two normalized frequencies

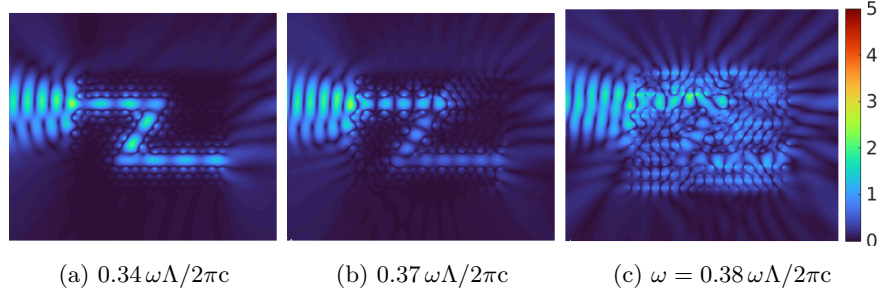


Figure 5.15: Distribution of electric field magnitude of the PhC with a Z-shape waveguide (16×16 rods) for three normalized frequencies

intensity I_{in} and the intensity detected at the exit I_{out} (rectangles marked as B and C in Fig. 5.10), we calculate a kind of transmission T given as

$$T = \frac{I_{\text{out}}}{I_{\text{in}}}, \quad \text{where} \quad (5.1)$$

$$I_{\text{in}} = \sum_i |\text{abs}(E_i)|^2 / A \quad (5.2)$$

$$I_{\text{out}} = \sum_j |\text{abs}(E_j)|^2 / A, \quad (5.3)$$

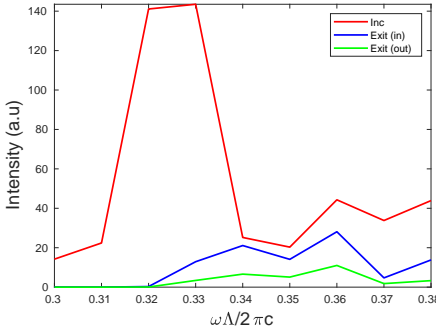


Figure 5.16: The intensity measured by the 3 detectors: B at the beginning of the waveguide (“inc”) marked in red color, C at the end of the waveguide (“Exit (in)”) marked in blue, and D just outside the waveguide (“Exit (out)”) marked in green.

where A is the area of the rectangle and i (j) is the index for grid points in the rectangle at the entrance (exit) of the waveguide. It must be noted that this transmission may exceed unity depending on the amplitude of undulating waves caught by the “detectors.” Nonetheless, it captures the general trend of how much of the incident light propagates through to the exit.

In case of the waveguide in the PhC, the incident beam may be reflected at the sharp bends (the degree depends on the frequency) and, as a result, the electric field magnitude at the exit is always smaller than the magnitude at the entrance. Fig. 5.16 plots the intensity measured by the 3 detectors. Although detectors B and C are placed near the nodes (not reflecting the amplitude of waves), the plots show that the intensity drops every time light is reflected at a bend, and that the difference between the blue and green plots is always significant (the intensity drops by $1/3$ to $1/4$ when the light exits the waveguide), reflecting the resonator effect.

Comparison with Straight-line Waveguide

We repeat the same analysis above using a straight-line waveguide having the same length as the Z-shape waveguide. Fig. 5.17 shows the geometry (dielectric constant map) of the PhC and locations/size of the 4 detectors.

Fig. 5.18 presents the distribution of electric field magnitude for the PhC with a straight-line waveguide for normalized frequencies $0.32 \omega \Lambda / 2 \pi c$ and $0.34 \omega \Lambda / 2 \pi c$. At frequency $0.32 \omega \Lambda / 2 \pi c$, the light is strongly confined in the waveguide, while the confinement is much lower at higher frequencies from $0.33 \omega \Lambda / 2 \pi c$ to $0.37 \omega \Lambda / 2 \pi c$ (not shown). The distribution is more

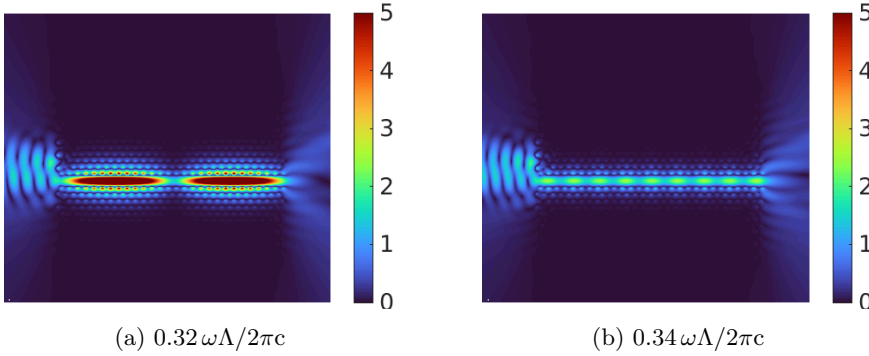


Figure 5.18: Distribution of electric field magnitude of the PhC with a straight-line waveguide (28×28 rods)

or less the same as for the Z-shape bend waveguide; the straight waveguide also functions as a resonator. At normalized frequency $0.32 \omega \Lambda / 2\pi c$, $k_x / G_x \approx 0$ as seen from Fig. 5.13 (a), and the standing wave with the long wavelength and strong electric field magnitude is explained from the following magnitude calculation, where the wave is the sum of propagating and reflected waves (setting wave amplitude to 1):

$$\begin{aligned} |e^{ik_x x} + r e^{-ik_x x}|^2 &= (e^{ik_x x} + r e^{-ik_x x})(e^{-ik_x x} + r^* e^{ik_x x}) \\ &= 1 + |r|^2 + r^* e^{2ik_x x} + r e^{-2ik_x x} \\ &= 1 + |r|^2 + 2|r| \cos(2k_x x + \theta), \end{aligned} \quad (5.4)$$

where r is the reflection coefficient, r^* is its complex conjugate, and θ is an arbitrary phase shift. The third term in (5.4) represents the spatial oscillation part, whose wavelength is long for small k_x , and the magnitude increases for higher r . Fig. 5.19 shows the intensities at the 3 detectors. Compared to Fig. 5.16, the red and blue curves are flipped; because there are no sharp bends, the waveguide functions as a single resonator and the intensities at the entrance and exit are nearly the same. Fig. 5.20 compares the transmission calculated according to (5.1) between the Z-shape bend and straight-line waveguides for triangular PhC. Clearly, the transmission is lower for the Z-shape waveguide because the light is reflected at two sharp bends.

5.2.2 Propagation of Light in Zigzag-edge Domain Walls

In the same way as for the previous section, we construct the Z-shape bend and straight-line domain-walls of type A using the VPhCs A and B explained in Section 5.1, and position 4 detectors at the entrance and exit as shown in Fig. 5.21.

We know from Fig. 4.14 that the photonic bandgap exist at frequencies from $0.244 \omega \Lambda / 2\pi c$ to below $0.268 \omega \Lambda / 2\pi c$, and that robust kink states are obtained when k_x / G_x values lie between the two valley points (corresponding to normalized frequencies of $0.24 \omega \Lambda / 2\pi c$ to $0.26 \omega \Lambda / 2\pi c$).

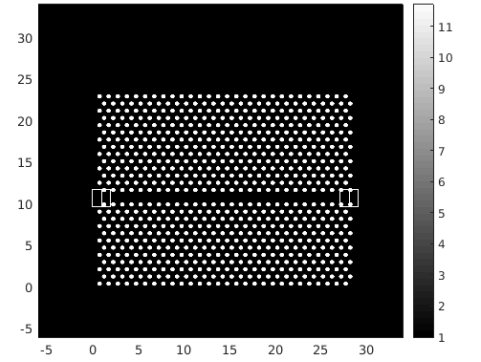


Figure 5.17: Geometry of a straight-line waveguide formed by removing Si rods horizontally at the center of the PhC formed by 28×28 rods. The location of the intensity detectors are indicated as white rectangles at the entrance/exit areas.

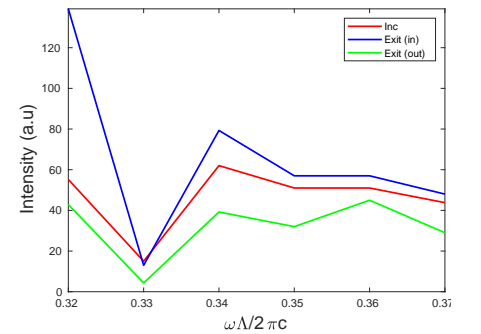


Figure 5.19: The intensity measured by the 3 detectors: B at the beginning of the waveguide (“inc”) marked in red color, C at the end of the waveguide (“Exit (in)”) marked in blue, and D just outside the waveguide (“Exit (out)”) marked in green.

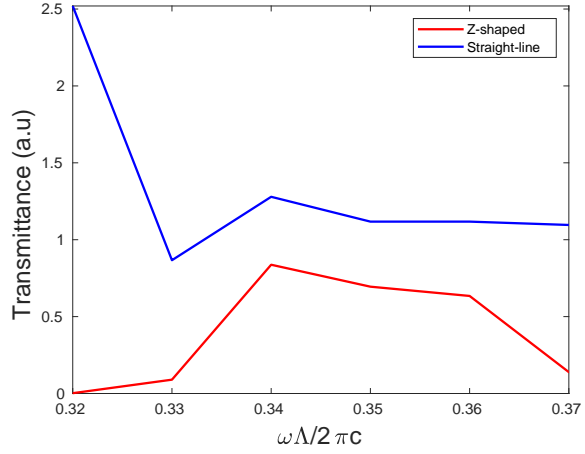
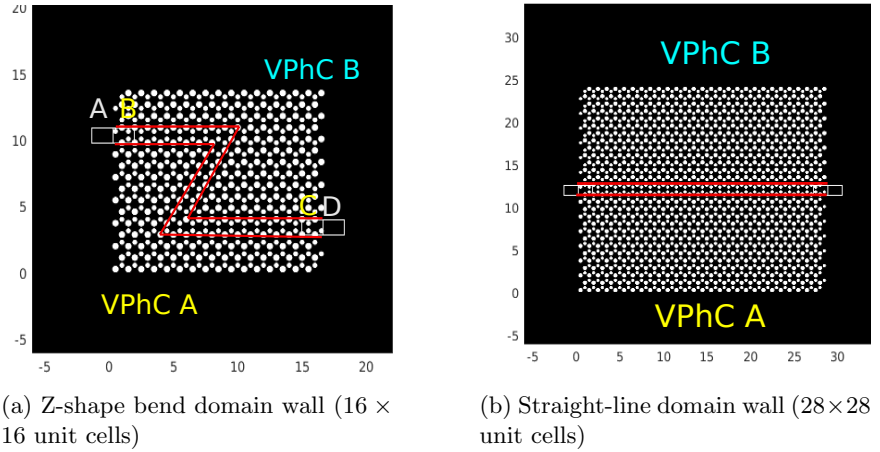


Figure 5.20: Comparison of transmission between the Z-shape bend and straight-line waveguides for triangular PhC.



(a) Z-shape bend domain wall (16×16 unit cells)

(b) Straight-line domain wall (28×28 unit cells)

Figure 5.21: Geometry for calculating transmission for zigzag-edge domain wall. The electric field is detected at the 4 detectors represented as white rectangles placed at the entrance (A and B) and exit (C and D). Both kink-states have the same length of 28Λ .

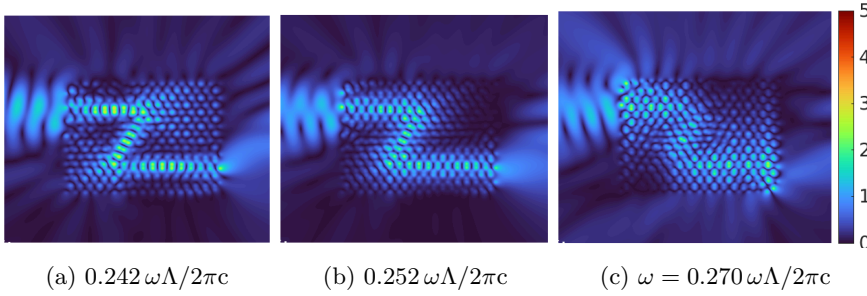


Figure 5.22: Distribution of electric field magnitude of the valley-PTI with a Z-shape bend domain wall (16×16 unit cells)

Comparison between Z-shape Bend and Straight-line Domain Walls

Qualitative Analysis

We first compare the distribution of electric field magnitude along the Z-shape bend domain wall among different frequencies. As expected, the beam propagates along the domain wall, but the robustness varies depending on the frequency. Fig. 5.22 compares the distribution of electric field magnitude among three arbitrary frequencies; the light confinement is maximum at frequency $0.242 \omega\Lambda/2\pi c$ (corresponding to point A3 in Fig. 4.14), and the light is less confined at higher frequencies.

It is observed that the wave propagates with a certain wavelength, which is confirmed by the undulation of field magnitude, but maintains nearly constant strength throughout the domain wall, even after the two sharp bends. Also, there is no noticeable resonator effect, as seen in Figs. 5.14 and 5.18. Furthermore, the kink state provides waveguiding in the frequency interval corresponding to the entire bandgap, as compared to the ordinary PhC waveguide where the waveguiding occurs only at part of the bandgap frequencies.

In case of a straight-line domain wall, we see the undulation pattern more clearly. The tendency of decreasing light confinement with higher frequencies is also observed here, as shown in Fig. 5.23. This is because the guided mode at normalized frequency of $0.244 \omega\Lambda/2\pi c$ is located at the middle of the $K - K'$ interval, while that of $0.260 \omega\Lambda/2\pi c$ is located outside the interval (see Fig. 4.14).

Quantitative Analysis

Fig. 5.24 presents the results of calculating intensities at 4 detector positions: just outside and inside the entrance to the waveguiding domain wall as well as just before and after the exit of the domain wall. Similar tendencies of intensities are observed in both types of domain walls, and the intensity values are also in the same range. This implies that the effect of the sharp bends is very small; the beam propagates along the Z-shape bend domain wall as if it travels straight through a linear domain wall without being reflected.

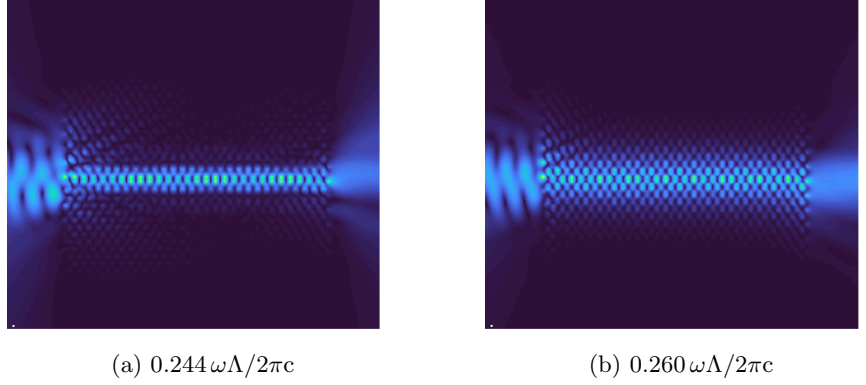


Figure 5.23: Distribution of electric field magnitude of the valley-PTI with a straight-line domain wall (28×28 unit cells).

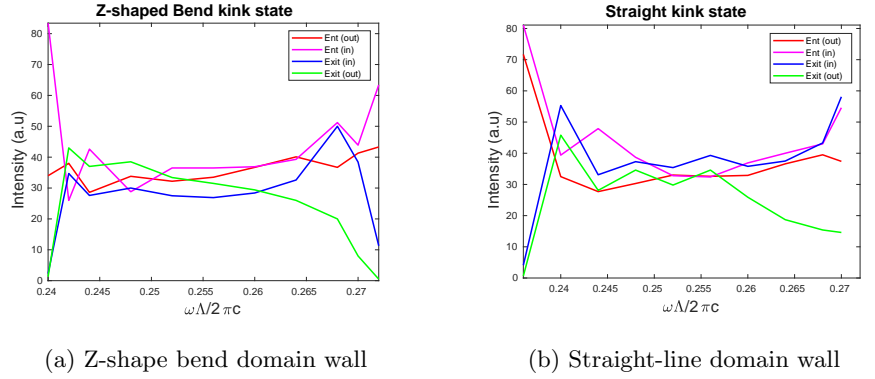


Figure 5.24: Intensities measured at the 4 locations shown in 5.21a: A: just outside the entrance of the waveguiding domain wall (Ent(out)) marked with red color, B: just inside the domain wall (Ent(in)) marked with magenta, C: just before the exit of the domain wall (Exit(in)) marked with blue, and D: after the exit of the domain wall (Exit(out)) marked with green

Fig. 5.25 shows the result of calculating transmission according to (5.1); it compares transmission between Z-shape bend and straight-line domain walls¹. T_1 is the ratio of the intensity of light propagating to the end of exit (Exit(in)) and the incident light intensity (Ent(in)), while T_2 is the ratio of the intensity of light exiting the domain wall (Exit(out)) and the incident light intensity (Ent(in)):

$$T_1 = \frac{\text{Exit(in)}}{\text{Ent(in)}} \quad (5.5)$$

$$T_2 = \frac{\text{Exit(out)}}{\text{Ent(in)}} \quad (5.6)$$

¹Data for frequency $0.272 \omega \Lambda / 2 \pi c$ for the straight-line domain wall is missing because the code failed to run to the end.

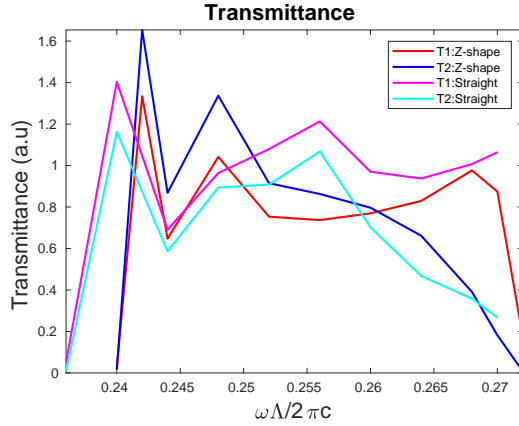


Figure 5.25: Comparison of transmission between Z-shape bend and straight line domain walls. Z-shape bend: Red (T_1) and blue (T_2), Straight-line: magenta (T_1) and cyan (T_2).

It is confirmed that the transmittance is 70% or higher throughout the bandgap interval (dropping to 20% at frequency $0.272 \omega\Lambda/2\pi c$ and 0 outside the bandgap) for both types of domain walls. This illustrates that the light is not lost significantly at the sharp corners or due to reflection/scattering to bulk, proving that the valley kink states are basically free of backscattering.

5.2.3 Propagation of Light in Bearded-stack Domain Walls

In this section, we repeat the same analysis as above for the bearded-stack domain walls for the purpose of comparing the kink state robustness against the zigzag-edge domain walls.

Photonic Band Structure and Electric Field Magnitude Distribution

We first present the photonic band structure and the distribution of electric field magnitude obtained using Program 2 for the bearded-stack domain walls. Fig. 5.26 shows the dielectric constant map and illustrates two types of interfaces. Bigger rods are interlaced for interface A while smaller rods are interlaced for interface B.

Fig. 5.27 (a) shows the photonic band structure of the bearded-stack interfaces. Comparing with the band structure of the zigzag-edge domain walls shown in Fig. 4.14, we see that there are no kink states at the mid points between the two valley points (points A5 and B5). Fig. 5.27 (b) shows the distribution of electric field magnitudes corresponding to the points marked on Fig. 5.27 (a).

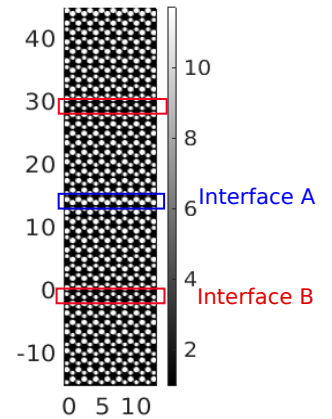


Figure 5.26: Dielectric map of bearded-stack domain wall: Interface A: Big rods interlaced, Interface B: Small rods interlaced

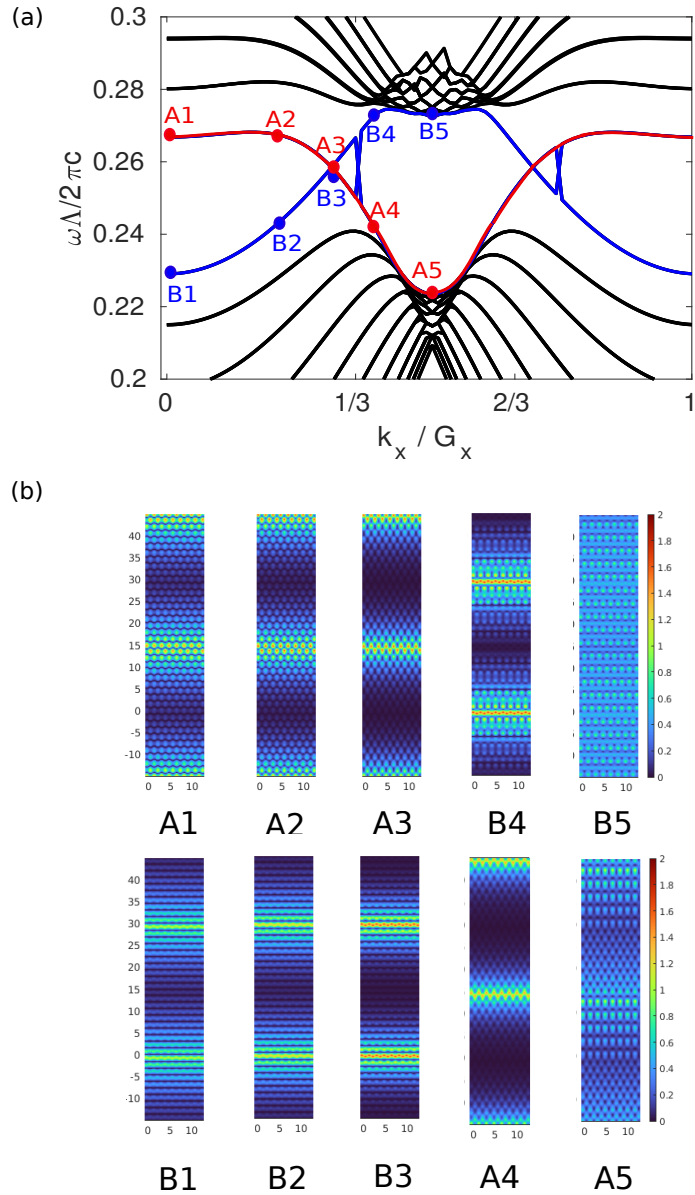


Figure 5.27: (a) Band diagram for the geometry in Fig. 5.26, showing the two types of valley-dependent kink states. Note that the 'X'-shaped crossings around $k_x/G_x = 1/3$ and $k_x/G_x = 2/3$ are numerical artifacts and may be ignored. (b) The distribution of electric field magnitude for the two bands located in the bandgap, for the points marked in (a)

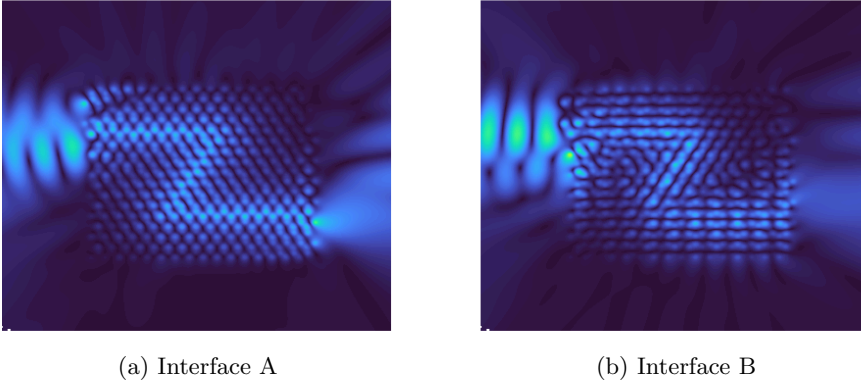


Figure 5.28: Comparison of distribution of electric field magnitude between interfaces A and B at normalized frequency $0.248 \omega \Lambda / 2\pi c$

Comparison between Z-shape Bend and Straight-line Domain Walls

We first compare the distribution of electric field magnitude between interfaces A and B to see which interface confines light better. Fig. 5.28 shows an example of comparison at normalized frequency $0.248 \omega \Lambda / 2\pi c$. In general, interface A (bigger rods interlaced at the interface) shows clearer Z-shape light confinement throughout the frequency range where the waveguiding effect is seen, i.e., from $0.244 \omega \Lambda / 2\pi c$ to $0.264 \omega \Lambda / 2\pi c$. We therefore choose to compare interface A of bearded-stack domain wall against interface A of zigzag-edge domain wall. Fig. 5.29 present the geometries we prepared for the comparison, in the same way as for the triangular PhC waveguide and valley-PTI with zigzag-edge domain wall.

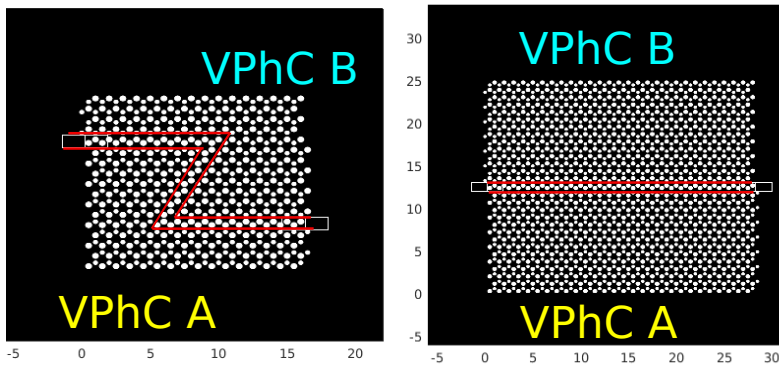


Figure 5.29: Geometry for calculating transmission for bearded-stack domain wall. The electric field is detected at the 4 detectors represented as white rectangles placed at the entrance and exit (2 each). Both domain walls have the same length of 28Λ .

Qualitative Analysis

Fig. 5.30 shows an example of how light confinement varies depending on the frequency for the straight-line domain wall. We note that the width of propagating light increases as the frequency increases, but the difference is not very significant for both types of domain walls, as indicated by the electric field distribution at points A1 to A4 in Fig. 5.27.

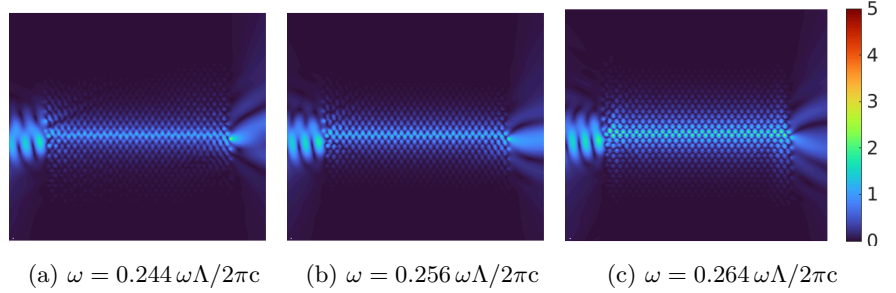


Figure 5.30: Distribution of electric field magnitude of the valley-PTI with a straight-line domain wall (28×28 unit cells)

Quantitative Analysis

Figs. 5.31 and 5.32 present the same analyses of intensities/transmission as for the zigzag-edge domain walls. The data is shown for the frequency range from $0.244 \omega\Lambda/2\pi c$ to $0.268 \omega\Lambda/2\pi c$ only, outside of which the waveguiding effect is not available. We see that intensities obtained by the 4 detectors are almost the same for both the Z-shape bend and straight-line domain walls. Consequently, there is little difference in transmissions T_1 and T_2 between the two types of domain walls.

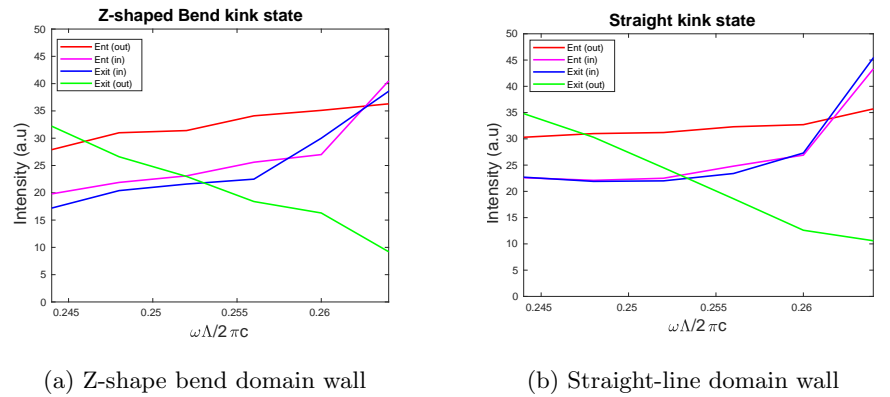


Figure 5.31: Intensities measured at the 4 locations of the PTI: just outside the entrance to the waveguiding domain wall (Ent(out)) marked with red color, just inside the domain wall (Ent(in)) marked with magenta, just before the exit of the domain wall (Exit(in)) marked with blue, and after the exit of the domain wall (Exit(out)) marked with green

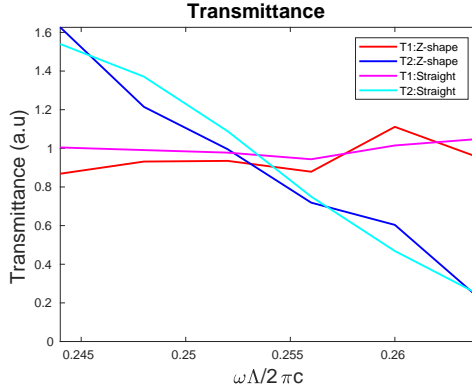


Figure 5.32: Comparison of transmittance between Z-shape bend and straight line. Z-shape bend: Red (T_1) and blue (T_2), Straight-line: magenta (T_1) and cyan (T_2).

Comparison of Robustness between Zigzag-edge and Bearded-stack Interfaces

We compare the robustness of the kink states between the zigzag-edge and bearded-stack interfaces by comparing average difference of transmissions T_1 and T_2 between the Z-shape bend and straight-line domain walls. For example, for T_1 , we calculate this average by taking the absolute value of difference of T_1 values between the Z-shape bend and straight-line domain walls for the frequency range 0.244 to 0.264 at intervals of 0.004, summing them up, and dividing by the number of sampling points ($N = 6$) for both types of interfaces:

$$\Delta \bar{T}_1 = \frac{1}{N} \sum_{i=1}^N |T_{1,\text{zbend}}(\omega_i) - T_{1,\text{straight}}(\omega_i)|, \quad \omega_i \in \{0.244, 0.248, \dots, 0.264\}$$

For the zigzag-edge interface, the average differences of T_1 and T_2 values between the Z-shape bend and straight-line domain walls are 0.2052 and 0.2042, respectively. The same values for the bearded-stack interface are 0.0824 and 0.0869, respectively, implying that transmission is nearly the same for the Z-shape bend and straight domain walls. The bearded-stack interface is thus more robust than the zigzag interface. We conclude that our first hypothesis H1 is supported, since the PhC waveguide does not provide as broadband and robust transport as any of the domain wall types of valley-PTIs investigated, and that a bearded-stack interface with bigger rods interlaced at a domain wall is the most robust among the interfaces investigated in this section.

5.3 Unidirectional Coupling – Chiral Light-Matter Interaction

In this section, we investigate how a chiral magnetic dipole couples to a kink state for the case of 2D VPhCs having HC lattice of cylindrical silicon rods in air to see if our hypotheses H2 and H3 are supported.

5.3.1 Method for Testing the Hypotheses

To test these hypotheses, we form an inverse- Ω bearded-stack domain wall in a VPhC consisting of 16×16 unit cells shown in Fig. 5.33, as well as a straight line domain wall consisting of 24×24 unit cells (not shown). We chose rod radii of $r_A = 0.25\Lambda$ and $r_B = 0.19\Lambda$ and the normalized frequency $0.26\omega\Lambda/2\pi c$ (the PBG ranges from $0.244\omega\Lambda/2\pi c$ to $0.272\omega\Lambda/2\pi c$ for this valley-PTI).

Program 3 is used for two purposes: 1) to plot distribution of electric field magnitude when dipoles of opposite polarization \mathbf{d}_{\pm} are placed at arbitrary locations along the domain wall (referred to as Program 3_{EF}), and 2) to calculate the inner product between the magnetic field and the chiral magnetic moments, $\mathbf{H} \cdot \mathbf{d}_{\pm}$, at each grid point and plot the values (referred to as Program 3_{IP}). See Section 3.3.5 for how to calculate magnetic field and inner product.

The following magnetization source density for a chiral magnetic dipole located at position \mathbf{r}_0 is defined:

$$\mathbf{M}(\mathbf{r}) = \frac{M}{\sqrt{2}}(\hat{\mathbf{x}} \pm i\hat{\mathbf{y}})\delta(\mathbf{r} - \mathbf{r}_0), \quad (5.7)$$

where M is the magnitude of the magnetic dipole moment and $\mathbf{d}_{\pm} = \frac{1}{\sqrt{2}}(\hat{\mathbf{x}} \pm i\hat{\mathbf{y}})$ is the chiral dipole moment. See Section 3.3.4 for implementation into Program 3.

To quantitatively determine UDC, we follow [RHZD21] and define the directionality for a given frequency as

$$D = \frac{P_L - P_R}{P_L + P_R}, \quad (5.8)$$

where P_L and P_R are the optical power detected at the left and right ends, respectively. We measure the power as the sum of the square of all electric field magnitude values of all grid points in the rectangles at the left and right ends of the valley-PTI named E_L (light blue) and E_R (light green) in Fig. 5.33, divided by the area. The UDC efficiency can then be defined as

$$\beta = \frac{P_L}{P_L + P_R}. \quad (5.9)$$

5.3.2 Directionality of 2D Honeycomb Lattice Silicon Rods: Preliminary Testing

We tested various dipole locations in the bearded-stack domain wall shown in Fig. 5.34, for the case of \mathbf{d}_+ , to see if we obtain the same results as

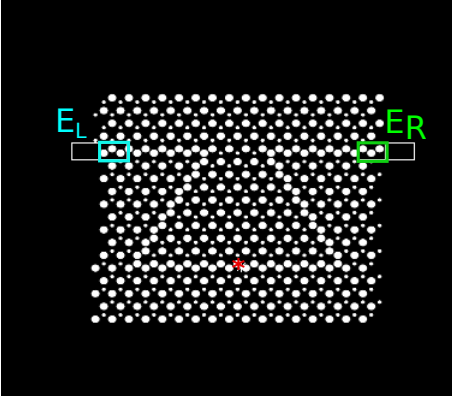


Figure 5.33: Geometry of bearded-stack interface with larger rods. The position of a chiral magnetic dipole is marked with the red asterisks. The detector positions are indicated by colored rectangles.

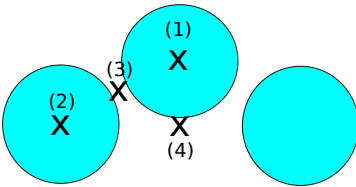


Figure 5.34: Positions of magnetic dipole. (1) On the center large rod in the upper domain, (2) on the large rod in the lower domain, to the left of the center rod, (3) between the two large rods, (4) just below the center rod

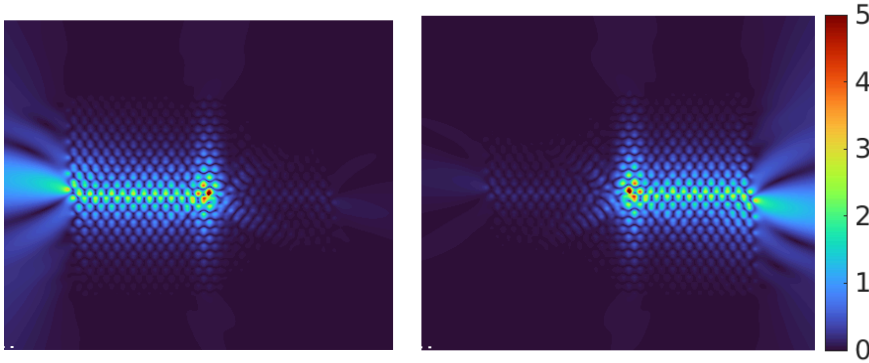
(a) Magnetic dipole moment \mathbf{d}_- (b) Magnetic dipole moment \mathbf{d}_+

Figure 5.35: Distribution of electric field magnitude of the valley-PTI with a straight-line waveguide (24×24 unit cells) at normalized frequency $0.26 \omega \Lambda / 2\pi c$

the silicon PhC slabs with air holes studied by [RHZD21] and [HLY⁺19]. We found that dipole locations achieving high UDC efficiencies are different from those studies; the highest efficiency in UDC is observed when a \mathbf{d}_+ dipole is placed immediately below the silicon rod at the center (position (4)), rather than at (1) in Fig. 5.34. Furthermore, no UDC is observed at position (3), which is on the flow path in Fig. 1.8. Nonetheless, we observed that the propagation direction is reversed at dipole position (2). This result matches with [YHO21], which also studied PhC slabs with air holes.

We confirmed backscattering-free propagation of light, without reflection at the sharp bends in the inverse- Ω edge state. Fig. 5.35 shows the resulting distribution of electric field magnitude due to dipoles \mathbf{d}_\pm located on the center rod in the straight-line domain wall (position (1)). Directionality of ± 1 is achieved for dipoles \mathbf{d}_\pm . The directionality achieved for the inverse- Ω domain wall is also high, 0.9996 and 0.9976 for \mathbf{d}_- and \mathbf{d}_+ , respectively (corresponding plots are found in Fig. 5.39).

5.3.3 Explaining Directionality by Coupling Between Chiral Magnetic Dipole and Magnetic Field

To test the hypothesis H3, we used the straight line domain wall, let a Gaussian beam with a large waist radius hit the valley-PTI (to make the incident field homogeneous in the valley-PTI) from the left side, and calculate the x and y components of the total magnetic field (the sum of the incident field and the radiation from polarization currents at any other positions inside the valley-PTI) throughout the system. We then calculate the inner product between the magnetic field and the chiral magnetic moments, $\mathbf{H} \cdot \mathbf{d}_\pm$, at each grid point and plot the values. This process is performed using Program 3_{IP}. See Section 3.3.5 for how the inner product is calculated.

Fig. 5.36 presents the results. As expected, the inner product values are high along the domain wall. It is seen that areas of high and low inner

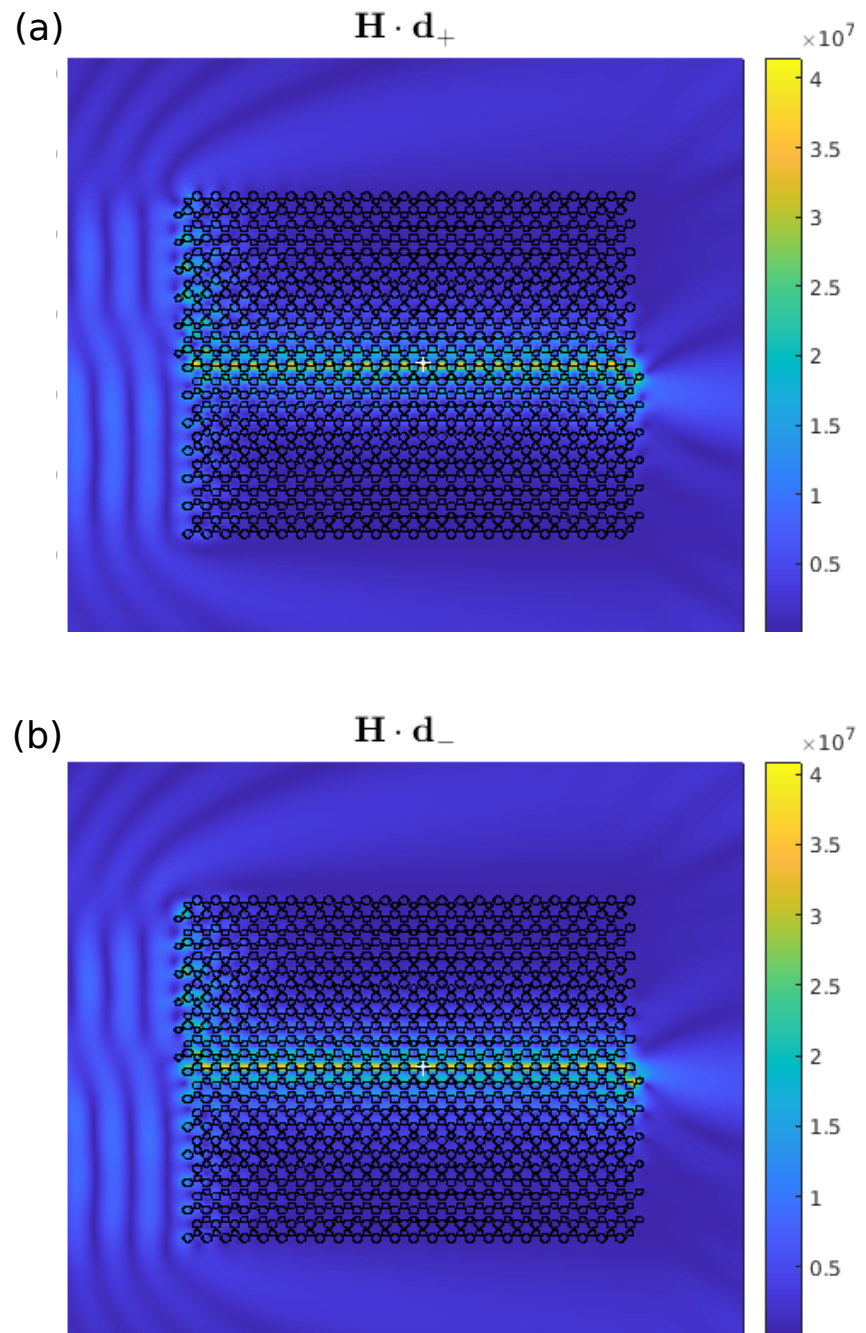


Figure 5.36: Distribution of magnitude of inner product (a) $\mathbf{H} \cdot \mathbf{d}_+$, (b) inner product $\mathbf{H} \cdot \mathbf{d}_-$ for the bearded-stack domain wall; the white cross indicates the location of the central rod.

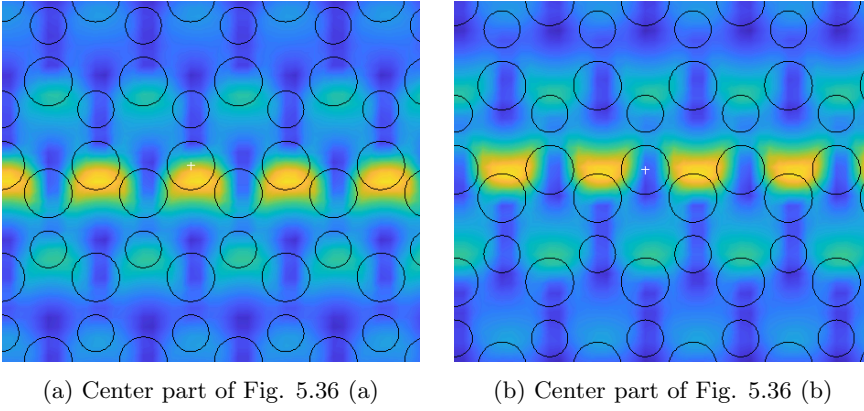


Figure 5.37: Center part of Fig. 5.36 with the same color scheme

product values alternate at the domain wall. Figs. 5.37 (a) and 5.37 (b) enlarge the central part of the domain wall shown in Fig. 5.36 (a) and (b), respectively. We see that high inner product areas are found at the boundary between the silicon rod in the upper domain and air for $\mathbf{H} \cdot \mathbf{d}_+$, and between the silicon rod in the lower domain and air for $\mathbf{H} \cdot \mathbf{d}_-$. We checked the correctness of this result by calculating the partial derivatives of the electric field numerically, and obtained a good match. For example, the resulting distribution of inner product for \mathbf{d}_+ by numerical differentiation is shown in Fig. 5.38, which is a good approximation of Fig. 5.36 (a).

Inner product $\mathbf{H} \cdot \mathbf{d}_+$

Here we analyze the directionality/UDC efficiency for \mathbf{d}_+ using the inverse- Ω domain wall. We take the unit cell located at the center and place a magnetic dipole \mathbf{d}_+ at 7 vertically aligned points for each of the two sublattice rods shown in Fig. 5.39, and examine the electric field magnitude distribution throughout the valley-PTI, using Program 3_{EF}.

Fig. 5.40 plots directionality D , UDC efficiency β , and average electric field strength at the left and right exits of the valley-PTI for each of 7 points shown in Fig. 5.39, for left sublattice (Fig. 5.40 (a)) and right sublattice (Fig. 5.40 (b)), respectively. The x axis (the positions of dipole emitter) corresponds to the numbers on Fig. 5.41.

Here, we conclude the following by comparing Figs. 5.39 and 5.40 against Fig. 5.36 (a):

- High inner product values are concentrated at the domain wall.
- The magnitudes of directionality D and UDC efficiency β are high for chiral dipole locations where the inner product value magnitude is high or low in Fig. 5.36 (a).
- The directionality is negative (propagation to the left) at locations where the inner product value is low, while the directionality is positive (propagation to the right) at locations where the inner product value

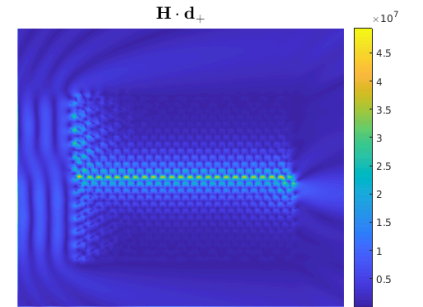


Figure 5.38: Distribution of inner product for \mathbf{d}_+ obtained using numerical differentiation

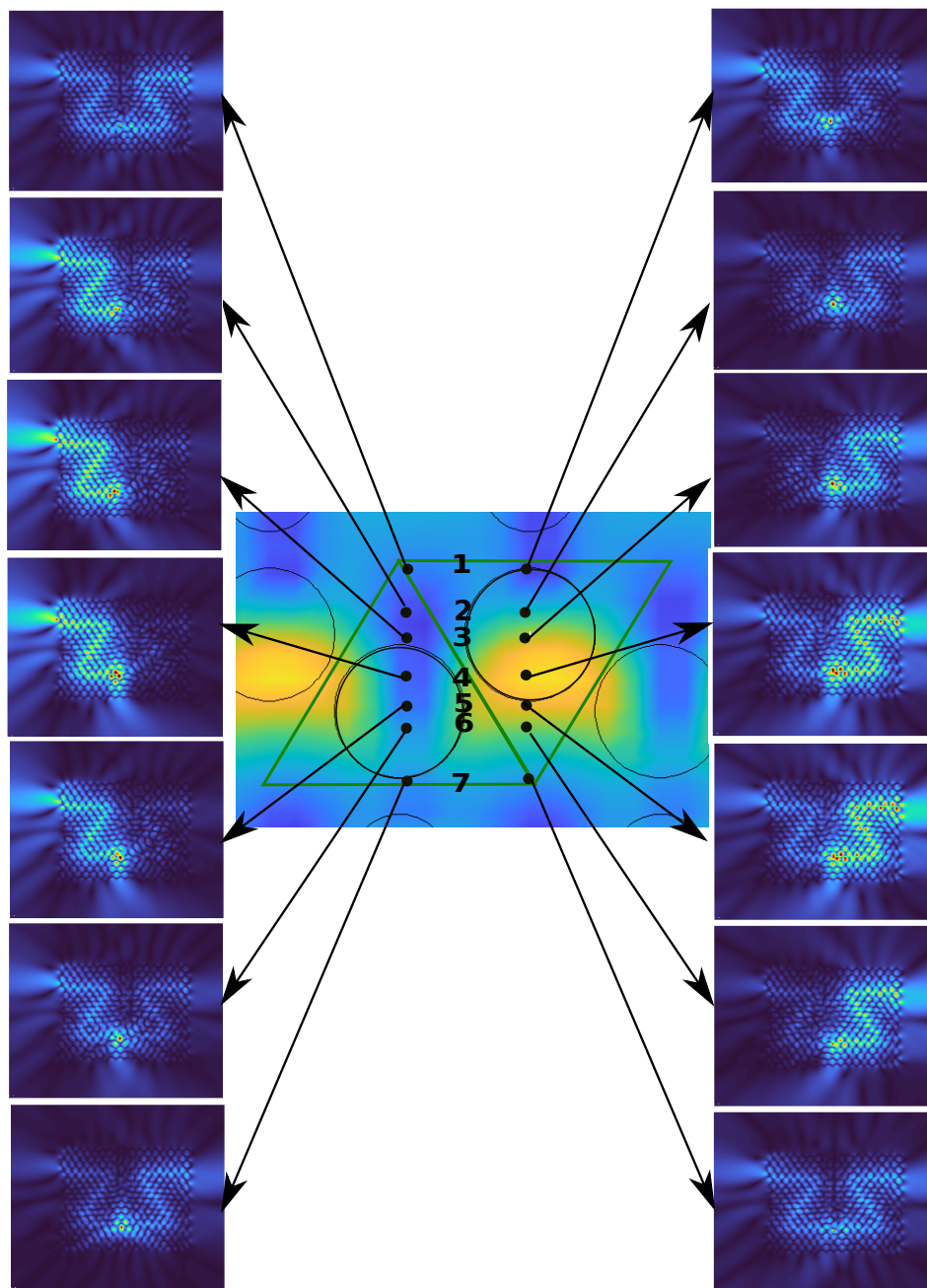


Figure 5.39: Change of electric field magnitude distribution when a magnetic dipole \mathbf{d}_+ is placed at various points

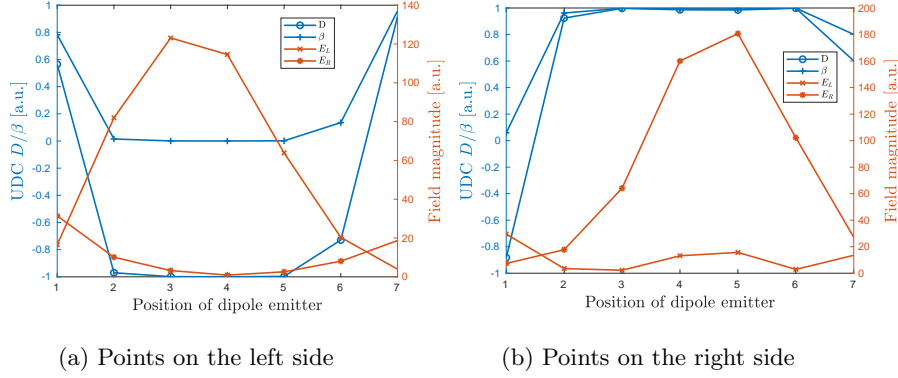


Figure 5.40: Directionality D , UDC efficiency β , and average electric field strength at the left and right exits for chiral magnetic dipoles located at the positions indicated in Fig. 5.39

is high in Fig. 5.36 (a). The dipole emitter is coupled to kink states corresponding to the K' and K valley points, respectively.

- The directionality is lost at locations where the inner product values take the mid-range values of around 2×10^7 , found at the outer edge of the domain wall.
- The points having high electric field magnitude at the exits shown in Figs. 5.40 (a) and 5.40 (b) are located at the interface between the silicon rod and air, agreeing well with positions of high inner product magnitudes in Fig. 5.36 (a).
- The magnitude of UDC efficiency for the left sublattice is smaller than that for the right sublattice. We do not have any good explanation for this.

Inner product $\mathbf{H} \cdot \mathbf{d}_-$

We conducted the same analysis for \mathbf{d}_- , and obtained results opposite of \mathbf{d}_+ , as expected from the distribution of inner product values shown in 5.36 (b). The distribution of electric field at various \mathbf{d}_- locations shown in Fig. 5.41 is a perfect mirror image of Fig. 5.39, and so are the plots of directionality D , UDC efficiency β , and average electric fields at the left and right exits shown in Fig. 5.42

If the Gaussian beam is incident from the right side of the valley-PTI, instead of from the left side, the inner product value patterns are flipped between \mathbf{d}_\pm . This is to be expected because this situation is obtained by rotating the original situation by 180° and flipping the y coordinate. The analyses above support our hypothesis H3; the UDC can also be explained by coupling between harmonic modes and chiral magnetic dipoles.

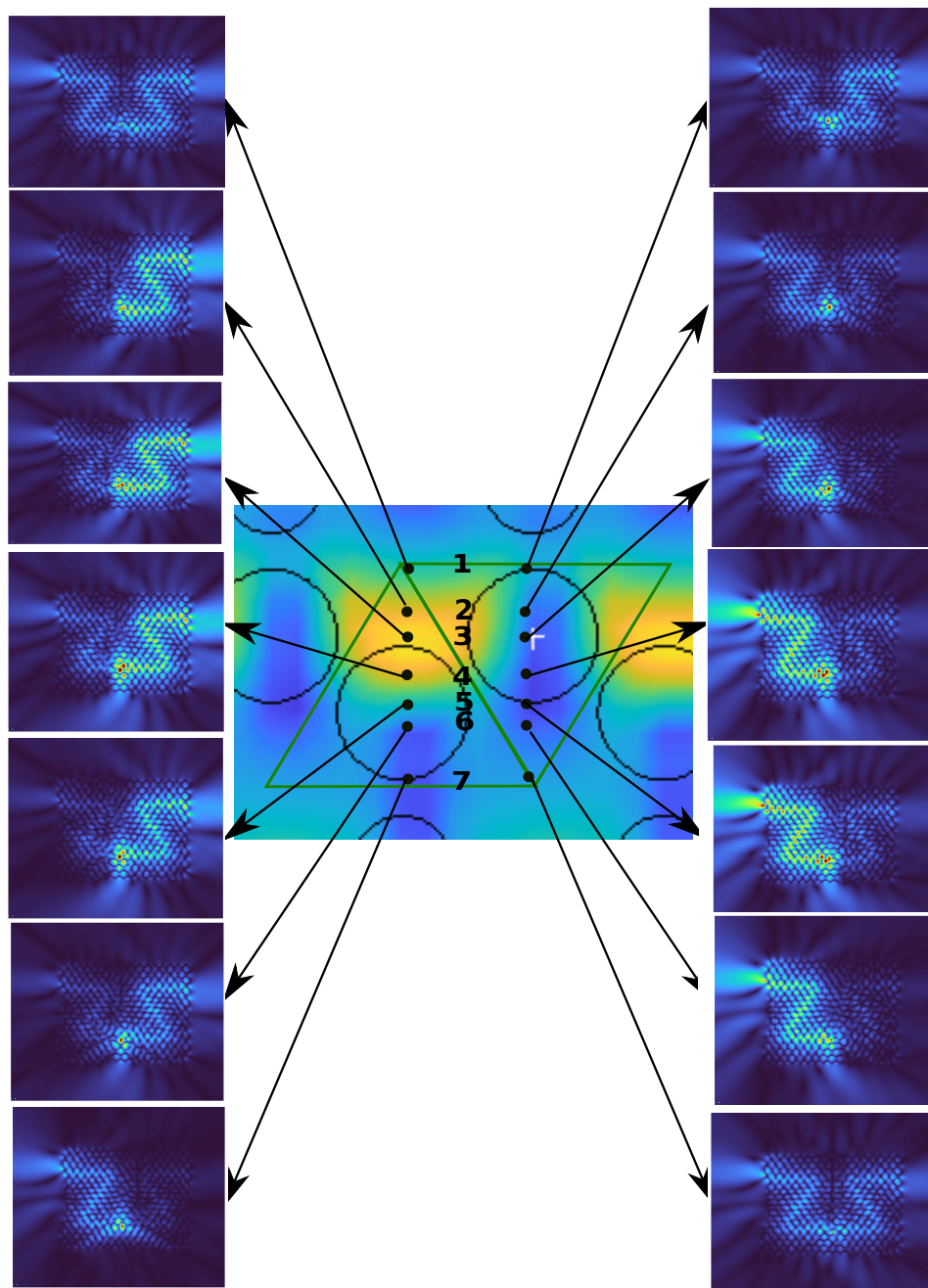


Figure 5.41: Change of electric field magnitude distribution along the vertical lines for the rods in the upper and lower domains

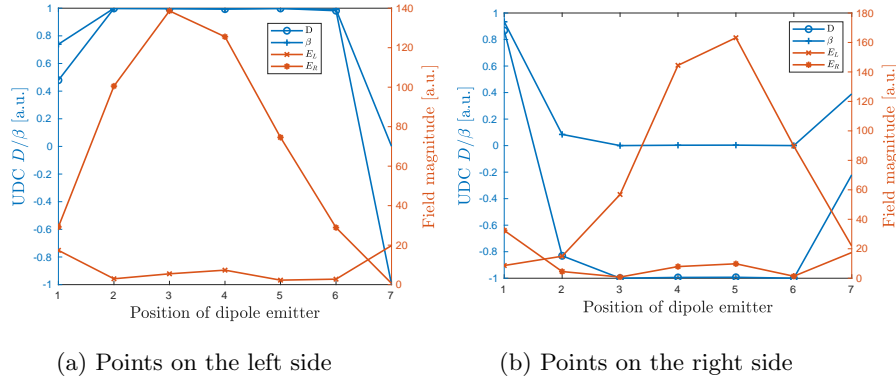


Figure 5.42: Directionality D , UDC efficiency β , and average electric field strength at the left and right exits for chiral magnetic dipoles located at the positions indicated in Fig. 5.41

5.3.4 Zigzag-edge Domain Walls

Finally, we tested if a zigzag-edge domain wall is actually not suited for high efficient UDC to test hypothesis H2. Figs. 5.43 presents the distribution of absolute values of inner products between the magnetic field and dipole moment \mathbf{d}_+ . Figs. 5.44 and 5.45 show enlarged views of the center part of the domain wall for dipoles of both chiralities. As in the case of the bearded-stack domain walls, the pattern of the inner products for \mathbf{d}_- is the mirror image of that of \mathbf{d}_+ . We see immediately that the magnitude is smaller than that of the bearded-stack domain wall (the maximum value is around 2.5×10^7), and that no high magnitude spots are found between the small rods that form the domain wall (high magnitude spots are found at the boundary between a big rod and air). Therefore, we conclude that our hypothesis H2 is supported; bearded-stack domain walls achieve higher UDC efficiency than zigzag domain walls.

Fig. 5.46 shows the distribution of electric field magnitude corresponding to various positions of \mathbf{d}_+ at the domain wall. Fig. 5.47 presents the directionality, UDC efficiency, as well as average electric field strength at the exits, as functions of the dipole positions. It is observed that the magnitude of electric field is lower than that of the bearded-stack domain wall (notice the colors in Fig. 5.46 and the values on the right y axis in Fig. 5.47), supporting hypothesis H2. It is seen that high directionality is obtained at locations with high magnitude of inner product values, supporting our hypothesis H3 in this structure as well. The main difference from the bearded-stack domain wall is that the directionality is zero when the source is placed at the center of the domain wall.

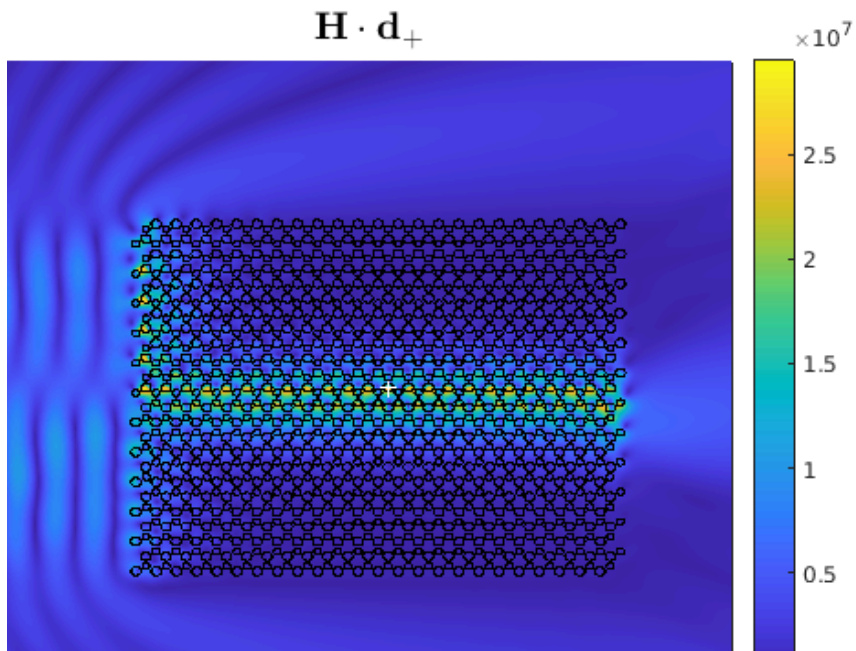


Figure 5.43: Distribution of magnitude of inner product $\mathbf{H} \cdot \mathbf{d}_+$ for the zigzag-edge domain wall; the white cross indicates the location of the central rod.

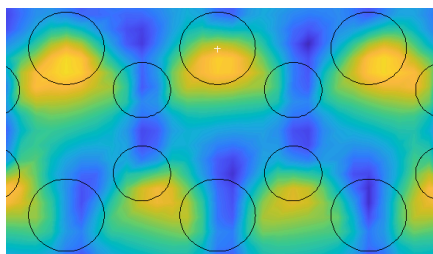


Figure 5.44: Center of the domain wall, enlarged for \mathbf{d}_+

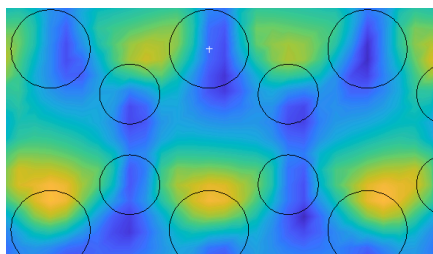


Figure 5.45: Center of the domain wall, enlarged for \mathbf{d}_-

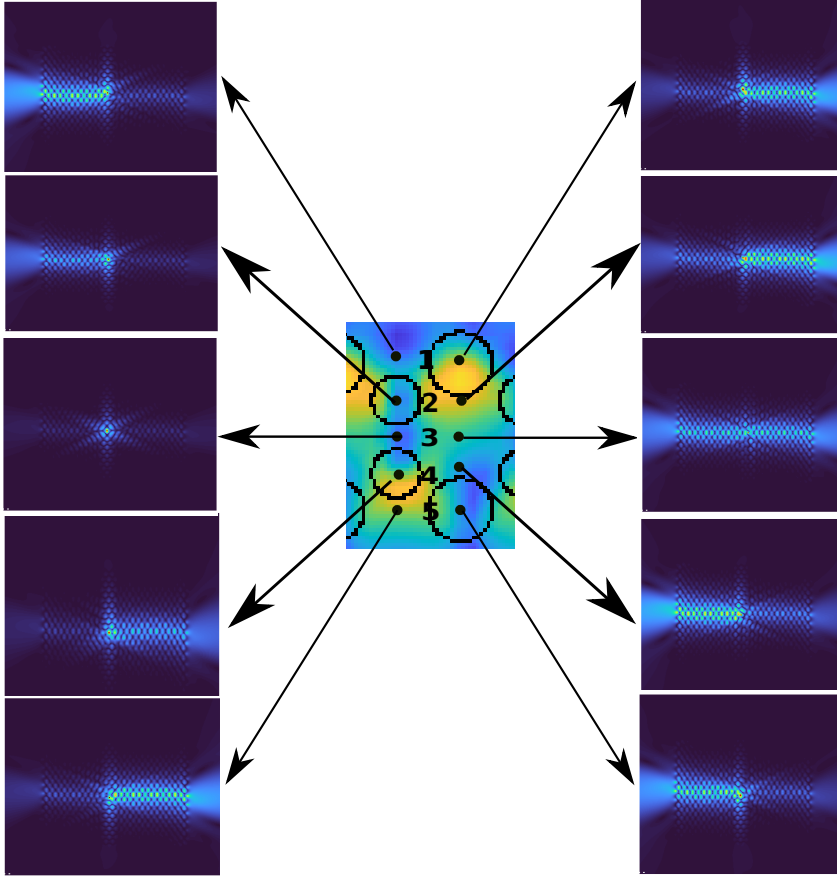
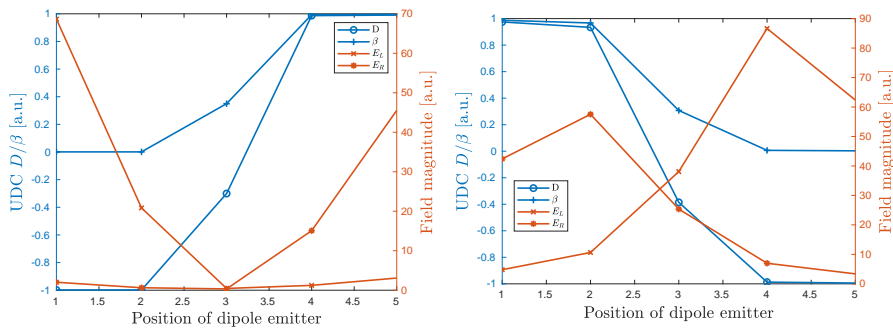


Figure 5.46: Change of electric field magnitude distribution along the vertical lines connecting small rods and larger rods



(a) Points on the left side

(b) Points on the right side

Figure 5.47: Directionality D , UDC efficiency β , and average electric field strength at the left and right exits for chiral magnetic dipoles located at the positions indicated in Fig. 5.46

5.4 Conclusion

This chapter documents the main findings of this project. First of all, we were able to show that the valley-PTI investigated here achieves robust kink states localized at the domain wall; if a Gaussian beam with a normalized frequency within the PBG hits the valley-PTI having Z-shape bends, the beam propagates along the domain wall and does not scatter into the bulk, because the states are protected by the PBG. We found that, among the various types of zigzag- and armchair-edge domain walls, a zigzag-edge domain wall formed with smaller rods achieves the most robust propagation.

Secondly, we tested hypothesis H1 and found it to be supported. We found that the most robust kink states are formed along bearded-stack domain walls of the valley-PTIs, as a result of comparing their transmission against zigzag-edge domain walls and line-defect waveguides in ordinary PhCs. While light propagates through the sharp corners without reflection in case of valley-PTIs, light is reflected at each corner and the exit of the waveguides of conventional PhCs.

Thirdly, regarding hypotheses H2 and H3, we confirmed that a chiral source placed in a bearded-stack domain wall excites the corresponding valley chiral states with near-unity directionality, and the observed behavior is explained by the magnitude of inner product with the magnetic field at the location. We also saw that it makes a considerable difference whether a structure is comprised of air or dielectric rods.

CHAPTER 6

Conclusion

In this Master's thesis project, we studied topological photonics, probably for the first time at AAU. We therefore tried to establish a foundation for students who will make their own challenges in this field hereafter, by providing a thorough review of the origin and types of topological photonics as well as presenting key features of valley photonic topological insulators through numerical calculations.

We stress that research in the area of valley photonic topological insulators, especially that of all dielectric materials, is a direct extension to the study on conventional photonic crystals, in which AAU has been actively involved over the years. Therefore, we were able to develop the tools necessary to investigate photonic topological insulators in this project, based on tools that have already been developed for photonic crystals by our supervisor.

Although researchers have already succeeded in discovering many structures that are more complicated, the valley photonic crystals we studied in this project have a very simple structure: cylindrical silicon rods in air forming a two dimensional honeycomb lattice. Nonetheless, we found that they are an ideal platform to develop a basic understanding of ideas and features of photonic topological insulators. By studying this structure, we witnessed rather exotic and surprising phenomena of valley photonic topological insulators. Moreover, we were able to identify possible research topics that have not been studied before.

In this project, we thus chose to work on two of the basic features of valley photonic topological insulators: robust light propagation and unidirectional coupling of chiral sources. For the former, our contribution is a systematic comparison of robustness of kink states among various types of domain walls, against conventional photonic crystal waveguides. Such comparisons have apparently not been made before, even though the backscattering free propagation, which does not happen in conventional photonic crystals, is the main reason why photonic topological insulators attract attention in the first place. For the latter, we explained the phenomenon of

unidirectional coupling of an external source to a kink state, by the coupling between harmonic modes and chiral magnetic dipoles. This phenomenon has been explained through matching between the chirality of orbital angular momentum of valley dependent kink states and the chirality of the external light source and/or matching between the vortex of angular momentum and dipole position ([CZCD17], [YHO21],[RHZD21], [HLY⁺19]), but it appears that we have found a new way of explaining the same phenomenon.

We found that, among the various types of interfaces, bearded-stack interface is capable of achieving the most robust propagation as well as the highest directionality/unidirectional coupling efficiency. This could be due to its glide-plane symmetry, as opposed to other types of interface having inversion symmetry. Symmetry always plays a significant role in physics, and especially for topological photonics. It will be interesting to study interfaces having other types of symmetries in the future. However, to promote such studies, it will be important to design efficient software algorithms that can handle larger structures in the future.

Bibliography

- [ABB⁺21] Sonakshi Arora, Thomas Bauer, René Barczyk, Ewold Verhagen, and L. Kuipers. Direct quantification of topological protection in symmetry-protected photonic edge states at telecom wavelengths. *Light: Science and Applications*, 10:9, 2021.
- [BDZ⁺20] Dia'aaldin J. Bisharat, Robert J. Davis, Yun Zhou, Prabhakar R. Bandaru, and Daniel F. Sievenpiper. Photonic topological insulators: A beginner's introduction. *IEEE Antennas and Propagation Magazine*, 62(3), 2020.
- [Ben21] Reiko Inoue Bendtsen. Dielectric photonic crystals sandwiched between parallel metal plates. 9th semester project report, Aalborg University, 2021.
- [BS21] Dia'aaldin J. Bisharat and Daniel F. Sievenpiper. Robust valley polarized states beyond topology. *Research Square*, 2021.
- [CDG⁺11] Daniel R. Cooper, Benjamin D'Anjou, Nageswara Ghattamaneni, Benjamin Harack, Michael Hilke, Alexandre Horth, Norberto Majlis, Mathieu Massicotte, Leron Vandsburger, Eric Whiteway, and Victor Yu. Experimental review of graphene. *ISRN Condens. Matter Phys.*, 2011.
- [CJN⁺16] Xiaojun Cheng, Camille Jouvaud, Xiang Ni, S. Hossein Mousavi, Azriel Z. Genack, and Alexander B. Khanikaev. Robust reconfigurable electromagnetic pathways within a photonic topological insulator. *Nature Materials*, 15, 2016.
- [CZCD17] Xiao-Dong Chen, Fu-Li Zhao, Min Chen, and Jian-Wen Dong. Valley-contrasting physics in all-dielectric photonic crystals: Orbital angular momentum and topological propagation. *Physical Review B*, 96(020202(R)), 2017.
- [DG14] S.E. Dissanayake and K.A.I.L. Garmalath. Simulation of two dimensional photonic band gaps. *International Letters of Chemistry, Physics and Astronomy*, 5, 2014.

- [dPDG⁺20] María Blanco de Paz, Chiara Devescovi, Geza Giedke, Juan José Saenz, Maia G. Vergniory, Barry Bradlyn, Dario Bercioux, and Aitzol García-Etxarri. Tutorial: Computing topological invariants in two-dimensional photonic crystals. *Adv. Quantum Technol.*, 3(2), 2020.
- [FHS05] Takahiro Fukui, Yasuhiro Hatsugai, and Hiroshi Suzuki. Chern numbers in discretized brillouin zone: Efficient method of computing (spin) hall conductances. *J. Phys. Soc. Jpn*, 74(6), 2005.
- [Gap10] Sergey V. Gaponenko. *Introduction to Nanophotonics*. Cambridge University Press, 2. ed. edition, 2010.
- [GSH17] S. Ali Hassani Gangaraj, Mário G. Silveirinha, and George W. Hanson. Berry phase, berry connection, and chern number for a continuum bianisotropic material from a classical electromagnetics perspective. *IEEE Journal on Multiscale and Multiphysics Computational Techniques*, 2, 2017.
- [GYG⁺17] Zhen Gao, Zhaoju Yang, Fei Gao, Haoran Xue, Yahui Yang, Jianwen Dong, and Baile Zhang. Valley surface-wave photonic crystal and its bulk/edge transport. *Physical Review B*, 96(201402(R)), 2017.
- [HDLT11] Mohammad Hafezi, Eugene E. Demler, Mikhail D. Lukin, and Jacob M. Taylor. Robust optical delay lines via topological protection. *Nature Physics*, 7:907–912, 2011.
- [HLY⁺19] Xin-Tao He, En-Tao Liang, Jia-Jun Yuan, Hao-Yang Qiu, Xiao-Dong Chen, Fu-Li Zhao, and Jian-Wen Dong. A silicon-on-insulator slab for topological valley transport. *Nat Commun*, 10(872), 2019.
- [HR08] F. D. M. Haldane and Srinivas Raghu. Possible realization of directional optical waveguides in photonic crystals with broken time-reversal symmetry. *Physical review letters*, 100 1:013904, 2008.
- [IWT⁺19] Milhail I. Shalaev, Wiktor Walasik, Alexander Tsukernik, Yun Xu, and Natalia M. Litchinitser. Robust topologically protected transport in photonic crystals at telecommunication wavelengths. *Nature Nanotech*, 14, 2019.
- [Joh87] S. John. Strong localization of photons in certain disordered dielectric superlattices. *Phys. Rev. Lett.*, 58(23):2486–2489, 1987.
- [KDP80] K. V. Klitzing, G. Dorda, and M. Pepper. New method for high-accuracy determination of the fine-structure constant based on quantized hall resistance. *Phys. Rev. Lett.*, 45(6), 1980.
- [KMT⁺12] Alexander B. Khanikaev, S. Hussein Mousavi, Wang-Kong Tse, Mehdi Kargarian, Allan H. MacDonald, and Gennady Shvets. Photonic topological insulators. *Nature Materials*, 12, 2012.

- [Kre11] Erwin Kreyszig. *Advanced engineering mathematics*. New York, N.Y. : Wiley-Blackwell, 10th edition, 2011.
- [KS17] Alexander B. Khanikaev and Gennady Shvets. Two-dimensional topological photonics. *Nature Photonics*, 11, 2017.
- [LJS14] Ling Lu, John D. Joannopoulos, and Marin Soljačić. Topological photonics. *Nature Photonics*, 8, 2014.
- [LLG⁺15] Andrei V. Lavrinenko, Jesper Lægsgaard, Niels Gregersen, Frank Schmidt, and Thomad M. Søndergaard. *Numerical Methods in Photonics*. Taylor and Francis Group, 1. ed. edition, 2015.
- [LSH⁺21] Jian-Wei Liu, Fu-Long Shi, Xin-Tao He, Guo-Jing Tang, Wen-Jie Chen, Xiao-Dong Chen, and Jian-Wen Dong. Valley photonic crystals. *Advances in Physics*, 6(1,1905546), 2021.
- [Lut15] Hans Luth. *Solid Surfaces, Interfaces and Thin Films*. Springer, 6. ed. edition, 2015.
- [MAB⁺93] R.D. Meade, A.M.Rappe, K.D. Brommer, J.D. Joannopoulos, and O.L. Alerhand. Accurate theoretical anlysis of photonic band-gap materials. *Phys. Rev. B*, 48(8483), 1993.
- [MCG19] Mehul Makwana, Richard Craster, and Sébastien Guenneau. Topological beam-splitting in photonic crystals. *Opt. Express*, 27, 2019.
- [MS16] Tzuhsuan Ma and Gennady Shvets. All-si valley-hall photonic topological insulator. *New J, Phys*, 18(025012), 2016.
- [NHCR17] Jiho Noh, Sheng Huang, Kevin Chen, and Mikael C. Rechtsman. Observation of photonic topological valley-hall edge states. *arXiv: 1706.00059v1*, 2017.
- [OF19] Bakhtiyar Orazbayev and Romain Fleury. Quantitative robustness analysis of topological edge modes in c6 and valley-hall metamaterial waveguides. *Nanophotonics*, 8(8), 2019.
- [OPA⁺19] Tomoki Ozawa, Hannah M. Price, Alberto Amo, Nathan Goldman, Mohammad Hafezi, Ling Lu, Mikael C. Rechtsman, David Schuster, Jonathan Simon, Oded Zilberberg, and Iacopo Carusotto. Topological photonics. *Rev. Mod. Phys.*, 91(1), 2019.
- [RHZD21] Wen-Sheng Ruan, Xin-Tao He, Fu-Li Zhao, and Jian-Wen Dong. Analysis of unidirectional coupling in topological valley photonic crystal waveguides. *Journal of Lightwave Technology*, 39(4), 2021.
- [RZP⁺13] Mikael C. Rechtsman, Julia M. Zeuner, Yonatan Plotnik, Yaakov Lumer, Daniel Podolsky, Felix Dreisow, Stefan Nolte, Mordechai Segev, and Alexander Szameit. Photonic floquet topological insulators. *Nature*, 496(7444), 2013.

- [Sak05] Kazuaki Sakoda. *Optical Properties of Photonic Crystals*. Springer, 2. ed. edition, 2005.
- [SB20] Mordechai Segev and Miguel A. Bandres. Topological photonics: Where do we go from here? *Nanophotonics*, 2020.
- [Søn19] Thomas M. Søndergaard. *Green's Function Integral Equation Methods in Nano-Optics*. CRC Press, 1. ed. edition, 2019.
- [Søn21] Thomas M. Søndergaard. Modeling of two-dimensional photonic crystals using plane-wave-expansion theory and an iterative method taking advantage of the fast fourier transform (lecture notes, aau), 2021.
- [Tor20] Luis E. F. Foa Torres. Floquet topological insulators. <https://www.foatorres.com/floquet-topological-insulators/>, 2020.
- [WCJS09] Zhen Wang, Yidong Chong, J. D. Joannopoulos, and Marin Solkjaic. Observation of unidirectional backscattering-immune topological electromagnetic states. *Nature*, 461, 2009.
- [Wei22] Eric W. Weisstein. Fourier transform. <https://mathworld.wolfram.com/FourierTransform.html>, 2022. Last accessed on 1-May-2022.
- [WGXL20] Hongfei Wang, Samit Kumar Gupta, Biye Xie, and Minghui Lu. Topological photonic crystals: a review. *Optoelectron*, 13(1), 2020.
- [WH15] Long-Hua Wu and Xiao Hu. Scheme for achieving a topological photonic crystal by using dielectric material. *Physical Review Letters*, 114(223901), 2015.
- [Wie12] D. Wiersma. Breaking reciprocity. *Nature Photon*, 6, 2012.
- [WSHO20] Stephan Wong, Matthias Saba, Ortwin Hess, and Sang Soon Oh. Gapless unidirectional photonic transport using all-dielectric kagome lattices. *Physical Review Research*, 2(012011(R)), 2020.
- [XYZ21] Haoran Xue, Yihao Yang, and Baile Zhang. Topological valley photonics: Physics and device applications. *Advanced Photonics Research*, 2(202100013), 2021.
- [Yab87] E. Yablonovitch. Inhibited spontaneous emission in solid-state physics and electronics. *Phys. Rev. Lett.*, 58(20):2059–2062, 1987.
- [YHO21] Jin-Kyu Yang, Yongsop Hwang, and Sang Soon Oh. Evolution of topological edge modes from honeycomb photonic crystals to triangular-lattice photonic crystals. *Physical Review Research*, 3(L022025), 2021.

-
- [YYY⁺20] Yihao Yang, Yuichiro Yamagami, Xiongbing Yu, Prakash Pitchappa, Julian Webber, Baile Zhang, Masayuki Fujita, Tadao Nagatsuma, and Ranjan Singh. Terahertz topological photonics for on-chip communication. *Nature Photonics*, 14:446–451, 2020.
- [ZXC⁺20] Ran Zhao, Guo-Da Xie, Menglin L. N. Chen, Zgugai Lan, Zhixiang H Huang, and Wei E. I. Sha. First-principle calculation of chern number in gyrotropic photonic crystals. *Optics Express*, 28(4/17), 2020.

APPENDIX A

Fast Fourier Transform

This appendix provides a very short review of the Fast Fourier Transform, which is utilized extensively in Programs 2 and 3 to map between real and frequency space.

A.1 Fourier Transform

Consider a continuous, piecewise differentiable L -periodic function $f : \mathbb{R} \rightarrow \mathbb{R}$. *Fourier series* represent such periodic functions as infinite sums of trigonometric functions:

$$f(x) = \frac{a_0}{2} + \sum_{n=1}^{\infty} a_n \cos n \frac{2\pi}{L} x + b_n \sin n \frac{2\pi}{L} x$$

where $a_n, b_n \in \mathbb{R}$ are known as *Fourier coefficients*. Using Euler's formula, we can rewrite the Fourier series above as

$$f(x) = \sum_{n=-\infty}^{\infty} c_n e^{in \frac{2\pi}{L} x}$$

where $c_n \in \mathbb{C}$ are given by the formula

$$c_n = \frac{1}{L} \int_0^L e^{-in \frac{2\pi}{L} x} f(x) dx.$$

However, since by definition $f(x) = f(x + L)$ for all $x \in \mathbb{R}$, periodic functions are only of interest on the finite interval $[0, L]$. To deal with functions that are nonperiodic and are of interest on the whole x -axis, it is necessary to consider the *Fourier transform*, which is a generalization of the complex Fourier series in the limit as $L \rightarrow \infty$. More precisely, we define

$$F(\omega) = \int_{-\infty}^{\infty} e^{-i2\pi x \omega} f(x) d\omega \tag{A.1}$$

as the Fourier transform of $f(x)$, and $\omega \in \mathbb{R}$ as the associated *frequency*, making F a *frequency-domain* function. Given $F(\omega)$, we may recover $f(x)$ by performing an *inverse Fourier transform*:

$$f(x) = \int_{-\infty}^{\infty} e^{i2\pi x\omega} F(\omega) d\omega.$$

Due to their close connection, $f(x)$ and $F(\omega)$ are often referred to as a Fourier transform pair. See e.g. [Kre11] for further details.

A.2 Discrete Fourier Transform and Fast Fourier transform

In many situations, a function $f(x)$ is given only in terms of large amounts of equally-spaced data. In this case, we replace the Fourier transform by the so-called *Discrete Fourier Transform* (DFT).

Consider a finite sequence of complex-valued samples

$$y = \{y_0, y_1, \dots, y_{N-1}\},$$

acquired at constant intervals Δx . Define the discrete sequence of frequencies (wave numbers)

$$k_{\tilde{n}} = \frac{2\pi}{N\Delta x} \tilde{n}, \quad \tilde{n} = 0, 1, \dots, N-1.$$

The Discrete Fourier Transform of y is then given as

$$Y(k_{\tilde{n}}) = \sum_{n=0}^{N-1} y_n e^{-ik_{\tilde{n}}n\Delta x} = \sum_{n=0}^{N-1} y_n e^{-i\frac{2\pi}{N}\tilde{n}n}, \quad \tilde{n} = 0, 1, \dots, N-1, \quad (\text{A.2})$$

where $e^{i\frac{2\pi}{N}}$ is a primitive N 'th root of 1. Analogously with the continuous inverse Fourier transform, the inverse DFT of $Y(k_{\tilde{n}})$ is given as

$$y_n = \frac{1}{N} \sum_{\tilde{n}=0}^{N-1} Y(k_{\tilde{n}}) e^{i\frac{2\pi}{N}\tilde{n}n}, \quad n = 0, 1, \dots, N-1.$$

It is now noted that, for each \tilde{n} , (A.2) specifies a linear equation in y_n , $n = 0, 1, 2, \dots, N-1$:

$$Y(k_{\tilde{n}}) = y_0 + y_1 e^{-i\frac{2\pi}{N}\tilde{n}} + y_2 e^{-i\frac{4\pi}{N}\tilde{n}} + \dots + y_{N-1} e^{-i\frac{2(N-1)\pi}{N}\tilde{n}}.$$

By letting \tilde{n} go from 0 to $N-1$ and stacking the resulting equations on top of one of another, it is possible to write this expression in matrix form:

$$\begin{bmatrix} Y(k_0) \\ Y(k_1) \\ Y(k_1) \\ \vdots \\ Y(k_{N-1}) \end{bmatrix} = \begin{bmatrix} 1 & 1 & 1 & \dots & 1 \\ 1 & e^{-i\frac{2\pi}{N}} & e^{-i\frac{4\pi}{N}} & \dots & e^{-i\frac{2(N-1)\pi}{N}} \\ 1 & e^{-i\frac{4\pi}{N}} & e^{-i\frac{8\pi}{N}} & \dots & e^{-i\frac{4(N-1)\pi}{N}} \\ \vdots & \vdots & \vdots & \ddots & \vdots \\ 1 & e^{-i\frac{2(N-1)\pi}{N}} & e^{-i\frac{4(N-1)\pi}{N}} & \dots & e^{-i\frac{2(N-1)^2\pi}{N}} \end{bmatrix} \begin{bmatrix} y_0 \\ y_1 \\ y_2 \\ \vdots \\ y_{N-1} \end{bmatrix}.$$

This shows that the DFT is a linear transformation from the N -dimensional discrete space domain to the N -dimensional discrete frequency domain. All linear transformations from a vector space to itself take the form $\mathbf{y} = \mathbf{A}\mathbf{x}$, and if they are invertible, the inverse transformations take the form $\mathbf{x} = \mathbf{A}^{-1}\mathbf{y}$. The inverse DFT may similarly be written on matrix form, and the coefficient matrix of the inverse DFT may be computed as $1/N$ times the complex conjugate of the original (symmetric) coefficient matrix.

However, computing a DFT directly from the definitions above is often too slow to be practical. Moreover, since a small number of sampling points has a tendency of causing a problem known as *aliasing*, where frequencies corresponding to \tilde{n} higher than $N/2$ “appear” as lower frequencies in the transformed data, we often need to require large N for reliable analysis.

The *Fast Fourier transform* (FFT) is an algorithm that computes the discrete DFT of a sequence (or its inverse DFT), for which highly effective software implementations are readily available. The FFT rapidly computes the transformation by factorizing the DFT matrix into a product of sparse (mostly zero) factors. As a result, it manages to reduce the complexity of computing the DFT from N^2 to $N \log_2 N$ operations. For instance, when $N = 1000$, those operations are reduced by a factor of $N/\log_2 N \approx 100$. [Kre11] [Wei22]

A.3 Convolution Theorem

A convolution is an integral that expresses the amount of overlap of one function g as it is shifted over another function f . It therefore “blends” one function with another. Convolution of two functions f and g over a finite range $[0, t]$ is given by

$$f(t) * g(t) = \int_0^t f(\tau)g(t - \tau)d\tau$$

where the symbol $f(t) * g(t)$ denotes convolution of f and g . Convolution is more commonly defined over an infinite range [Wei22]:

$$f(t) * g(t) = \int_{-\infty}^{\infty} f(\tau)g(t - \tau)d\tau = \int_{-\infty}^{\infty} g(\tau)f(t - \tau)d\tau.$$

For example, a convolution integral can be an output response $y(t)$ to two signals $h(t)$ and $u(t)$, where $h(t)$ is the impulse response of a linear time-invariant dynamical system and $u(t)$ is an input signal:

$$y(t) = \int_{-\infty}^{\infty} h(t - \tau)u(\tau)d\tau.$$

Notice the obvious similarity with $E(\mathbf{r}) = i\omega\mu_0 \int g(\mathbf{r}-\mathbf{r}')J(\mathbf{r}')d^2r'$ in GFAIEM, when the variables t and τ (time domain) are replaced with \mathbf{r}/\mathbf{r}' (spatial domain).

The discrete-time counterparts can be defined using two sequences $h = \{h_n\}$ and $u = \{u_n\}$ as

$$y_n = h * u = \sum_{\kappa=-\infty}^{\infty} h_{\kappa}u_{n-\kappa} = \sum_{\kappa=-\infty}^{\infty} h_{n-\kappa}u_{\kappa}.$$

Importantly, convolution in the time/spatial domain corresponds to standard (pointwise) multiplication in the Fourier domain due to the *convolution theorem*:

$$h * u \leftrightarrow H(\omega_{\tilde{n}}) \cdot U(\omega_{\tilde{n}}). \quad (\text{A.3})$$

See e.g., [Wei22] for the proof.

Like the DFT, performing a convolution integral on two discrete sequences also encompasses a computational load of the order N^2 . However, by using the FFT algorithm, it is possible to perform calculation of convolution integrals much more efficiently. That is, we can benefit from the aforementioned $N \log_2 N$ computation scaling by Fourier transforming both signals, perform element-by-element multiplication of the transformed signals, and then inverse transform the result to get back to the time/spatial domain.

